THERMAL-ELECTROCHEMICAL MODELING AND STATE OF CHARGE ESTIMATION FOR LITHIUM ION BATTERIES IN REAL-TIME APPLICATIONS

THERMAL-ELECTROCHEMICAL MODELING AND STATE OF CHARGE ESTIMATION FOR LITHIUM ION BATTERIES IN REAL-TIME APPLICATIONS

BY

MOHAMMED FARAG, M.A.Sc., B.Sc.

A THESIS
SUBMITTED TO THE DEPARTMENT OF MECHANICAL ENGINEERING
AND THE SCHOOL OF GRADUATE STUDIES
OF MCMASTER UNIVERSITY
IN PARTIAL FULFILMENT OF THE REQUIREMENTS
FOR THE DEGREE OF
DOCTOR OF PHILOSOPHY

© Copyright by Mohammed Farag, February 2017
All Rights Reserved

DOCTOR OF PHILOSOPHY (2017) McMaster University
(Mechanical Engineering) Hamilton, Ontario, Canada

TITLE:	Thermal-Electrochemical Modeling and State of Charge Estimation for Lithium Ion Batteries in Real-Time Applications
AUTHOR:	Mohammed Farag M.A.Sc., (Mechanical Engineering) McMaster University, Hamilton, Ontario, Canada
SUPERVISOR:	Dr. Saeid R. Habibi, Professor Department of Mechanical Engineering
NUMBER OF PAGES:	xxii, 226

I dedicate this work to my wonderful parents.

”It is not the critic who counts; not the man who points out how the strong man stumbles, or where the doer of deeds could have done them better. The credit belongs to the man who is actually in the arena, whose face is marred by dust and sweat and blood; who strives valiantly; who errs, who comes short again and again, because there is no effort without error and shortcoming; but who does actually strive to do the deeds; who knows great enthusiasms, the great devotions; who spends himself in a worthy cause; who at the best knows in the end the triumph of high achievement, and who at the worst, if he fails, at least fails while daring greatly, so that his place shall never be with those cold and timid souls who neither know victory nor defeat.”

Theodore Roosevelt

Permission to use

In presenting this thesis in partial fulfillment of the requirements for a Postgraduate degree from McMaster University, I agree that the Libraries of this University may make it freely available for inspection. I further agree that the permission for copying this thesis in any manner, in whole or in part for scholarly purposes, may be granted by the professors who supervised my thesis work or, in their absence, by the Head of the Department or the Faculty Dean in which my thesis work was conducted. It is understood that any copying or publication or use of this thesis or parts thereof for financial gain shall not be allowed without my written permission. It is also understood that due recognition shall be given to me and McMaster University in any scholarly use which may be made of any material in my thesis. Requests for permission to copy or to make other use of material in this thesis, in whole or part, should be addressed to:

Head of the Department of Mechanical Engineering
McMaster University
Faculty of Engineering
1280 Main Street West
Hamilton, Ontario L8S 4L6, Canada.

Abstract

In the past decade, automobile manufacturers have gone through the initial adoption phase of electric mobility. The increasing momentum behind electric vehicles (EV) suggests that electrified storage systems will play an important role in electric mobility going forward. Lithium ion batteries have become one of the most common solutions for energy storage due to their light weight, high specific energy, low self-discharge rate, and non-memory effect. To fully benefit from a lithium-ion energy storage system and avoid its physical limitations, an accurate battery management system (BMS) is required. One of the key issues for successful BMS implementation is the battery model. A robust, accurate, and high fidelity battery model is required to mimic the battery dynamic behavior in a harsh environment. This dissertation introduces a robust and accurate model-based approach for lithium-ion battery management system.

Many strategies for modeling the electrochemical processes in the battery have been proposed in the literature. The proposed models are often highly complex, requiring long computational time, large memory allocations, and real-time control. Thus, model-order reduction and minimization of the CPU run-time while maintaining the model accuracy are critical requirements for real-time implementation of lithium-ion electrochemical battery models. In this dissertation, different modeling techniques are developed. The proposed models reduce the model complexity while maintaining the accuracy.

The thermal management of the lithium ion batteries is another important consideration for a successful BMS. Operating the battery pack outside the recommended operating conditions could result in unsafe operating conditions with undesirable consequences. In order to keep the battery within its safe operating range, the temperature of the cell core must be monitored and controlled. The dissertation implements a real-time electrochemical, thermal model for large prismatic cells used in electric vehicles' energy storage systems. The presented model accurately predicts the battery's core temperature and terminal voltage.

Acknowledgements

Firstly, I would like to express my sincere gratitude to my advisor Prof. Saeid Habibi for the continuous supervision of my Ph.D. study, for his patience, motivation, and immense knowledge. His guidance helped me in all the time of research.

Besides my advisor, I would like to thank my thesis committee: Prof. A. Emadi, Prof. G. Goward, and Prof. F. Yan, for their insightful comments and encouragement.

Financial support provided by the BMW AG, the Natural Sciences and Engineering Research Council of Canada (NSERC), the School of Graduate Studies, the Department of Mechanical Engineering, and the Ontario Government's Graduate Scholarship Program is acknowledged.

My sincere thanks also go to my BMW colleagues in Munich, Germany, who provided me an opportunity to join their team, and provided access to the laboratory data and research facilities.

I would like to thank all my friends, A. El-Mazariky and L. Schumann for their continuous support, encouragement and for all the fun we had in the past few years. Also, without whom this thesis would have been completed a year earlier.

Last but not the least, I would like to thank my family: my parents, my brother, and my sister for their endless love, encouragement, and absolute confidence in me throughout my life.

Publications and Patents

In compliance with the regulations of McMaster University, this dissertation is assembled as a sandwich thesis composed of four journal articles. These articles represent the independent work of the author of this dissertation. The research also resulted in two patents. The publications and patents are as follows.

[1] International Patent - filled in June 28, 2016 and received an application no. PCT/EP2016/065003.
Authors: **Mohammed Farag** (McMaster Univeristy), Benno Schweiger (BMW AG), and Saeid Habibi (McMaster Univeristy).
Title: Method and device for estimating a voltage of a battery

[2] International Patent - filled in June 28, 2016 and received an application no. PCT/EP2016/064998.
Authors: **Mohammed Farag** (McMaster Univeristy), Edwin Knobbe (BMW AG), Benno Schweiger (BMW AG), Matthias Fleckenstein (BMW AG), and Saeid Habibi (McMaster Univeristy).
Title: Method and device for estimating the state of charge of a battery

[3] Journal article - submitted and accepted by the Journal of Power Sources

Mohammed Farag, Matthias Fleckenstein, and Saeid Habibi.

Title: Continuous piecewise-linear, reduced-order electrochemical model for lithium-ion batteries in real-time applications. http://dx.doi.org/10.1016/j.jpowsour.2016.12.044

[4] Journal article - Submitted in December 2016 and under revision by the Journal of Power Sources

Mohammed Farag, Haitham Sweity, Matthias Fleckenstein, and Saeid Habibi.

Title: Combined reduced-order electrochemical, heat generation, and thermal model for large prismatic lithium-ion batteries in real-time applications.

[5] Journal article - submitted in March 2017 to the IEEE Journal of Emerging and Selected Topics in Power Electronics

Mohammed Farag and Saeid Habibi.

Title: A critical comparative review of battery modeling categories and state of charge estimation strategies for real-time applications.

[6] Journal article - Accepted by the International Journal of Chemical, Molecular, Nuclear, Materials and Metallurgical Engineering.

Mohammed Farag, Mina Attari, Andrew Gadsden, and Saeid Habibi.

Title: Li-ion battery state of charge estimation using one state hysteresis model with nonlinear estimation strategies. http://waset.org/publications/10006626

Table of Contents

List of Tables

List of Figures

Chapter 1

Introduction

1.1 Thesis Motivation

This research was motivated by global concerns related to the greenhouse gas emissions (GHG) and the need for improving the fuel efficiency of transportation systems. The United States Environmental Protection Agency (EPA) report in 2014 showed that the GHG emissions from the transportation sector contribute 26% to the total GHG emissions [2]. In order to reduce the emissions of the transportation sector, the National Highway Traffic Safety Administration (NHTSA) has set new standards to improve the Corporate Average Fuel Economy (CAFE) levels on a yearly basis starting from 2017 until 2025. By 2025, the CAFE standard aims to increase the corporate fleet fuel efficiency to 54.5 miles per gallon (mpg) (5.6 liter/100 km) and reduce the CO_2 emissions to 163 grams/mile. The 2025 CAFE goals improve the fuel efficiency by 20% compared to the 2017 target of 40.3 mpg (7 liter/100 km) [3].

The automakers are expected to produce more hybrid electric vehicles (HEVs), plug-in hybrid electric vehicles (PHEVs), and battery electric vehicles (BEVs) in order to reduce the overall fleet emissions and meet the new restrictive emissions standards. Lithium ion batteries have become one of the most attractive alternatives for electric vehicle energy storage systems due to their light weight, high specific energy, low self-discharge rate, and non-memory effect [1].

The electric vehicle energy storage systems consist of a battery pack and a battery management system (BMS). The battery pack consists of multiple modules and each module consists of multiple connected cells. The BMS is essential for maximizing the benefits of lithium-ion batteries and cells and avoid their physical limitations. The BMS is responsible for performance management which includes but is not limited to the state of charge (SOC), state of health (SOH), and state of function (SOF) estimation algorithms, as well as cell balancing, power management, and thermal management. One of the key issues for successful BMS implementation is the battery model. A robust, accurate, and high fidelity battery model is required to simulate the dynamic cell behavior in a demanding environment.

1.2 Thesis contributions and novelty

This dissertation presents contributions in the area of lithium-ion battery electrochemical modeling, thermal modeling, heat generation modeling, state of charge estimation, core temperature estimation, and thermal management strategies, with the focus on their real-time application in the battery manage systems of hybrid and electric vehicles. The contributions of this dissertation are divided into primary contributions and secondary contribution as follows:

Primary contribution:

- Development of a continuous piecewise-linear, reduced-order electrochemical model for lithium-ion batteries in real-time applications.
- Development of a combined electrochemical, heat generation, and thermal model for large prismatic lithium-ion batteries in real-time applications.
- A critical review of the most commonly used modeling categories and nonlinear state estimation strategies for lithium-ion energy storage systems real-time applications.

Secondary contribution:

- Reducing the computational cost (CPU run-time) of the single particle electrochemical model while maintaining accuracy using a piecewise linearization technique.
- Development of an optimal knot-placement algorithm for continuous piecewise-linear approximation of electrochemical models.
- Determination of the model parameters dependencies on the electrode's state of charge.
- Development of a four nodes thermal model for large format prismatic cells.
- Development of a parameterization scheme that aids in identifying the model parameters under isothermal and non-isothermal operating conditions.
- Identification of the model parameters dependencies on temperature.

- Introducing a heat generation model that accounts for different loss mechanisms.
- Comparatively assessing three different estimation strategies based on their rate of convergence, robustness against modeling and measurement uncertainties, computational complexity, tuning complexity, and SOC estimation accuracy under normal operating conditions.

1.3 Thesis Outline

The thesis is organized as follows:

Chapter 2 provides a literature review of the battery management system, battery models, thermal models, heat generation models, state of charge estimation techniques, and battery aging mechanisms.

Chapter 3 proposes a new reduced-order, electrode-average, electrochemical model using piecewise linearization technique. The Genetic Algorithm (GA) optimization strategy is used to determine the optimal knot-locations. The proposed model reduces the univariate nonlinear function of the electrode's open circuit potential dependence on the state of charge with respect to continuous piecewise regions. The proposed model is complemented by parameterization experiments that were specifically chosen to isolate the slow changing parameters from the fast changing parameters, and that provided a trade-off between extensive experimental characterization and parameter identifications using optimization techniques.

The parametrization experiments are described and the data was gathered using a prismatic lithium-ion battery cell suitable for high-power applications like PHEVs,

HEVs, and EVs. The experimental tests were done on 12 channels, Scienlab battery test bench. During testing, the cells were placed in a climate chamber with a continuously controlled ambient temperature maintained at 25°C.

Chapter 4 proposes an accurate combined electrochemical, heat generation, and thermal model for large prismatic cells. The proposed model consists of three sub-models, an electrochemical model, a heat generation model, and a thermal model. These are integrated together in an iterative fashion through physicochemical temperature dependent parameters. A parameterization scheme is then used to identify the sub-models' parameters separately by exciting the battery under isothermal and non-isothermal operating conditions. The proposed combined model structure shows accurate terminal voltage and core temperature prediction at various operating conditions while maintaining a simple mathematical structure, making it ideal for real-time BMS applications.

Experimental data was gathered using a prismatic lithium-ion battery cell suitable for high-power applications like PHEVs, HEVs, and EVs. During testing, the cells were placed in a climate chamber with a constantly controlled ambient temperature. The tests were repeated at six different temperature points.

Chapter 5 presents a critical review of the most commonly used battery model categories and non-linear state estimation strategies in lithium-ion battery energy storage applications. The modeling categories include Behavioral models, Equivalent circuit models, and Electrochemical models. A representative model from each category is considered. The two-states enhanced self-correcting model, the two-RC model, and the reduced-order, electrode average electrochemical model are considered as representatives of behavioral models, equivalent circuit models, and electrochemical models, respectively. The performance of the three models performance are analyzed with respect to their terminal voltage prediction accuracy, parameterization efforts, and computational complexity. Three non-linear estimation strategies are also considered and compared using the reduced order electrochemical model. The estimation strategies include, the extended Kalman filter (EKF), the smooth variable structure filter (SVSF), and the unscented Kalman filter (UKF). The estimation strategies are comparatively assessed based on their rate of convergence, robustness against modeling and measurement uncertainties, computational complexity, tuning complexity, and SOC estimation accuracy under normal operating conditions.

Chapter 6 presents the implementation of three non-linear estimation strategies for Li-Ion battery SOC estimation. The one state hysteresis (OSH) model is used as a standard benchmark for the three strategies. The extended Kalman filter (EKF), the smooth variable structure filter (SVSF), and the time varying smoothing boundary layer SVSF (VBL-SVSF) are applied on the model, and the results are compared.

Chapter 7 provides the conclusions and recommendations for future work.

Chapter 2

Literature Review

2.1 Introduction

In the past decade, automotive manufacturers have been increasingly aligning with electric mobility. The increasing momentum behind electric vehicles (EV) suggests that electric energy storage systems will play a major role in transportation going forward. Lithium ion batteries have become one of the most attractive solutions for electric vehicles' energy storage systems due to their light weight, high specific energy, and low self-discharge rate [1].

In order to efficiently integrate lithium-ion batteries in electric vehicles (EVs), different cell chemistries have been introduced. Ragone plot presented in Figure 2.1 shows the current and projected status of batteries in HEV, PHEV, and BEV with respect to the United States Advanced Battery Consortium (USABC) requirements [4].

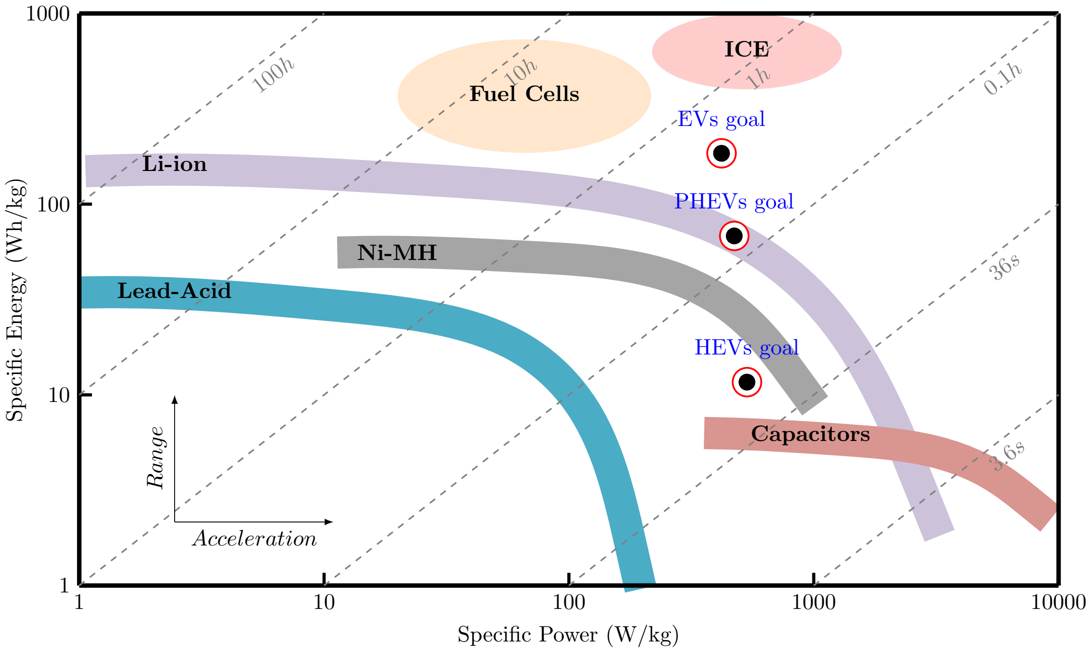

Figure 2.1: Ragone plot of different energy storage chemistries.

The Internal Combustion Engine (ICE) has the highest specific power and specific energy due to the nature of fossil fuels. Ultra-capacitors possess the highest specific power, which enables them to supply a large instantaneous peak power. Alternatively, fuel cells have a large specific energy density but require a hydrogen infrastructure. Lithium-ion based batteries provide an attractive choice for the HEVs and PHEVs due to their large combined energy and power densities. As a result, considerable investment and research are being made for their development in order to improve their performance, reliability, safety and longevity.

2.2 Background

2.2.1 Operating principles of Li-ion batteries

A battery converts chemical energy into electrical energy and vice versa. The basic setup of a battery cell consists of four main parts: the positive electrode, the separator, the electrolyte, and the negative electrode, as shown in Figure 2.2.

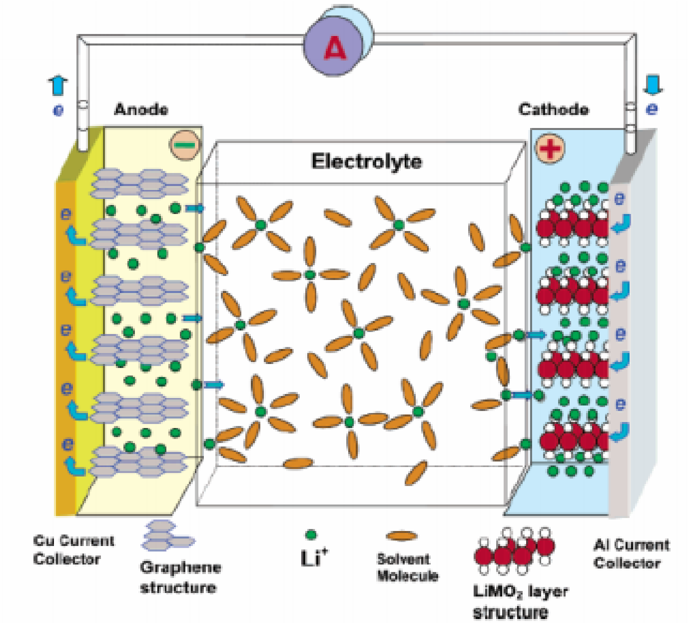

Figure 2.2: Schematic representation of a Li-ion battery during discharging [14].

The positive and negative electrodes are referred to as the cathode and the anode. The battery is connected to an external load using current collector plates. In the case of Li-ion cells, a copper collector is used in the negative electrode while an aluminum collector is used for the positive electrode.

The anode is the electrode capable of supplying electrons to the load. The anode is usually made up of a mixture of carbon (e.g. Li_xC_6), the cathode is typically made of metal oxides (ex. $LiCoO_2$ or $LiMn_2O_4$), while the electrolyte can be a salt-containing solvent mixture, polymer, or solid materials (e.g. $LiPF_6$), polymer or solid materials.

In the case of solid or polymer materials, the electrolyte will also act as a separator. The separator is a porous membrane allowing the transfer of lithium ions between the electrodes, but which also serves as a barrier to electrons. It prevents the occurrence of a short-circuit and thermal run away, while at the same time offering negligible resistance to the flow of ions between the electrodes.

Under the presence of a load current, reduction-oxidation reaction occurs. Oxidation reaction takes place at the anode where the trapped lithium particles start to deintercalate or diffuse toward the electrolyte-solid interface splitting lithium into ions and electrons. Lithium ions transfer through the solution due to the potential difference while the electrons move through the current collector because the electrolyte solution serves as a barrier to electrons. Reduction reaction takes place at the cathode where the traveling lithium ions from the anode start to intercalate and react with the electrons coming from the positive collector. The electrochemical reactions are as follows:

$$Li_xC_6 \xrightleftharpoons[charge]{discharge} Li_0C_6 + xLi^+ + xe^- \tag{2.1}$$

$$Li_{(y-x)}Mn_2O_4 + xLi^+ + xe^- \xrightleftharpoons[charge]{discharge} Li_yMn_2O_4 \tag{2.2}$$

The process of lithium ion insertion into the electrode happens without a change in the electrode crystal structure ”intercalation” mechanism. The whole phenomenon of intercalation and deintercalation is reversible as lithium ions pass back and forth between the electrodes during charging and discharging. In theory, this phenomenon could go on infinitely. Unfortunately, due to cell material degradation and other irreversible chemical reactions, the cell capacity and power degrade with the number of cycles and usage.

2.2.2 Battery terminology

Cell, Modules and Packs

Every HEV, PHEV, and BEV contains a high voltage battery pack that consists of multiple modules, each module consists of multiple cells. A cell is the smallest unit connected in parallel or in series to form one module. A module is then connected in a parallel or series configuration to form one pack.

Nominal capacity

Nominal capacity C_n is determined by the manufacturer and referred to as the coulometric capacity. The C_n is equal to the total Amp-hours drawn to fully discharge a cell from 100% state of charge to the cut-off voltage. The capacity is then calculated as the multiplication of the discharge current (in Amps) by the discharge time (in hours) [5].

C-Rate

The C-Rate describes the rate at which the battery is charged or discharged relative to its maximum capacity C_n. It is often used to normalize the discharge current of batteries with different capacities. It can be calculated as follows:

$$C - Rate = \frac{I[A]}{C_n[Ah]}, \qquad [1/\mathrm{h}] \quad (2.3)$$

State of charge

The state of charge (SOC) is the ratio between the present capacity to the nominal capacity C_n in percentage.

State of health

The state of health (SOH) is a ratio that indicates a condition reached in the battery's life cycle between the beginning of life (BoL) and end of life (EoL).

2.3 Battery management system

The battery management system is a critical component of the energy storage system found in Electric Vehicle (EVs) and Hybrid Electric Vehicles (HEVs). To fully benefit from a lithium-ion energy storage system and avoid its physical degradation, an accurate Battery Management System (BMS) is required. The main objective of a BMS is to monitor, control, and balance all the cells in the battery pack. The five main functionalities for the BMS can be summarized as follows [6]:

- Cell protection.
- Performance management.
- Communication.
- Diagnostics.
- History.

The BMS uses mathematical models and state estimation algorithms to perform the above mentioned functions. One of the main requirements for a successful BMS implementation is the development of a high fidelity battery model that is complemented and coupled with a thermal model and an aging model. The models need to be dynamically significant while being computationally efficient, robust, and accurate.

Of particular interest is the prediction of the terminal voltage which is affected by the cell's core temperature. As such, an accurate thermal model is needed to predict the core temperature and estimate its dynamics. The inclusion of a thermal model within the overall battery model is necessary as it enables the BMS to operate the battery safely and preserve its performance effectively. In section 2.4, battery models are discussed in details, and in section 2.5 the literature pertaining to thermal models is reviewed..

2.4 Battery models

In the literature, numerous battery models have been reported. The choice between these models is a trade-off between model complexity, accuracy, and parameterization effort. The models can be classified into three categories of increasing complexity: behavioral (or black-box) [7, 8, 9, 10], equivalent circuit [11, 12, 13, 14], and finally detailed electrochemical (physics-based) models [1, 15, 16] Currently, the equivalent circuit models are commonly used in the BMS because of their low computational complexity and acceptable accuracy. However, they are not capable of describing the battery's internal physical behavior.

2.4.1 Ideal battery models

As the name suggests, the battery is represented as an ideal voltage source. These models are used in studies where the energy storage device (battery) is not of interest.

2.4.2 Behavioral or Black-box battery models

Behavioral or Black-box Models simulate the terminal voltage behavior of the batteries without the need for the specification or approximation of the underlying physical or electrochemical behavior. These models consist of phenomenological functions that require measured data to be used. Alternatively, neural networks, empirical functions or look-up tables may be utilized. Peukert's law [17] is one of the first well-known examples of a behavioral model for batteries, where an empirical function is used to describe the dependence of the battery's remaining capacity on the discharge rate as follows.

$$I^{PC} t = constant \tag{2.4}$$

Where, I is the discharge current, t is the maximum discharge time and PC is the Peukert's Coefficient which ranges from 1 to 2 [18]. The battery capacity can be calculated as follows [18]:

$$C_{n1} = C_n \left(\frac{I_n}{I_{n1}} \right)^{PC-1} \tag{2.5}$$

Where C_{n1} is the battery remaining capacity at the discharge current of I_{n1} [18].

Another form of behavioral model was introduced by Shepherd [19], to predict the terminal voltage during charging/discharging conditions as follows [20]:

$$E(t) = E_0 + R_\alpha i(t) + \frac{K_1}{q_s(t)} \tag{2.6}$$

Where, E_0 is the initial cell voltage, R_α is the cell internal resistance, $q_s(t)$ is the instantaneous stored charge, and K_1 is a constant. A further modification was made to equation (2.3) by the Unnewehr model [20]:

$$E(t) = E_0 + R_\alpha i(t) + K_2 q_s(t) \tag{2.7}$$

Nernst introduced another two constants K_3 and K_4 which are used for curve fitting as follows:

$$E(t) = E_o + R_\alpha i(t) + K_3 \frac{q_s(t)}{Q} - K_4 ln\left(\frac{Q - q_s(t)}{Q}\right) \tag{2.8}$$

Where, Q is the total charge capacity of the cell and the constants K_1, K_2, K_3, and K_4 can be obtained by fitting experimental data [21].

Plett combined a series of behavioral models to simulate the battery operations [7, 8, 9]. Four models were discussed in his publication namely simple, zero-hysteresis, one-state hysteresis, and enhanced self-correcting (ESC). All of these were based on Peukert's and Shepherd's models. These models can account for cell hysteresis, polarization time constants, and ohmic loss effects [10]. Use of artificial neural networks and fuzzy logic in modeling is discussed in [22]. Behavioral models can achieve terminal voltage prediction accuracy of up to 5% [16, 23].

The combined model

Shepherd/Unnewehr/Nernst models are combined to make a 'combined model' that performs better than any of the individual models alone [8]. The combined model is defined as follows:

$$z_{k+1} = z_k - \frac{\eta_i \Delta t}{C} i_k \tag{2.9}$$

$$y_k = K_0 - Ri_k - \frac{K_1}{z_k} - K_2 z_k + K_3 ln(z_k) + K_4 ln(1 - z_k) \tag{2.10}$$

This model has the advantage of being linear in the parameters, which makes it easier to implement and estimate. Accordingly, the unknown quantities in the model may be estimated using a system identification procedure. For example, given a set of N cell input-output parameters (y_k,i_k,z_k), the values may be solved for in a closed form using least squares estimation [8].

The simple model

The simple model is obtained from the combined model. The output equation of the simple model is divided into two additive parts: one depending only on the SOC (z_k), and the other depending only on the current (i_k). Doing so yields equations (2.11) and (2.12):

$$f(z_k) = OCV(z_k) = K_0 - \frac{K_1}{z_k} - K_2 z_k + K_3 ln(z_k) + K_4 ln(1 - z_k) \tag{2.11}$$

$$f(i_k) = Ri_k \tag{2.12}$$

Equation (2.11) and (2.12) are combined in one equation for an easier and more accurate implementation of the combined model as follows:

$$z_{k+1} = z_k - \frac{\eta_i \Delta t}{C} i_k \tag{2.13}$$

$$y_k = OCV(z_k) - Ri_k \tag{2.14}$$

Where $OCV(z_k)$ refers to the open circuit voltage.

The zero-state hysteresis model

An important concept that is overlooked by the previous two models includes hysteresis. For improved SOC estimation, the hysteresis effects of the terminal voltage should be considered. As described in [10], a basic model of hysteresis simply adds a term to the output equation (2.14) as follows:

$$y_k = OCV(z_k) - s_k M(z_k) - Ri_k \tag{2.15}$$

Where s_k represents the sign of the current (with memory during a rest period). For some sufficiently small and positive value ε, s_k can be calculated as follows:

$$s_k = \begin{cases} +1 & : i_k > \varepsilon \\ -1 & : i_k < -\varepsilon \\ s_k - 1 & : |i_k| \leqslant \varepsilon \end{cases} \tag{2.16}$$

Also, note that $M(z_k)$ is half the difference between the charge and discharge values (i.e., some value of hysteresis) [10]. Typically, the value for M can be assumed constant. As per [8], the zero-state hysteresis model is an improvement over the simple model, but only crudely approximates the underlying phenomenon. Whereas the level of hysteresis slowly changes as the cell is charged or discharged, the model estimates hysteresis as immediately flipping between its maximum positive and negative values when the sign of current changes.

The one-state hysteresis model

The slow transition may be modeled by adding a 'hysteresis state' to the model. The hysteresis state is not a differential equation as a function of time but in SOC (i.e., ampere-hours). Suppose that $h(z,t)$ is the hysteresis voltage, then one has [8]:

$$\frac{dh(z,t)}{dz} = \gamma sgn(\dot{z})[M(z,\dot{z}) - h(z,t)] \tag{2.17}$$

Where $M(z,\dot{z})$ is a function that gives the maximum polarization due to hysteresis as a function of SOC and the rate-of-change of SOC. The term $M(z,\dot{z}) - h(z,t)$ states that the rate-of-change of hysteresis voltage is proportional to the distance away from the main hysteresis loop; leading to a type of voltage decay in the major loop. The term γ is considered positive and constant and affects the rate of voltage decay. The sign function forces the equation to be stable for both charge and discharge. The overall state-space equations for the one-state hysteresis model are as follows [8]:

$$\begin{bmatrix} h_{k+1} \\ z_{k+1} \end{bmatrix} = \begin{bmatrix} F(i_k) & 0 \\ 0 & 1 \end{bmatrix} \begin{bmatrix} h_k \\ z_k \end{bmatrix} + \begin{bmatrix} 0 & 1 - F\left(i_k\right) \\ -\frac{\eta_i \Delta t}{C} & 0 \end{bmatrix} \begin{bmatrix} i_k \\ M\left(z,\dot{z}\right) \end{bmatrix} \tag{2.18}$$

$$y_k = OCV(z_k) + h_k - Ri_k \tag{2.19}$$

where $F(i_k) = exp(-|\eta_i i(t)\gamma / C_n|)$

The enhanced self-correcting model

The enhanced self-correction (ESC) battery model represents one of the most accurate models that are currently being used for battery SOC estimation. This model can accurately capture battery dynamics and thus can be implemented in a vehicle BMS as it accommodates for hysteresis, polarization time constants, and ohmic losses. The ESC model in the state space form is as follows [8]:

$$\begin{bmatrix} f_{k+1} \\ h_{k+1} \\ z_{k+1} \end{bmatrix} = \begin{bmatrix} diag(\alpha) & 0 & 0 \\ 0 & F(i_k) & 0 \\ 0 & 0 & 1 \end{bmatrix} \begin{bmatrix} f_k \\ h_k \\ z_k \end{bmatrix} + \begin{bmatrix} 1 & 0 \\ 0 & 1 - F(i_k) \\ -\frac{\eta_i \Delta t}{C} & 0 \end{bmatrix} \begin{bmatrix} i_k \\ M\left(z, \dot{z}\right) \end{bmatrix} \tag{2.20}$$

$$y_k = OCV(z_k) + h_k - Ri_k + Gf_k \tag{2.21}$$

Where z_k is the state of charge, f_k is the states of the low pass filter on i_k which is used to characterize the polarization time constants, h_k is the state representing charging or discharging hysteresis effect, OCV is the open circuit voltage, C_n is the nominal battery capacity, R is the internal battery resistance, G is the output matrix of the low pass filter, and α are the poles of the low pass filter.

This model contains two inputs as follows: i_k is the battery input current, and $M(z, \dot{z})$ which represents the maximum polarization due to hysteresis. The model has one output y_k, which is the terminal voltage. It is important to note that this model may be broken into two models; based on either two states or four states [8, 10].

2.4.3 Equivalent circuit battery models

Lumped-element equivalent circuit components such as resistors and capacitors can be used to represent the behavior of a battery cell [14]. They are widely applied because of their simplicity, a low number of parameters to tune, and easy implementation. They commonly consist of first-order, second-order, or third-order RC models in addition to the hysteresis effect. The model parameters such as resistances and capacitances are calculated by system identification using test data. Present Battery Management Systems (BMS) rely on Equivalent circuit models due to their simplicity and robustness, which allow these models to be implemented in real-time applications. However, they have limitations in providing insight into the electrochemical reactions that occur internally inside the cell. This limitation makes them unable to predict electrochemical phenomena like cell degradation, capacity fading, and power fading. In literature, these models also can be coupled or integrated with thermal models to predict the overall cell behavior as discussed in [24].

The first order RC models

The first order RC model represents the simplest equivalent circuit model [14]. It consists of one RC pair connected in series with resistance. The state and measurement equations of the system are represented by (2.22) and (2.23) respectively. The schematic diagram is shown in Figure 2.3. It can be easily implemented in real-time applications due to its simplicity.

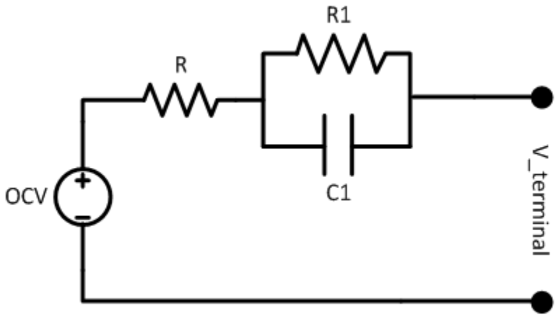

Figure 2.3: Schematic diagram of the first order RC Battery Model.

$$\begin{bmatrix} V^1_{k+1} \\ z_{k+1} \end{bmatrix} = \begin{bmatrix} 1 - \frac{\Delta t}{R_1 C_1} & 0 \\ 0 & 1 \end{bmatrix} \begin{bmatrix} V^1_k \\ z_k \end{bmatrix} + \begin{bmatrix} \frac{\Delta t}{C_1} \\ -\frac{\eta_i \Delta t}{C} \end{bmatrix} \begin{bmatrix} i_k \end{bmatrix} \tag{2.22}$$

$$y_k = OCV(z_k) - Ri_k - V_k^1 \tag{2.23}$$

Where, z_k is the state of Charge of the battery cell, V_k^1 is the voltage drop across the first RC pair, C is the battery nominal capacity, R is the battery ohmic resistance, y_k is the battery terminal voltage, and η_i is the charging and discharging efficiency.

The parameters to be optimized are given in Equation (2.24).

$$\theta = [R^+, R^-, R_1, C_1] \tag{2.24}$$

The first order RC models with one-state hysteresis

The hysteresis state is incorporated by adding the OCV charging and discharging hysteresis effect to the first order RC model. The state and measurement equations of the system are represented by (2.25) and (2.26) respectively. While the parametric vector to be optimized is shown in Equation (2.27).

$$\begin{bmatrix} V_{k+1}^1 \\ h_{k+1} \\ z_{k+1} \end{bmatrix} = \begin{bmatrix} 1 - \frac{\Delta t}{R_1 C_1} & 0 & 0 \\ 0 & F(i_k) & 0 \\ 0 & 0 & 1 \end{bmatrix} \begin{bmatrix} V_k^1 \\ h_k \\ z_k \end{bmatrix} + \begin{bmatrix} \frac{\Delta t}{C_1} & 0 \\ 0 & 1 - F(i_k) \\ -\frac{\eta_i \Delta t}{C} & 0 \end{bmatrix} \begin{bmatrix} i_k \\ M\left(z, \dot{z}\right) \end{bmatrix} \tag{2.25}$$

$$y_k = OCV(z_k) - Ri_k - V_k^1 + h_k \tag{2.26}$$

$$\theta = [R^+, R^-, R_1, C_1, M^+, M^-, \gamma] \tag{2.27}$$

The second order RC models

The second-order OCV-R-RC-RC model is as shown in 2.4 and its state and measurement equations are represented by Equation (2.28) and (2.29) respectively. This model is more accurate than the previous models while it is still simple enough to be implemented in real-time applications [14].

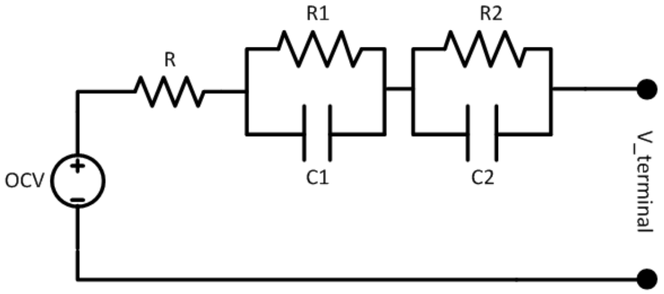

Figure 2.4: Schematic diagram of the second order RC Battery Model.

$$\begin{bmatrix} V^1_{k+1} \\ V^2_{k+1} \\ z_{k+1} \end{bmatrix} = \begin{bmatrix} 1-\frac{\Delta t}{R_1 C_1} & 0 & 0 \\ 0 & 1-\frac{\Delta t}{R_2 C_2} & 0 \\ 0 & 0 & 1 \end{bmatrix} \begin{bmatrix} V^1_k \\ V^2_k \\ z_k \end{bmatrix} + \begin{bmatrix} \frac{\Delta t}{C_1} \\ \frac{\Delta t}{C_2} \\ -\frac{\eta_i \Delta t}{C} \end{bmatrix} \begin{bmatrix} i_k \end{bmatrix} \tag{2.28}$$

$$y_k = OCV(z_k) - Ri_k - V^1_k - V^2_k \tag{2.29}$$

Where, V^2_k is the voltage drop across the second RC pair. The parameters to be optimized are shown in Equation (2.30).

$$\theta = [R^+, R^-, R_1, C_1, R_2, C_2] \tag{2.30}$$

The second order RC models with one-state hysteresis

This model is formed by adding one hysteresis state to the second order RC model. The state and measurement equations of the system are represented in Equation

(2.31) and (2.32) respectively. While the parameteric vector to be optimized is shown in Equation (2.33).

$$\begin{bmatrix} V_{k+1}^1 \\ V_{k+1}^2 \\ h_{k+1} \\ z_{k+1} \end{bmatrix} = \begin{bmatrix} 1-\frac{\Delta t}{R_1C_1} & 0 & 0 & 0 \\ 0 & 1-\frac{\Delta t}{R_2C_2} & 0 & 0 \\ 0 & 0 & F(i_k) & 0 \\ 0 & 0 & 0 & 1 \end{bmatrix} \begin{bmatrix} V_k^1 \\ V_k^2 \\ h_k \\ z_k \end{bmatrix} + \begin{bmatrix} \frac{\Delta t}{C_1} & 0 \\ \frac{\Delta t}{C_2} & 0 \\ 0 & 1-F(i_k) \\ -\frac{\eta_i \Delta t}{C} & 0 \end{bmatrix} \begin{bmatrix} i_k \\ M\left(z, \dot{z}\right) \end{bmatrix} \tag{2.31}$$

$$y_k = OCV(z_k) - Ri_k - V_k^1 - V_k^2 + h_k \tag{2.32}$$

$$\theta = [R^+, R^-, R_1, C_1, R_2, C_2, M^+, M^-, \gamma] \tag{2.33}$$

The third order RC models

The third-order OCV-R-RC-RC-RC model is shown in Figure 2.5 and the state and measurement equations of this system are represented by Equation (2.34) and (2.35) respectively. The associated parameteric vector is given in Equation (2.36). Although the complexity increases in this model, it is more accurate in capturing the dynamic behavior of the battery cell [14].

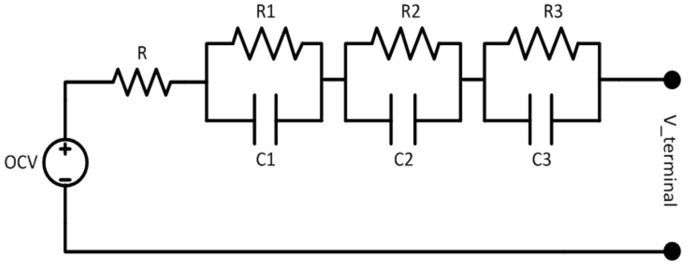

Figure 2.5: Schematic diagram of the third order RC Battery Model.

$$\begin{bmatrix} V^1_{k+1} \\ V^2_{k+1} \\ V^3_{k+1} \\ z_{k+1} \end{bmatrix} = \begin{bmatrix} 1-\frac{\Delta t}{R_1C_1} & 0 & 0 & 0 \\ 0 & 1-\frac{\Delta t}{R_2C_2} & 0 & 0 \\ 0 & 0 & 1-\frac{\Delta t}{R_3C_3} & 0 \\ 0 & 0 & 0 & 1 \end{bmatrix} \begin{bmatrix} V^1_{k} \\ V^2_{k} \\ V^3_{k} \\ z_{k} \end{bmatrix} + \begin{bmatrix} \frac{\Delta t}{C_1} \\ \frac{\Delta t}{C_2} \\ \frac{\Delta t}{C_3} \\ -\frac{\eta_i \Delta t}{C} \end{bmatrix} \begin{bmatrix} i_k \end{bmatrix} \tag{2.34}$$

$$y_k = OCV(z_k) - Ri_k - V^1_k - V^2_k - V^3_k \tag{2.35}$$

Where, V^3_k is the voltage drop across the third RC pair.

$$\theta = [R^+, R^-, R_1, C_1, R_2, C_2, R_3, C_3] \tag{2.36}$$

The third order RC models with one-state hysteresis

Similarly to the first and second order models, the third order RC model can be augmented with one state to represent the hysteresis effect [25]. The state and measurement equations of the system are represented by Equation (2.37) and (2.38) respectively.

$$\begin{bmatrix} V^1_{k+1} \\ V^2_{k+1} \\ V^3_{k+1} \\ h_{k+1} \\ z_{k+1} \end{bmatrix} = \begin{bmatrix} 1-\frac{\Delta t}{R_1C_1} & 0 & 0 & 0 & 0 \\ 0 & 1-\frac{\Delta t}{R_2C_2} & 0 & 0 & 0 \\ 0 & 0 & 1-\frac{\Delta t}{R_3C_3} & 0 & 0 \\ 0 & 0 & 0 & F(i_k) & 0 \\ 0 & 0 & 0 & 0 & 1 \end{bmatrix} \begin{bmatrix} V^1_k \\ V^2_k \\ V^3_k \\ h_k \\ z_k \end{bmatrix} + \begin{bmatrix} \frac{\Delta t}{C_1} & 0 \\ \frac{\Delta t}{C_2} & 0 \\ \frac{\Delta t}{C_3} & 0 \\ 0 & 1-F(i_k) \\ -\frac{\eta_i \Delta t}{C} & 0 \end{bmatrix} \begin{bmatrix} i_k \\ M\left(z,\dot{z}\right) \end{bmatrix} \tag{2.37}$$

$$y_k = OCV(z_k) - Ri_k - V^1_k - V^2_k - V^3_k + h_k \tag{2.38}$$

$$\theta = [R^+, R^-, R_1, C_1, R_2, C_2, R_3, C_3, M^+, M^-, \gamma] \tag{2.39}$$

2.4.4 Electrochemical battery models

Many approaches to model the electrochemical processes in the battery have been proposed in the literature. Most of the models are derived from the physics-based, electrochemical pseudo-two-dimensional (P2D) model referred to as the Doyle-Fuller-Newman model [26, 27], which is based on the porous electrode and concentrated solution theory. The primary benefit of the rigorous physics-based P2D model is the increased accuracy/precision achieved by modeling the electrochemical processes. Unfortunately, it is high in complexity, computational time, memory allocations, and not suited to real-time control. Therefore, simplifications to the P2D model are required. In the literature, numerous reduction methods have been explored, all of which have the goal of reducing the computational complexity involved in solving the physics-based electrochemical model while maintaining acceptable accuracy.

These methods can be divided into two categories. The first one is primarily focused on reducing the computational complexity involved in solving for the concentration of lithium in the solid particles of the electrodes, e.g. Subramanian et al. [28, 29, 30] developed a simplified model using the Lyapunov-Schmidt technique, perturbation techniques, volume averaging, and intuition-based simplifications. Their approach works well at low-to-moderate discharge rates but performs poorly for highly dynamic current profiles such as those encountered in hybrid- and electric-vehicle applications. Cai et al. [31] proposed an approach based on proper orthogonal decomposition, which uses a two-step approximation of the full order model; The first approximation is discretizing the governing equations and the second is truncating the number of orthogonal modes. The proposed reduced order model proved to be about seven times faster than the full order model. Forman et al. [32] used quasi-linearization and Padé approximation. This approach uses a quasi-linearized model of intercalation current to solve the model algebraic equations, then a Padé approximation of spherical diffusion is used to decrease the model complexity while maintaining a high level of accuracy. Wang et al. [15] assumed a parabolic concentration profile within the spherical particle ($c_s = a_0 + a_1 r + a_2 r^2$) formulating a solid state diffusion sub-model, which correctly captures bulk dynamics and steady state concentration gradient but otherwise neglects diffusion dynamics. It is, therefore, valid for extended operation times and low C-rates, as its inaccuracy becomes significantly compromised at higher C-rates. Smith et al. [33, 34] proposed a simplified model using the method of residue grouping. They used a nonlinear optimization technique to minimize the error in the frequency response between the 'full order' and the 'reduced order' model. The derived transfer functions are represented by a truncated series of grouped residuals with similar eigenvalues. Bhikkaji et al. [35, 36] developed a simplified model based on the Chebyshev polynomial.

The second category of model simplification is focused on reducing the electrochemical model as a whole. The primary contribution pertains to avoiding the solution of large sets of differential-algebraic equations (DAEs) of the Li^+ concentration distribution and the potential distribution of the electrolyte phase. This provides a reduced order model capable of computing in real-time. However, this strategy for model simplification leads to loss of information. The performance reduces at higher C-rates in comparison to the full order model. In general, the assumptions used for the model reduction can lead to inaccuracies if a broad C-rate range of operation is considered and if the model is not adjusted with respect to the operating conditions of the battery. Examples of this modeling approach, Haran et al. [37] originally developed the single particle model (SPM) approach for the metal hydride battery, and it was extended to the lithium system by Santhanagopalan in [25, 38]. In this model, the local volumetric current density j^{li} is constant across the electrode (anode or cathode) and equal to an average value $\bar{j}^{li}$. Rahimian et al. [39] extended the SPM by including a polynomial approximation of the electrolyte dynamics. Domenico et al. [16] presented the electrode averaging model (EAM). In literature, there are also other methodologies reported for solving the original physics-based P2D model directly.

2.5 Battery thermal managament

Thermal management of lithium ion batteries is an important consideration for a successful BMS. Operating the battery pack outside the recommended operating conditions could result in unsafe operating conditions with undesired consequences. In order to keep the battery within its safe operating range, the temperature of the cell core must be monitored and controlled.

In the literature, various strategies have been proposed for managing the temperature variations inside a cell during its operation. All of which have the goal of avoiding unsafe operating conditions. All the battery thermal management models are divided into two sub-models, heat generation model, and thermal model.

2.5.1 Heat generation model

The heat generation model is responsible for the heat generation experienced during the cell's operation due to the energy conversion losses through electrical, chemical and mass transport processes. In literature, various ways have been utilized to model the heat generation rate ranging from empirical to analytical models.

Empirical heat generation models

The Empirical approach as discussed by Kobayashi [40] measures the heat generation rate experimentally using calorimetry techniques. The empirical models are usually parameterized under a constant current load via the direct measurement of the heat generated in the cells. Al-Hallaj et al. [41] used an Accelerating Rate Calorimeter (ARC) to measure the heat generation of a cell for complete charging and discharging cycles. These measurements are mostly carried out for small battery samples, and the heat generation is scaled up to the actual battery cell size [42]. The results from the empirical heat generation methods are tabulated as a function SOC, current density, current direction, and temperature.

Analytical heat generation models

The analytical approach as discussed by Bernadi [43] calculates the heat generation rate using an energy balance that accounts for different sources of heat generation.

In chapter 4, the analytical approach will be considered in details. A detailed expression for the heat losses that accounts for all the chemical reactions, mixing processes, polarization effects and electrode kinetics is often impractical. A simplified expression derived by Berandi et al. [43] is widely used in literature. Bernardi's expression quantified the losses in an electrochemical system taking into account the enthalpy of the reactions, enthalpy of mixing, phase-change and the heat capacity.

The sum of all the heat sources is $\dot{Q}_{gen}$ as defined in equation (2.40). It consists of four different terms.

$$\dot{Q}_{gen} = \dot{Q}_{rev} + \dot{Q}_{irr} + \dot{Q}_{mix} + \dot{Q}_{sr} \tag{2.40}$$

Reversible losses The first term in equation (2.40) is the reversible losses ($\dot{Q}_{rev}$), and can be calculated as shown in (2.41)

$$\dot{Q}_{rev} = IT\frac{\partial(U_p - U_n)}{\partial T} \tag{2.41}$$

The magnitude of $\dot{Q}_{rev}$ can be either positive or negative depending on the sign of the entropic coefficient. The entropic coefficient $\partial U_{p,n}/\partial T$ quantifies the magnitude of the OCP dependency on temperature and is directly correlated with the entropy change and hence the reversible losses. A common way of calculating the entropic coefficient is to discharge the cell to a predefined SOC and wait until the cell relaxes to record the equilibrium potential and then repeat at different temperature points and different SOC points. This can either be done by keeping the SOC constant and then varying the temperature or by varying the SOC while holding the temperature constant, though the latter method results in more uncertainty [44]. The accuracy of the results depends on the number of SOC points considered. It can take extended experimental procedures to get sufficient data. Some novel approaches such as electrothermal impedance spectroscopy [45] as well as methods based on calorimetry [46] are discussed in the literature.

Irreversible losses The second term in equation (2.40) is named irreversible losses ($\dot{Q}_{irr}$) or polarization losses. Polarization is the deviation of the cell's voltage from its equilibrium voltage and can be attributed to ohmic, activation and concentration polarization [47]. The irreversible loss is quantified by how much the instantaneous cell potential deviates from the equilibrium potential, and can be calculated as follows

$$\dot{Q}_{irr} = I[V_t - (U_p - U_n)] \tag{2.42}$$

Losses induced by polarization have the biggest magnitude out of all the modes of losses.

Heat of Mixing The third term in equation (2.40) is the heat of mixing ($\dot{Q}_{mix}$), and it models the losses released or absorbed from the formation and relaxation of the concentration gradients during the operation of a lithium-ion cell. Thomas et al. [48] quantified the amount of heat of mixing for porous insertion electrodes, and concluded that its magnitude is negligible compared to the reversible and irreversible losses for well-designed cells. The heat of mixing in porous insertion electrodes can be divided into four modes (i) the concentration gradients inside the spherical particles, (ii) concentration gradients inside the bulk electrolyte, (iii) concentration gradients inside the electrolyte pores of the insertion electrode, and (iv) concentration gradients inside the bulk electrode.

Side reactions The fourth term in equation (2.40) is the heat associated with any side reactions that may occur ($\dot{Q}_{sr}$). During normal operating conditions, this term can be neglected as discussed in [43].

2.5.2 Thermal model

Thermal models are important to predict and simulate the temperature profile inside the battery during operation. The thermal model uses the heat generation rate inside the cell (as discussed in section 2.5.1) and the thermal boundary conditions in order to simulate the heat transfer mechanisms. In the literature, different approaches are proposed to model the thermal profile within a cell. These approaches can be divided into two categories:(i) lumped models, and (ii) multi-dimensions models.

Lumped models

Damay et al. [49] developed a lumped capacitance zero-dimensional thermal model. The model included one heat capacitor coupled with different modes of heat transfer throughout the cell to represent the thermal behavior of a prismatic cell. Similarly, Forgez et al. [50] employed the same technique for cylindrical cells using two heat capacitors. The lumped capacitance modeling approach will also be considered in chapter 4 due to its low computational complexity and acceptable accuracy.

Multi-dimensions models

The multi-dimensions models include coupled partial differential equations (PDE) models, linear parameter-varying state-space models, three-dimensional Finite Element Analysis (FEA) models. Smyshlyaev et al. [51] proposed an analytic solution for solving the thermal model PDEs. Whereas, Hu et al. [52] reduced the PDEs computational complexity by fitting a more complicated computational fluid dynamics (CFD) model to a linear parameter-varying state-space model. Guo et al. [53] presented a three-dimensional FEA thermal model, while Baba et al. [54] developed a full 3D thermal model that takes into account local heat generation and the spatial dependencies to obtain a full 3D temperature distribution of the cell. The FEA thermal models are very accurate; however, they require excessive computational power and detailed material properties, which limit their real-time implementation especially when fluid dynamics are considered in the cooling process.

2.5.3 Thermal model parametrization

An accurate set of parameters is required for obtaining a high-fidelity thermal model. The thermal parameters are either determined analytically or experimentally. Lin et al. [55] used detailed information about the material and geometry of the cell for analytically determining the parameters. Perez et al. [24] used the least squares optimization algorithms to fit the model to the experimental data. Lin et al. [56]

proposed an online estimation algorithm. Whereas Hu et al. [52] fitted a linear parameter-varying state-space model from a more complicated computational fluid dynamics (CFD) model to reduce the computational complexity. In Chapter 4, an experimental method involving optimization will be used instead of analytical methods as they suffer from a high level of uncertainty.

2.6 State of charge determination

The Battery Management System (BMS) and the accurate estimation of State of Charge (SOC) have been researched extensively in the past decade. SOC estimation not only provides information on battery performance but also reminds the user of the remaining useful energy in the battery. The different SOC determination techniques are considered in this section.

2.6.1 Direct measurement methods

The direct measurement methods use physical battery properties to calculate the SOC.

Measurement of the electrolyte physical properties

This method is used in lead-acid batteries. Here, a linear relationship between the electrolyte acid concentration and the SOC is established and used to determine the value of the SOC. A possible application of this method to batteries with liquid electrolyte is provided in [57].

Open circuit voltage - OCV

This method is promising for applications where the battery is allowed to rest for long periods of time as the battery terminal voltage decays with time to the Open Circuit Voltage (OCV). SOC can then be inferred from the OCV via look-up tables. However, this method cannot be used for dynamic SOC estimation, and its accuracy is adversely affected by temperature variations and hysteresis. Since the rest periods occur from time to time; this technique can be used in addition to coulomb counting. Such a combination allows the SOC to be calculated after a rest period using the OCV-SOC interrelation; this SOC can then be used as a re-calibration point for the coulomb counting method [58].

Impedance spectroscopy

Electro-Chemical Impedance Spectroscopy (EIS) is widely discussed in literature [59, 60]. It is based on establishing a baseline by measuring the cell impedances over a wide range of frequencies under different SOCs. The SOC is inferred by measuring the cell impedance values and correlating them against baseline impedance for various SOC.

2.6.2 Book-keeping methods

The book-keeping methods measure the battery current and use this information as input for calculating the state of charge.

Ampere-hour (Coulomb) counting

Ampere-hour (Coulomb) counting technique is the most common technique for calculating the SOC. Since the battery discharge and charge are directly related to the supplied and the drawn currents respectively, the idea of battery current balancing is applied as follows. If a starting (SOC_0) is known, the value of the current integral is the direct indicator for the SOC. Such that:

$$SOC = SOC_0 - \frac{1}{C_{nom}} \int_{t_0}^{t} I dt \tag{2.43}$$

where C_n is the nominal capacity, I is the discharge current and SOC_0 is the initial SOC value. Three main drawbacks of this method are:

1. Incorrect current measurement could result in a large error due to integration in equation (2.43).
2. Ampere-hour counting calculation is based on a predefined calibration point that may not always be available.
3. Not all of the current charged or discharged from the battery can be taken into account due to losses.

The first drawback can be overcome by having an accurate sensor that is often expensive. The second drawback is solved by having a predefined calibration point. The third drawback can be eliminated by adding a constant correction charging factor(η_i) to the battery at each charge/discharge cycle, where the value of (η_i) changes with the number of cycles to compensate for battery capacitance losses as follows:

$$SOC = SOC_0 - \frac{\eta_i}{C_{nom}} \int_{t_0}^{t} I dt \tag{2.44}$$

The error in Ampere-hour counting can be maintained low by defining a correction factor and defining a re-calibration point [61]. The Ah counting method [62] provides a higher accuracy than other SOC calculation methods. It is easy and reliable if the current measurement is accurate and if the re-calibration point is available.

2.6.3 Adaptive methods

Artificial neural network

SOC determination using Artificial Neural Networks (ANN) is discussed in details in [63, 64]. Since artificial neural networks can establish an input/output relationship of complex non-linear systems, SOC and SOH can readily be obtained with ANNs. An ANN is composed of neurons that are interconnected together to form a relationship between the network's input and outputs. ANN mimics the human brain and needs to be trained. The techniques and algorithms used for training of the ANN are presented in [65]. A limitation of ANN is that it requires a significant amount of data for training for all operating conditions and situations.

State estimation techniques

In the literature, several state estimation techniques have been presented to predict the battery's state of charge. The state estimation techniques require an accurate state space model for the battery where the SOC is an observable state. Plett et al. [9] used the Extended Kalman Filter (EKF) to predict the battery SOC using the behavioral models. Farag et al. [14] used the Smooth Variable Structure Filter (SVSF) to estimate the battery SOC using the equivalent circuit models. In chapter 5 a comparative study between different state estimation techniques is presented using the electrochemical model.

2.7 Battery aging mechanisms

The phenomenon of battery aging is complex to model due to its dependence on many factors either from the environment or from utilization modes as shown in [66, 67]. In literature, the aging has been mainly defined as capacity or power fading to a predefined limit, where the capacity fade is identified as loss of capacity [68], and power fade is identified as an increase in the battery internal resistance [69].

2.7.1 Aging origins

The origins for aging can be classified into two main causes [70]:

- Extreme Conditions: operating the battery under extreme conditions such as high temperature [66], or high charging rates [71].
- Normal Conditions: aging can be caused due to battery storage (calendar aging) or usage (cycling aging).

Battery aging is a result of diverse and complex processes where performance degradation takes place due to irreversible chemical reactions [72].

2.7.2 Aging models

In the literature, different models have been proposed to model the aging phenomena. The models can be divided into five categories:

- Electrochemical models: physical-based models that estimate the aging phenomena occurring in the cell [73].
- Equivalent circuit-based models: using an equivalent circuit model to model the aging phenomena [74].
- Performances based models: physical equations predict the battery aging [75].
- Analytical models with empirical fitting: involves estimation of aging parameters through experimental measurements [76].
- Statistical approach: these are mainly based on data analysis and do not require apriori knowledge [77].

2.8 Summary

The battery management system plays a major role in the energy storage systems of electric vehicles. One of the key consideration for the accuracy of the BMS is the battery model and its temperature and aging dependencies. This chapter provided a brief literature review of the battery management system, battery models, thermal models, heat generation models, state of charge estimation techniques, and cell aging mechanisms.

Different battery modeling categories are presented. The choice between these categories is a trade-off between model complexity, accuracy, and parameterization effort. The models can be classified into three categories of increasing complexity: behavioral, equivalent circuit, and electrochemical models. Currently, the equivalent circuit models are commonly used in the BMS because of their low computational complexity and acceptable accuracy. However, they are not capable of describing the battery's internal physical behavior.

An accurate thermal-electrical battery model is required in order to operate the energy storage system in a temperature range which is characterized by slow aging progress, high efficiency, and performance. The thermal models consist of two submodels, namely the heat generation model, and the heat transfer model. The heat generation model is responsible for the rate of heat generation inside the battery's core during operation and can be divided into four primary sources: reversible losses, irreversible losses, heat of mixing losses, and side reaction losses. The heat transfer models are necessary to predict and simulate the temperature profile inside the battery. Finally, various state of charges estimation techniques and battery aging mechanisms are presented.

In this dissertation, a new formulation for the the reduced-order, electrode-average model (EAM) is developed. The new formulation reduces the CPU run-time while maintaining accuracy. The electrochemical model is then augmented with thermal model and heat generation model in order to be capable of predicting the cell's terminal voltage and core temperature over a broad range of temperatures and state of charges. Finally, different model-based nonlinear state of charge estimation strategies were used to estimate the state of charge of the battery.

Chapter 3

Continuous piecewise-linear, reduced-order electrochemical model for lithium-ion batteries in real-time applications [1]

3.1 Abstract

Model-order reduction and minimization of the CPU run-time while maintaining the model accuracy are critical requirements for real-time implementation of lithium-ion

---

[1] Mohammed Farag, Matthias Fleckenstein, Saeid Habibi
Continuous piecewise-linear, reduced-order electrochemical model for lithium-ion batteries in real-time applications
Journal of Power Sources, Volume 342, 28 February 2017, Pages 351-362, ISSN 0378-7753, http://dx.doi.org/10.1016/j.jpowsour.2016.12.044.
http://www.sciencedirect.com/science/article/pii/S0378775316317396

electrochemical battery models. In this paper, an isothermal, continuous, piecewise-linear, electrode-average model is developed by using an optimal knot placement technique. The proposed model reduces the univariate nonlinear function of the electrode's open circuit potential dependence on the state of charge to continuous piecewise regions. The parameterization experiments were chosen to provide a trade-off between extensive experimental characterization techniques and purely identifying all parameters using optimization techniques. The model is then parameterized in each continuous, piecewise-linear, region. Applying the proposed technique cuts down the CPU run-time by around 20%, compared to the reduced-order, electrode-average model. Finally, the model validation against real-time driving profiles (FTP-72, WLTP) demonstrates the ability of the model to predict the cell voltage accurately with less than 2% error.

3.2 Introduction

In the past few years, automobile manufacturers have gone through the initial adoption phase of electric mobility. The gradually increasing momentum behind electric vehicles (EV) adoption suggests that electrified storage systems will play an important role in electric mobility going forward. Lithium ion batteries have become one of the most attractive alternatives for electric vehicles' energy storage systems due to their light weight, high specific energy, low self-discharge rate, and non-memory effect, etc. [6]. To fully benefit from a lithium-ion energy storage system and avoid its physical limitations, an accurate battery management system (BMS) is required. In EV, the BMS is responsible for performance management which includes -but is not limited to- state of charge (SOC), state of health (SOH), and state of function

(SOF) estimation algorithms, as well as power management, thermal management, and so forth. One of the key issues for successful BMS implementation is the battery model. A robust, accurate, and high fidelity battery model is required to mimic the battery dynamic behavior in a harsh environment.

In the literature, numerous battery models have been reported. The choice between these models is a trade-off between model complexity, accuracy, and parameterization effort. The models can be classified into three categories of increasing complexity: behavioral (or black-box) [7, 8, 9, 10], equivalent circuit [11, 12, 13, 14], and finally detailed electrochemical (physics-based) models. Currently, the equivalent circuit models are commonly used in the BMS because of their low computational complexity and acceptable accuracy. However, they are not capable of describing the battery's internal physical behavior.

Many approaches to model the electrochemical processes in the battery have been proposed in the literature. Most of the models are derived from the physics-based, electrochemical pseudo-two-dimensional (P2D) model developed by Doyle-Fuller-Newman model [26, 27], which is based on the porous electrode and concentrated solution theory. The primary gain of the rigorous physics-based P2D model is the increased accuracy/precision achieved by modeling the electrochemical processes. Unfortunately, it is high in complexity, computational time, memory allocations, and real-time control. Therefore, simplification of the P2D model is required. In the literature, numerous reduction methods have been explored, all of which have the goal of reducing the computational complexity involved in solving the physics-based electrochemical model while maintaining acceptable accuracy.

These methods can be divided into two categories. The first one is primarily focused on reducing the computational complexity involved in solving for the concentration of lithium in the solid particles of the electrodes, e.g. Subramanian et al. [28, 29, 30] developed a simplified model using the Liapunov-Schmidt technique, perturbation techniques, volume averaging, and intuition-based simplifications. Their approach works well at low-to-moderate discharge rates but performs poorly for highly dynamic current profiles such as those encountered in hybrid- and electric-vehicle applications. Cai et al. [31] proposed an approach based on proper orthogonal decomposition, which uses a two-step approximation of the full order model; The first approximation is discretizing the governing equations and the second is truncating the number of orthogonal modes. The proposed reduced order model proved to be about seven times faster than the full order model. Forman et al. [32] used quasi-linearization and Padé approximation. This approach uses a quasi-linearized model of intercalation current to solve the model algebraic equations, then a Padé approximation of spherical diffusion is used to decrease the model complexity while maintaining a high level of accuracy. Wang et al. [15] assumed a parabolic concentration profile within the spherical particle ($c_s = a_0 + a_1 r + a_2 r^2$) formulating a solid state diffusion submodel, which correctly captures bulk dynamics and steady state concentration gradient but otherwise neglects diffusion dynamics. It is, therefore, valid for extended operation times and low C-rates, as its inaccuracies become significant at higher C-rates. Smith et al. [33, 34] proposed a simplified model using the method of residue grouping. They used a nonlinear optimization technique to minimize the error in the frequency domain response between the 'full order' and 'reduced order' model. The derived transfer functions are represented by a truncated series of grouped residues with similar eigenvalues. Bhikkaji et al. [35, 36] developed a simplified model based on Chebyshev polynomial.

The second category of model simplification is focused on reducing the electrochemical model as a whole. The primary contribution pertains to avoiding the solution of large sets of differential-algebraic equations (DAEs) of the Li^+ concentration distribution and the potential distribution of the electrolyte phase. This provides a reduced model capable of computing in real-time. However, this strategy for model simplification leads to loss of information. The performance reduces at higher C-rates in comparison to the full order model. In general, the assumptions used for the model reduction can lead to inaccuracies if a broad C-rate range of operation is considered and if the model is not adjusted with respect to the operating conditions of the battery. Examples of this modeling approach, Haran et al. [37] originally developed the single particle model (SPM) approach for the metal hydride battery, and it was extended to the lithium system by Santhanagopalan in [25, 38]. In this model, the local volumetric current density j^{li} is constant across the electrode (anode or cathode) and equal to an average value $\bar{j}^{li}$. Rahimian et al. [39] extended the SPM by including a polynomial approximation of the electrolyte dynamics. Domenico et al. [16] presented the electrode averaging model (EAM). In literature, there are also other methodologies reported for solving the original physics-based P2D model directly.

This paper contributes to the literature above by developing three unique improvements to the reduced-order electrode average electrochemical model presented by Domenico et al. [16]. The first contribution is a continuous piecewise linearized (CPWL) technique that aids in efficiently running the model in real time applications. The second contribution is an optimal knot-placement optimization technique for the continuous piecewise linearized electrode averaged model (CPWL-EAM) using the genetic algorithm (GA). The third contribution is a parameter-grouping approach that helps in reducing the parameterization efforts for the EAM and the CPWL-EAM. First, the optimal knot locations are obtained using the GA to minimize the residual error. The CPWL-EAM parameters are then identified in order to minimize the error between the model terminal voltage output and the experimental data. The model is then validated using battery voltage, current, and temperature measurements against real-time driving cycles.

Paper structure First, the full-order electrochemical model is briefly introduced. Next, the continuous piecewise linearization technique is presented. Then, the battery parameter identification procedure and the experimental setup are illustrated. The model validation against two different real-time driving cycles is then shown. Finally, the results and discussion are presented.

3.3 Electrochemical battery modeling

3.3.1 Operating principles of lithium-ion batteries

A battery converts chemical energy into electrical energy and vice versa. The basic setup of a battery cell consists of four main parts: the positive electrode, the separator, the electrolyte, and the negative electrode, as shown in Figure 3.1.

The positive and negative electrodes are referred to as the cathode and the anode. The battery is connected to an external load using current collector plates. In the case of Li-ion cells, a copper collector is used in the negative electrode while an aluminum collector is used for the positive electrode.

The anode is the electrode capable of supplying electrons to the load. The anode is usually made up of a mixture of carbon (e.g. Li_xC_6), the cathode is typically made of metal oxides (ex. $LiCoO_2$ or $LiMn_2O_4$), while the electrolyte can be made of a salt-containing solvent mixture, polymer, or solid materials (e.g. $LiPF_6$), polymer or solid materials. In the case of solid or polymer materials, the electrolyte will also act as a separator. The separator is a porous membrane allowing the transfer of lithium ions between the electrodes, but which serves as a barrier to electrons. It prevents the occurrence of a short-circuit and thermal run away, while at the same time offering negligible resistance to the flow of ions between the electrodes.

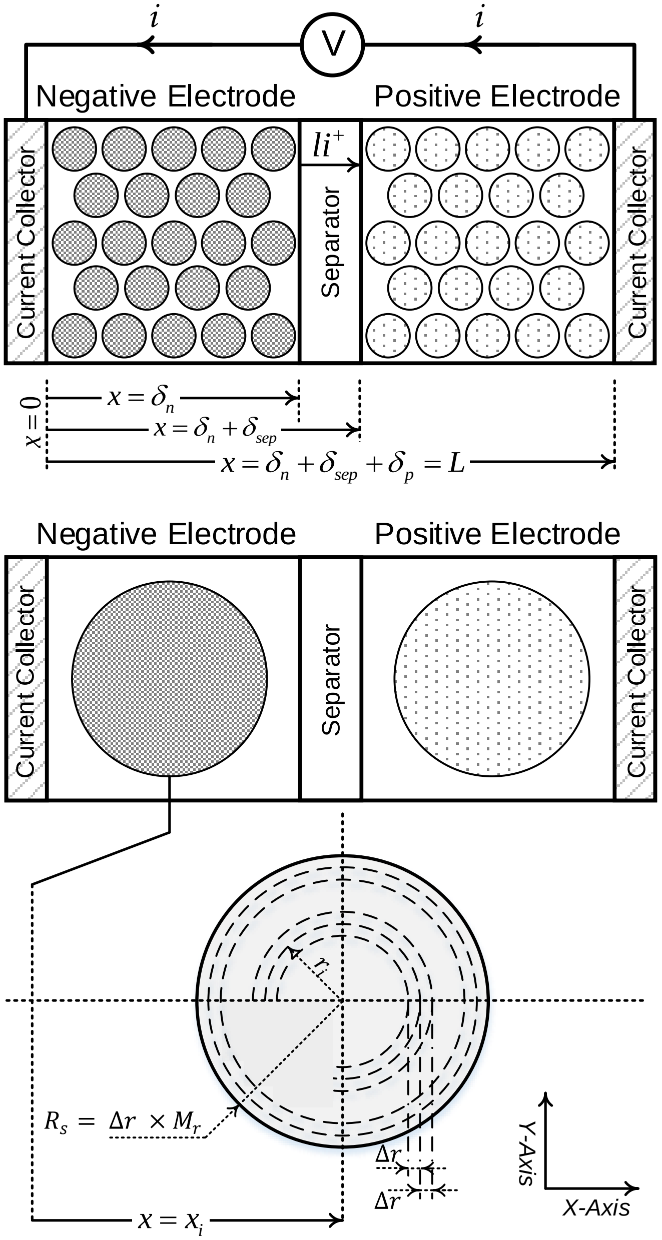

Figure 3.1: Schematic representation of the Li-ion battery operation principles and the single particle model simplification.

3.3.2 Model mathematical formulation

Relationship between concentrations and currents

The mathematical equations governing the charge and mass conservation in the solid and electrolyte phases is summarized in this section.

Mass transport in the solid phase The electrode model is based on the porous electrode theory, and the lithium-ion concentration in a single spherical particle is described by Fick's law of diffusion [25]

$$\frac{\partial c_s^{n,p}(x,r,t)}{\partial t} = \frac{D_s}{r^2}\frac{\partial}{\partial r}\left[r^2 \frac{\partial c_s^{n,p}(x,r,t)}{\partial r}\right] \tag{3.1}$$

where $c_s(x,r,t) : (0,L) \times (0,R_s^{n,p}) \times (t_0,t) \rightarrow [0, c_{s,max}^{n,p}]$ is the concentration of Li^+ in the solid particles, as shown in Figure 3.1. At the particle surface, the rate at which ions exit or enter the particle is proportional to the volumetric rate of chemical reaction j^{li}, while at the center of the particle the rate is equal to zero, written as the boundary conditions (BC):

$$\left.\frac{\partial c_s^{n,p}}{\partial r}\right|_{r=0} = 0 \quad \text{and} \quad \left.\frac{\partial c_s^{n,p}}{\partial r}\right|_{r=R_s^{n,p}} = \frac{-j^{li}}{D_s a_s F} \tag{3.2}$$

With initial conditions (IC):

$$c_s^{n,p}\left(x,r,t_0\right) = c_{s_0}^{n,p}\left(x,r\right) \tag{3.3}$$

Mass transport in the electrolyte The Li^+ concentration in the electrolyte changes due to the flow of ions and the current. It can be described by Fick's law of diffusion along the coordinate between the electrodes, with the mass transport between the electrodes treated as being effectively homogeneous at all coordinates in the plane normal to the inter-electrode coordinate.

$$\frac{\partial \varepsilon_e c_e(x,t)}{\partial t} = \frac{\partial}{\partial x}\left(D_e^{eff}\frac{\partial c_e(x,t)}{\partial t}\right) + \frac{1-t_0^+}{F} j^{li} \tag{3.4}$$

Where $c_e(x,t)$ is the concentration of Li^+ in the electrolyte and ε_e and D_e^{eff} are domain-dependent parameters (anode, cathode, separator). The Bruggeman's relation $D_e^{eff} = D_e \times \varepsilon_e^{1.5}$ accounts for the tortuous path of Li^+ transport through the porous electrodes and separator. Ensuring zero flux at the current collector and continuity of concentration and flux through the adjoining domains within the cell, written as boundary conditions:

$$\left.\frac{\partial c_e^n}{\partial x}\right|_{x=0} = 0 \quad \text{and} \quad \left.\frac{\partial c_e^p}{\partial x}\right|_{x=L} = 0 \tag{3.5}$$

With initial conditions:

$$c_e(x,t_0) = c_{e_0}(x) \tag{3.6}$$

Relationship between potential and currents

Potential in the solid electrodes The electrical potential in the electrodes ϕ_s is derived from the extended Ohm's law:

$$\frac{\partial}{\partial x}\left(\sigma^{eff}\frac{\partial}{\partial x}\phi_s(x,t)\right) - j^{li} = 0 \tag{3.7}$$

The potentials at the current collectors ($x = 0$ and $x = L$) are proportional to the applied current, I and zero at the separator, written as boundary conditions (where

A is the cross-sectional area of the cell):

$$
\begin{aligned}
-\sigma^{eff}\frac{\partial}{\partial x}\phi_s(x,t)\bigg|_{x=0} &= -\sigma^{eff}\frac{\partial}{\partial x}\phi_s(x,t)\bigg|_{x=L} = \frac{I}{A} \\
\frac{\partial}{\partial x}\phi_s(x,t)\bigg|_{x=\delta_n} &= \frac{\partial}{\partial x}\phi_s(x,t)\bigg|_{x=\delta_n+\delta_{sep}} = 0
\end{aligned}
\tag{3.8}
$$

Potential in the electrolyte The electrical potential in the electrolyte ϕ_e is derived from the charge conservation law:

$$
\frac{\partial}{\partial x}\left(\kappa^{eff}\frac{\partial}{\partial x}\phi_e(x,t)\right) + \frac{\partial}{\partial x}\left(\kappa_D^{eff}\frac{\partial}{\partial x}\ln c_e\right) + j^{li} = 0 \tag{3.9}
$$

With boundary conditions:

$$
\frac{\partial}{\partial x}\phi_e(x,t)\bigg|_{x=0} = \frac{\partial}{\partial x}\phi_e(x,t)\bigg|_{x=L} = 0 \tag{3.10}
$$

Butler-Volmer kinetics equations

The volumetric rate of chemical reaction is governed by the Butler-Volmer current density equation. This equation links the reaction rate to the phase potentials and is described as:

$$
j^{li} = a_s j_0\left[\exp\left(\frac{\alpha_a F}{RT}\eta\right) - \exp\left(-\frac{\alpha_c F}{RT}\eta\right)\right] \tag{3.11}
$$

The overpotential η is defined as the difference between the cell's overpotential and its charge/discharge voltage. It is responsible for driving the electrochemical reaction, and can be calculated as follows:

$$
\eta = \phi_s - \phi_e - U(c_{se}) \tag{3.12}
$$

Where $U(c_{se})$ is the open circuit potential and the coefficient j_0 is a function of the surface electrolyte concentration c_{se} according to equation (3.13).

$$j_0 = (c_e)^{\alpha_a} \left(c^{n,p}_{s,\max} - c^{n,p}_{se}\right)^{\alpha_a} \left(c^{n,p}_{se}\right)^{\alpha_c} \tag{3.13}$$

Cell potential equations

The cell potential, V, across the cell terminals is determined as follows:

$$V = \phi_s(x = L) - \phi_s(x = 0) - R_f \frac{I}{A} \tag{3.14}$$

The mathematical formulation, describing the full order electrochemical model equation (3.1) to (3.14), is presented in Figure 3.2.

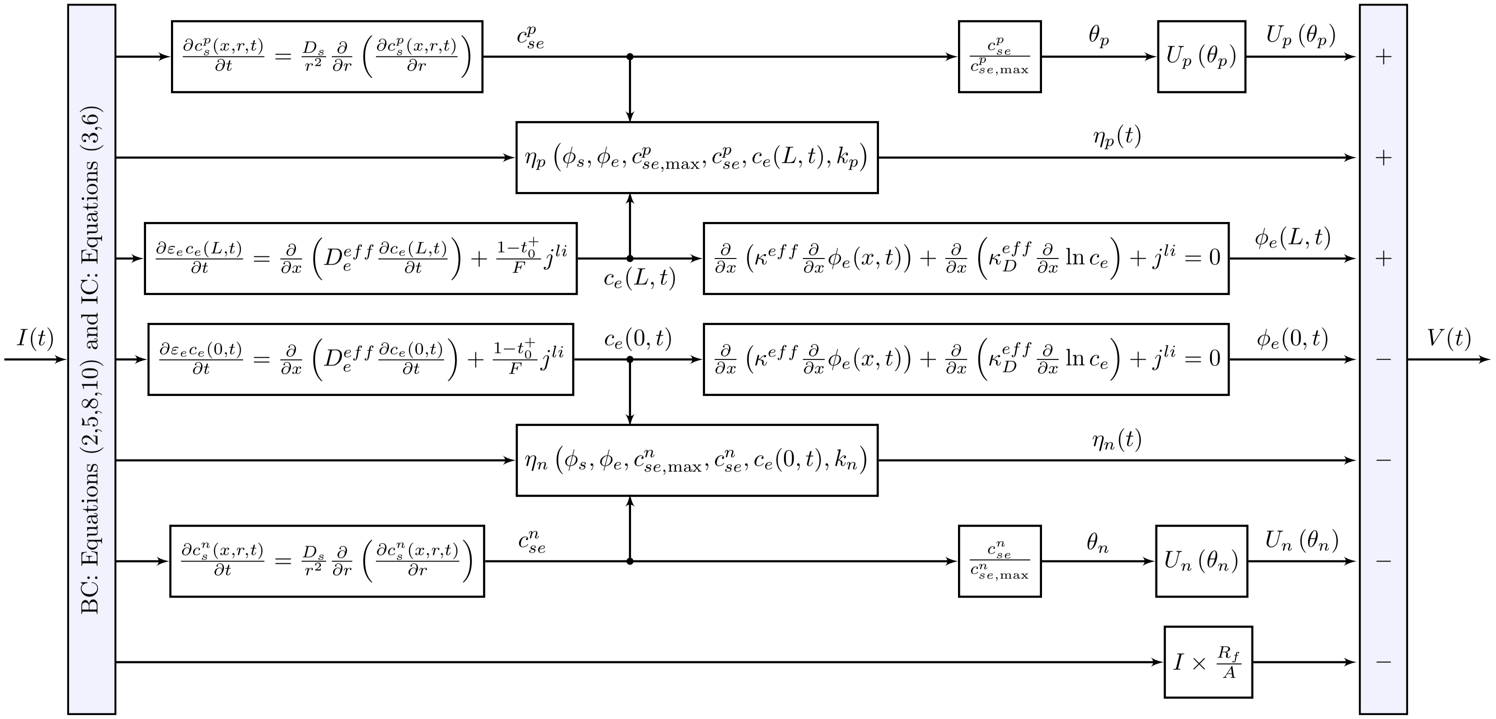

Figure 3.2: Block diagram representations for the coupled nonlinear partial differential equations in the full order electrochemical model.

3.3.3 Model reduction

The full-order model (FOM) is highly accurate; however it requires extensive computational time and onboard memory allocation, which limits its utility for real-time applications. Therefore, reduction of the FOM has been carried out by simplifying the set of FOM equations for ion concentration and potential in electrode and electrolytes. In this section, some assumptions and simplifications to the FOM are considered in order to obtain a Reduced Order Model (ROM) as shown in Figure 3.3.

Model reduction assumptions

The FOM equations represented in equations (3.1) to (3.14) are simplified in order to be implemented in real-time applications. The simplification assumptions are summarized in Table 3.1. As a result of these reductions, a single particle from each electrode (anode and cathode) can describe the diffusion dynamics.

Conservation Equation	Assumptions
ROM-Ion concentration in the electrodes	
$$\frac{\partial c_s^{n,p}(r,t)}{\partial t} = \frac{D_s}{r^2}\frac{\partial}{\partial r}\left[r^2\frac{\partial c_s^{n,p}(r,t)}{\partial r}\right] \quad (3.15)$$	Since only one particle is to be considered from the anode and the cathode, the x-dimension has been ignored
$$c_e(x,t) = \bar{c}_e \quad (3.16)$$	The lithium concentration in electrolyte c_e is assumed to be constant, uniform, and equal to an average value
ROM-Ion concentration in the electrolyte	
$$\frac{\partial}{\partial x}\left(\sigma^{eff}\frac{\partial}{\partial x}\phi_s(x,t)\right) = \bar{j}_{n,p}^{li} \quad (3.17)$$	
$$\frac{\partial}{\partial x}\left(\kappa^{eff}\frac{\partial}{\partial x}\phi_e(x,t)\right) = -\bar{j}_{n,p}^{li} \quad (3.18)$$	The lithium concentration in electrolyte c_e is assumed to be constant, uniform, and equal to an average value
ROM-Butler-Volmer kinetics equation	
$$\bar{j}_{n,p}^{li} = \frac{I}{A\delta_{n,p}} \quad (3.19)$$	The lithium concentration in electrolyte c_e is assumed to be constant, and one particle is to be considered from the each electrode. Hence, the spatial dependence of the Butler-Volmer equation is removed

Table 3.1: Final set of reduced-order model equations and underlying assumptions.

Reduced-order model

The FOM set of equations is simplified due to the previous assumptions. The reduced-order, electrode-averaged model (ROM) is summarized in equation (3.15) to (3.19). Its terminal voltage can be calculated by substituting equation (3.12) in equation (3.14), as derived in [25]:

$$V(t) = (\bar{\eta}_p - \bar{\eta}_n) + \left(\bar{\phi}_e^p - \bar{\phi}_e^n\right) + [U_p(\theta_p) - U_n(\theta_n)] - R_f \frac{I}{A} \tag{3.20}$$

where $\bar{\eta}_p - \bar{\eta}_n$ is the difference between the positive and negative electrode overpotentials, and can be calculated by substituting equation (3.19) in (3.11) as shown below:

$$\bar{\eta}_p - \bar{\eta}_n = \frac{RT}{\alpha_a F} \ln \frac{\xi_p + \sqrt{\xi_p^2 + 1}}{\xi_n + \sqrt{\xi_n^2 + 1}} \quad where \quad \xi_{n,p} = \frac{\bar{j}^{li}_{n,p}}{2 a_s j_0} \tag{3.21}$$

$\bar{\phi}_e^p - \bar{\phi}_e^n$ is the difference between the positive and negative terminals electrolyte potentials, and can be represented as derived in [25]:

$$\bar{\phi}_e^p - \bar{\phi}_e^n = -\frac{I}{2A\kappa^{eff}} \left(\delta_n + 2\delta_{sep} + \delta_p\right) \tag{3.22}$$

Finally, $U_p(\theta_p) - U_n(\theta_n)$ is the difference between the open circuit voltage for the positive and negative electrolyte. The stoichiometry ratio $\theta_{n,p}$ is the normalized solid-electrolyte interface concentration for the negative and positives electrodes respectively.

$$\theta_{n,p} = \frac{\bar{c}^{n,p}_{s,e}}{c^{n,p}_{s,max}} \tag{3.23}$$

where $\bar{c}_s^{n,p}$ is the average bulk concentration, and can be obtained by calculating the total concentration volumetric average V_s.

$$\bar{c}_s^{n,p}(t) = \frac{1}{V_s}\int_0^{R_{n,p}} c_s^{n,p}(r,t)dV_s \tag{3.24}$$

3.3.4 Capacity model mathematical formulation

In this paper, the battery nominal capacity C_{nom} is determined by the mass of active material contained in a fully charged cell. It can be measured by calculating the maximum number of ampere-hours that can be drawn from the fully charged battery at room temperature (293 K) and very low C-rate (C/25). The volumetric averaged Li concentration can be determined by substituting $V_s = 4\pi R_s^3/3$ and $dV_s = 4\pi r^2 dr$ in equation (3.24).

$$\bar{c}_s^{n,p}(t) = \frac{3}{R_s^3}\int_0^{R_s} r^2 c_s^{n,p}(r,t)dr \tag{3.25}$$

By using the boundary conditions in equations (3.2) and substituting equation (3.19) into equation (3.2), the volumetric averaged Li concentration dynamics in equation (3.25) become [78]:

$$\bar{c}_s^{n,p}(t) = \frac{3D_s}{R_s^{n,p}}\left[R_s^{2_{n,p}}\partial c_s(R_s^{n,p},t)\right] = \frac{I}{\delta_{n,p}A\varepsilon_s^{n,p}F} \tag{3.26}$$

The state of charge is defined as

$$SOC = \frac{1}{C_{nom}(Ah)}\int_0^t I(\tau)d\tau \tag{3.27}$$

assuming the initial state of charge $SOC(t=0)=0$ and $I(t)$ is the applied current with $I>0$ during charge. SOC can be defined as

$$SOC=\frac{\theta_{n,p}-\theta_{0\%}}{\theta_{100\%}-\theta_{0\%}} \tag{3.28}$$

Using equations (3.26), (3.27), and (3.28), the capacity is defined as

$$C_{nom}=\frac{AF\delta_{n,p}\varepsilon_s^{n,p}c_{s,\max}^{n,p}[\theta_{100\%}^{n,p}-\theta_{0\%}^{n,p}]}{3600}, \qquad [\text{Ah}] \tag{3.29}$$

3.3.5 Discretization method

The governing PDEs of the ROM constitute the building blocks of the battery model. To be useful for control and systems engineering, the PDEs must be discretized in space to reduce them to coupled multiple ordinary differential equations (ODEs) in the time domain.

Finite difference method

The Finite Difference Method (FDM) is the simplest and the most commonly used approach to the solution of the diffusion equations found in battery models for real-time applications. By using the central finite difference method for the radial dimension r, it is possible to describe the spherical PDE by a set of ordinary differential equations (ODE). Equation (3.15) can be written as

$$\frac{\partial c_s(r,t)}{\partial t}=D_s\left(\frac{\partial^2 c_s}{\partial r^2}+\frac{2\partial c_s}{r\partial r}\right) \tag{3.30}$$

By using the CFDM, and discretizing the solid spherical particle into M_r shells along the radial dimension r as shown in Figure 3.1, such that $R_s = \Delta r \times (M_r)$, and defining $q = 1, ..., M_{r-1}$ equation (3.30) becomes

$$\dot{c}_s^{n,p}\big|_q = \frac{D_s}{\Delta r^2}\left[\left(c_s^{n,p}\big|_{q+1} - 2\,c_s^{n,p}\big|_q + c_s^{n,p}\big|_{q-1}\right) + \frac{\Delta r}{r_q}\left(c_s^{n,p}\big|_{q+1} - c_s^{n,p}\big|_{q-1}\right)\right] \tag{3.31}$$

By substituting with $r_q = q \times \Delta r$ and rearranging, equation (3.31) becomes

$$\dot{c}_s^{n,p}\big|_q = \frac{D_s}{\Delta r^2}\left[\left(\frac{q-1}{q}\right) c_s^{n,p}\big|_{q-1} - 2\,c_s^{n,p}\big|_q + \left(\frac{q+1}{q}\right) c_s^{n,p}\big|_{q+1}\right] \tag{3.32}$$

The boundary condition equations (3.2) can be rewritten accordingly:

$$c_s^{n,p}\big|_0 = c_s^{n,p}\big|_1 \tag{3.33}$$

$$c_s^{n,p}\big|_{M_r} = c_s^{n,p}\big|_{M_{r-1}} + \Delta r \frac{-\bar{\jmath}^{li}}{F a_s D_s} = c_{se}^{n,p} \tag{3.34}$$

By substituting with the boundary conditions equations (3.33) and (3.34), and rearranging, equation (3.32) becomes

$$\dot{c}_s^{n,p} = \begin{cases} \Psi\left[-2\,c_s^{n,p}\big|_q + \left(\frac{q+1}{q}\right) c_s^{n,p}\big|_{q+1}\right] & : q = 1 \\ \Psi\left[\left(\frac{q-1}{q}\right) c_s^{n,p}\big|_{q-1} - 2\,c_s^{n,p}\big|_q + \left(\frac{q+1}{q}\right) c_s^{n,p}\big|_{q+1}\right] & : 2 \leq q \leq M_r - 2 \\ \Psi\left[\left(\frac{q-1}{q}\right) c_s^{n,p}\big|_{q-1} - \left(\frac{q-1}{q}\right) c_s^{n,p}\big|_q - \frac{\mathrm{Z}}{\Psi}\left(\frac{q+1}{q}\right) \bar{\jmath}^{li}\right] & : q = M_r - 1 \end{cases} \tag{3.35}$$

where $\Psi = D_s/\Delta r^2$ and $\mathrm{Z} = 1/(\Delta r \times a_s \times F)$. The lithium concentration in the solid particle at the outer shell when $r = M_r$ is referred to as the lithium concentration at the solid-electrolyte interface $c_{se}^{n,p}$.

State space representation

With the above approximations for the mass conservation equation and its boundary conditions, a state space representation for equations (3.31) to (3.35) can be formulated as follows:

$$\dot{c}_s^{n,p} = \mathbf{A} c_s^{n,p} + \mathbf{B} j^{li} \tag{3.36}$$

$$c_{se}^{n,p} = c_s^{n,p}|_{M_r} = c_s^{n,p}|_{M_r - 1} + \mathbf{D} j^{li} \tag{3.37}$$

The state space matrices, A, B, and D, are obtained as follows:

$$\mathbf{A} = \Psi \begin{bmatrix} -2 & \frac{q+1}{q} & 0 & \cdots & 0 & 0 \\ \frac{q-1}{q} & -2 & \ddots & & 0 & 0 \\ 0 & \ddots & \ddots & \ddots & & \vdots \\ \vdots & & \ddots & \ddots & \ddots & 0 \\ 0 & 0 & & \ddots & -2 & \frac{q+1}{q} \\ 0 & 0 & \cdots & 0 & \frac{q-1}{q} & -\frac{q-1}{q} \end{bmatrix} \tag{3.38}$$

$$\mathbf{B} = \mathrm{Z} \begin{bmatrix} 0 \\ 0 \\ 0 \\ \vdots \\ \vdots \\ -\frac{q+1}{q} \end{bmatrix} \tag{3.39}$$

$$\mathbf{D} = -\frac{\mathrm{Z}}{\Psi} \tag{3.40}$$

3.3.6 Model parameter grouping

The ROM battery voltage equation can be rewritten by substituting equation (3.21), (3.22), (3.23) in equation (3.20) as shown below:

$$V(t) = [U_p(\theta_p) - U_n(\theta_n)] + \vartheta_\eta^{n,p}(\theta_{n,p}, I) - IK_{res} \tag{3.41a}$$

$$where \quad K_{res} = \frac{1}{A}\left[R_f + \frac{(\delta_n + 2\delta_{sep} + \delta_p)}{2\kappa^{eff}}\right] \tag{3.41b}$$

Where K_{res} is a term that accounts for the increase in ohmic resistance during a charge or discharge current pulse related to the poor electronic conductivity of the cell chemistry.

By substituting $a_s^{n,p} = 3\varepsilon_s^{n,p}/R_s^{n,p}$, and $\alpha_a = \alpha_c = 0.5$ from Table 3.3, equation

(3.21) can be written as follows:

$$\vartheta_{\eta}^{n,p}(\theta_{p,n}, I) = \bar{\eta}_p - \bar{\eta}_n = \frac{RT}{\alpha_a F} \ln \frac{\xi_p + \sqrt{\xi_p^2 + 1}}{\xi_n + \sqrt{\xi_n^2 + 1}} \tag{3.42a}$$

$$where \quad \xi_{n,p} = \Omega^{n,p} \frac{I}{\left(c_{s,\max}^{n,p} c_{se}^{n,p} - c_{se}^{n,p^2}\right)^{0.5}} \tag{3.42b}$$

$$and \quad \Omega^{n,p} = \frac{R_s^{n,p}}{6A\delta_{n,p}\varepsilon_s^{n,p}(\bar{c}_e)^{0.5}} \tag{3.42c}$$

Where $\Omega^{n,p}$ is a constant term which accounts for the variation of the average electrolyte concentration.

After introducing $\Omega^{n,p}$ and K_{res}, the new set of equations are described in Figure 3.3, where the blue-colored constants represent the model parameters.

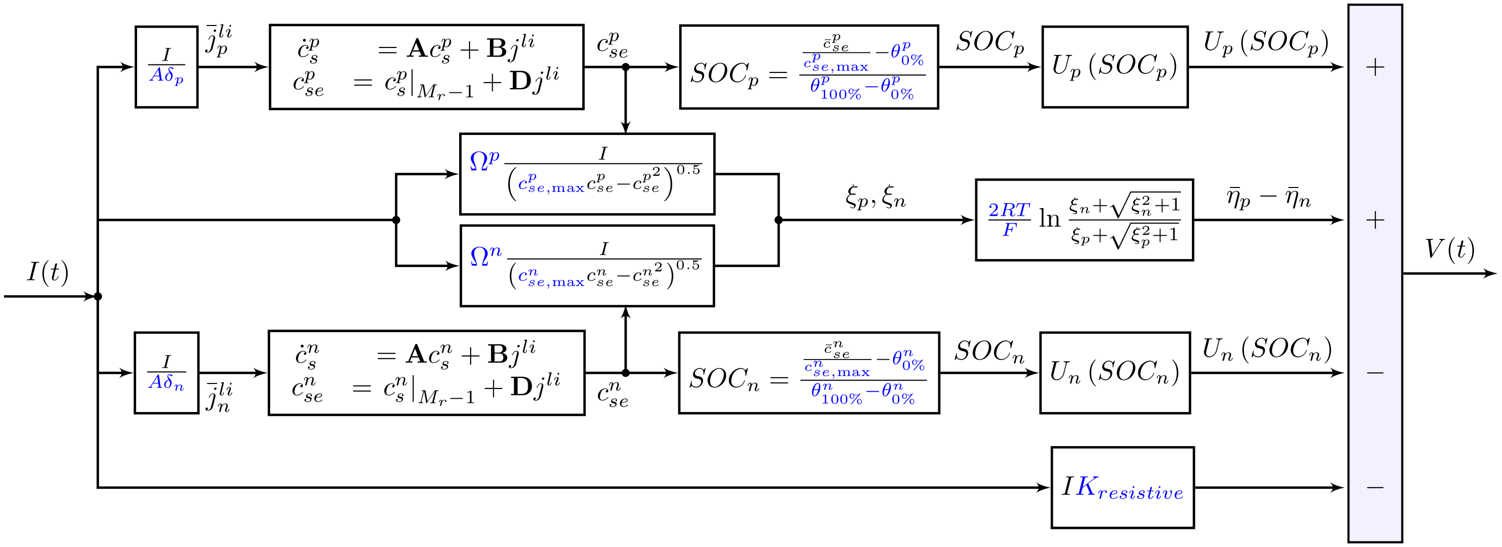

Figure 3.3: Block diagram representation for the reduced-order, electrode-average model with $\Omega^{n,p}$ and K_{res}.

Equations (3.35), which describe the lithium-ion concentration in a single spherical particle, are linear time-invariant (LTI). The nonlinearity in the output equation (3.41) is due to the open circuit potential term $[U_p(SOC_p) - U_n(SOC_n)]$ and the over-potential difference term $\vartheta_\eta^{n,p}(\theta_{p,n}, I)$. The open circuit potential term is a univariate, nonlinear function of the cell state of charge $U_{n,p}(SOC_{n,p})$. Reducing this term to a CPWL regions while maintaining accuracy aids in reducing the computational complexity of the model.

3.4 Continuous piecewise linearization

This sections will present the main contribution of this paper, the use of piecewise linearization techniques to reduce the system complexity.

3.4.1 Background

In the literature, Qingzhi et al. [79] used a cubic spline regression model to fit the experimental open-circuit potential (OCP) curves of two intercalation electrodes of a lithium-ion battery. In this paper, a method is presented for constructing CPWL regions of the experimentally measured OCP data using polynomials of the first order by a stochastic global solution of the resulting mathematical problem. Due to constraints in real time applications, the proposed technique must maintain the continuity and smoothness of the OCP curve at the knot positions.

Pittman et al. [80] have proposed an algorithm that attempts to stochastically find the global solution to an optimization problem that not only minimizes the sum of squared errors (SSE) but also chooses the optimal number of knots that maximizes the information content in each knot. The algorithm proposed in the current work is a modified form of Pittman's algorithm since the optimization problem being solved is more restrictive. First, the number of knots must be known and specified in advance. Second, the knots are not completely free on the fitting interval, but rather are restricted to be unique and in order between the values in the finite set of measurements.

A two-stage framework of knot placement is proposed. We start with an outline of the algorithm, then the knot placement strategy and the genetic algorithm (GA) optimization model are described, respectively.

3.4.2 Problem formulation and implementation

The open circuit potential as a function of state of charge, $U_{n,p}(SOC_{n,p})$, is a univariate, nonlinear function where $SOC_{n,p} \in [SOC^{0\%}_{n,p}, SOC^{100\%}_{n,p}]$. This nonlinear function has N CPWL functions $\omega_i(\theta)$ within its domain, where λ is a pre-specified number that represents the knot points. Each line segment can be defined as follows:

$$\omega_i(SOC) = \frac{U(\lambda_i) - U(\lambda_{i-1})}{\lambda_i - \lambda_{i-1}}(SOC - \lambda_{i-1}) + U(\lambda_{i-1}) \quad \forall \quad \lambda_{i-1} \leq SOC \leq \lambda_i \tag{3.43}$$

Where λ_i are knot points in $[SOC^{0\%}, SOC^{100\%}]$ and $i = 1, ..., N$. The first and the last knot points are fixed at the boundaries, that is, $\lambda_0 = SOC^{0\%}, \lambda_N = SOC^{100\%}$. Also, the knot points are ordered and unique: $\lambda_i > \lambda_{i-1}$ for $i = 1, ..., N$. To find the optimal placements for the knot points $\lambda_1, ..., \lambda_{n-1}$, such that the overall squared-approximation error err is minimized. The optimization objective function is defined as follows:

$$\min_{\lambda_1,.......\lambda_{N-1}} \left\{ err = \int\limits_{SOC^{0\%}}^{SOC^{100\%}} [U(SOC) - \omega_i(SOC)]^2 dSOC \right\} \tag{3.44}$$

The optimization problem can be described as follows:

$$\min_{\lambda_1,\ldots,\lambda_{N-1}} err(SOC) \tag{3.45a}$$

$$s.t. \quad \frac{d}{dSOC}(err(SOC)) = [U(SOC) - \omega_i(SOC)]^2, \quad err(SOC^{0\%}) = 0 \tag{3.45b}$$

$$\omega_i(SOC) = \frac{U(\lambda_i) - U(\lambda_{i-1})}{\lambda_i - \lambda_{i-1}}(SOC - \lambda_{i-1}) + U(\lambda_{i-1}) \text{ for } \lambda_{i-1} \leq SOC \leq \lambda_i \tag{3.45c}$$

$$\lambda_0 = SOC^{0\%}, \quad \lambda_N = SOC^{100\%} \tag{3.45d}$$

$$\lambda_i \geq \lambda_{i-1} + \epsilon, \quad i = 1, \ldots, N \tag{3.45e}$$

The continuity constraint implies that $\omega(\lambda_{i+1}) = \omega(\lambda_i)$, and can be written as:

$$\lambda_i = -\frac{U(\lambda_i) - U(\lambda_{i-1})}{\lambda_i - \lambda_{i-1}}\lambda_{i-1} + U(\lambda_{i-1}) \tag{3.46}$$

3.4.3 Optimizing joint-points for continuous piecewise linearization

The proposed method for optimizing the joint-points uses the genetic algorithm (GA), which is inherently stochastic in nature. The GA is theoretically proven to eventually attain global convergence, and its stochastic nature prevents any prediction or calculation of its rate of convergence. As a result, these routines can be computationally expensive in real-time calculations.

Since the continuous piecewise linearization of the OCP will be performed offline, the real-time calculation constraint does not apply. Therefore, the problem can be solved to global optimality by the GA, which guarantees that the resulting solution is globally optimal within an epsilon tolerance.

The experimental procedure for obtaining the OCP curves will be discussed in Section 3.6. As shown in Figure 3.4, the anode OCP is nearly constant. The OCP of the cathode is an order of magnitude higher than that of the anode; therefore, the knot locations are optimized for the cathode. The results of the optimization problem described in equation (3.44) are shown in equation (3.47). Since the nonlinear relation between the OCP and the cell SOC is chemistry dependent. The optimized knot locations will differ according to the lithium ion chemistry under consideration. In this experiment, the optimized knot locations are at (6%, 23%, 49%, 78%) SOC_p. Round-off errors at lower SOC are avoided by choosing the first piecewise-linear region interval away from the steep portion of the cathode OCP curve.

$$\lambda = [0.06, 0.23, 0.49, 0.78, 1] \tag{3.47}$$

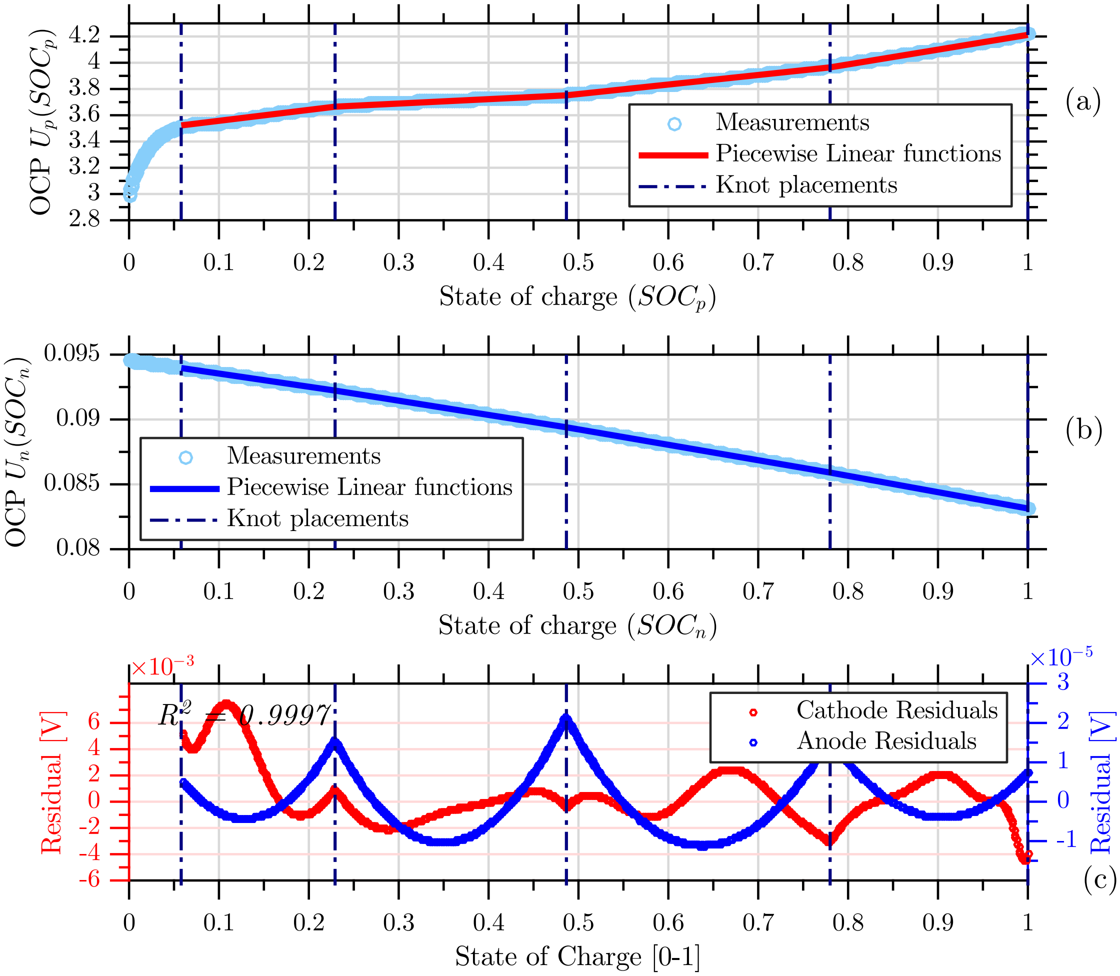

Figure 3.4: Comparison of the experimental OCP curves and the CPWL functions obtained by optimizing the joint-points. (a) Cathode, (b) Anode, (c) Residual plot for Cathode (red) and Anode (blue).

Figure 3.4 shows the optimized knot locations and compares between the measurement and the piecewise-linear functions. In both parts of the graphs, the x-axis represents the normalized concentration, and the y-axis represents the OCP [V] and residuals [V], in upper and lower figures, respectively. The residuals graph shows the accuracy of the piecewise-linear functions with respect to the nonlinear function; the coefficient of determination of the fitted functions is equal to 0.9997.

By substituting equation (3.47) in equation (3.43),

$$\omega(SOC_{n,p}) = \begin{cases} 0.82SOC_p - 0.05SOC_n + 3.42 & : 0.06 \leq SOC_p \leq 0.23 \\ 0.31SOC_p - 0.05SOC_n + 3.53 & : 0.23 \leq SOC_p \leq 0.49 \\ 0.69SOC_p - 0.03SOC_n + 3.34 & : 0.49 \leq SOC_p \leq 0.78 \\ 1.08SOC_p - 0.02SOC_n + 3.09 & : 0.78 \leq SOC_p \leq 1.00 \end{cases} \tag{3.48}$$

The CPWL-EAM terminal voltage can be calculated by substituting equations (3.21), (3.22), and (3.48) in equation (3.20):

$$V(t) = \omega(SOC_{n,p}) + \frac{RT}{\alpha_a F} \ln \frac{\xi_p + \sqrt{\xi_p^2 + 1}}{\xi_n + \sqrt{\xi_n^2 + 1}} - IK_{res} \tag{3.49}$$

3.4.4 Comparison with existing models

A well-determined model for the nonlinear relation between the OCP and the cell SOC is indispensable for the model performance. The proposed method is compared against six different models summarized by Weng et al. in [81] and listed in Table 3.2. The OCP data shown in figure 3.4-a is used to fit the models presented in Table 3.2 using the Matlab curve fitting toolbox.

The RMS error and CPU time for the models' fitting results are shown in Table 3.2. The proposed continuous piecewise-linear model has the lowest CPU run time and the third highest accuracy when compared to the other models.

It should be noted that none of the other six models in Table 3.2 reduces the model to a linear form. The benefit of the piecewise linearization is the ability to incorporate optimal SOC estimation techniques such as Kalman Filter. Linear estimation strategies are simpler, computationally more efficient, more robust and more accurate for linear or piecewise linear systems compared to non-linear estimation techniques.

#	Model (x = SOC, y = OCP(SOC))	RMSE (mV)	CPU time (ms)	Ref
1	$y = k_0 - \frac{k_1}{x} - k_2 x + k_3 ln(x) + k_4 ln(1-x)$	5.68	0.384	[7]
2	$y = k_0 + k_1(1 - e^{-\alpha_1 * x}) + k_2(1 - e^{\frac{-\alpha_2}{1-x}}) + k_3 x$	6.40	0.396	[82]
3	$y = k_0 + k_1 e^{-\alpha_1(1-x)} + \frac{k_2}{x}$	3.20	0.226	[83]
4	$y = k_0 + k_1 e^{-\alpha_1 x} + k_2 x + k_3 x^2 + k_4 x^3$	4.69	0.287	[12]
5	$y = k_0 + k_1 x + k_2 x^2 + k_3 x^3 + k_4 x^4 + k_5 x^5 + k_6 x^6$	1.23	0.606	[84]
6	$y = k_0 + k_1 \frac{1}{1+e^{\alpha_1(x-\beta_1)}} + k_2 \frac{1}{1+e^{\alpha_2(x-\beta_2)}} + k_3 \frac{1}{1+e^{\alpha_3(x-1)}} + k_4 \frac{1}{1+e^{\alpha_4(x)}} + k_5 x$	1.03	0.960	[81]
7	Continuous Piecewise Linear Model (CPWL), equation (3.48)	3.16	0.124	

Table 3.2: Comparison between different open circuit potential models.

3.5 Experimental setup

In this paper, parameterization and validation data sets have been gathered experimentally using a prismatic lithium-ion battery cell suitable for high-power applications like PHEVs, HEV, and EV. The battery positive electrode material is NMC-based, and the anode is graphite-based.

The tests are done on a Scienlab battery test bench. The voltage accuracy is ± 0.05% ($\simeq \pm$ 1mV) of the measured value, the current accuracy is ± 0.05% ($\simeq \pm$ 20mA) of the measured value. The sensors are integrated to the test bench. During testing, the cells are placed in a climate chamber with a continuously controlled ambient temperature of 25°C.

The cycler has 12 channels; four different current profiles were tested on 12 cells (one cell per channel). In order to account for any cell manufacturing variations, each test was conducted on a cluster of three cells of the same type and under the same conditions. The cluster output was averaged to obtain the measurement variables. The cell voltages, currents, and temperature are sampled every 100ms. The measured variables are used as input data for the presented algorithm in the MATLAB/Simulink environment.

3.6 Parameter identification procedure

This section presents the procedure for identifying the model parameters. The reduced-order, electrode-averaged model requires fewer parameters than the full-order model; however the number of parameters is still relatively high, if all of the parameters values are considered as unknowns. These parameters represent geometrical, physical, or chemical properties. In order to decrease the number of parameters to be identified, the parameterization process will be divided into two steps.

In step one, the battery cell is operated within $[C/30 \text{ to } C/50]$ range of operation using experimental inputs so as to limit the number of parameters which impact the output voltage. The parameters are identified using experimental data. In step two, the battery cell is excited with a signal that is rich in the frequency range necessary to identify the rest of the parameters. This approach has the advantage of providing a trade-off between extensive experimental characterization techniques and purely identifying all of the parameters using nonlinear techniques. Table 3.3 summarizes the model constants or formula-based parameters [25].

Symbol	Value		
	Anode	Separator	Cathode
α_a, α_c	0.5	-	0.5
t_0^+	0.363	0.363	0.363
σ	1	-	0.1
σ^{eff}	$\sigma^{eff} = \varepsilon_s^{n,p}\sigma$	-	$\sigma^{eff} = \varepsilon_s^{n,p}\sigma$
$a_s^{n,p}$	$a_s^n = \frac{3\varepsilon_s^{n,p}}{R_s}$	-	$a_s^p = \frac{3\varepsilon_s^{n,p}}{R_s}$
D_e^{eff}	$D_e^{eff} = \varepsilon_e^{1.5} D_e$		
κ	$\kappa = 0.0158 c_e e^{\left(0.85 c_e^{1.4}\right)}$		
κ^{eff}	$\kappa^{eff} = \varepsilon_s^{n,p}\kappa$		
κ_D^{eff}	$\kappa_D^{eff} = \frac{2RT\kappa^{eff}}{F}(t_0^+ - 1)$		

Table 3.3: Model parameters - constant parameters and formula-based parameters.

The solid concentrations inside the electrodes and the correlation function between the electrodes' solid concentrations and their OCP are obtained from OCV data. This step relies mostly on utilizing half-cell OCV curves. Next, the rest of parameters are optimized using the GA. Lastly, the model is compared to experimental results.

3.6.1 Identification of capacity-related parameters

This step identifies the solid concentrations inside the electrodes and is used to obtain the correlation function between the electrodes' solid concentrations and their OCP. This step makes SOC-dependent and rate-dependent parameters easier to identify by sweeping through the full range of battery states of charge at different charge/discharge rates. The correlation between the negative electrode active material solid concentration and its open circuit potential has been measured in the laboratory.

Anode OCP $U_n(\theta_n)$ measurements were made using a composite graphite film ($\simeq$ 140 microns thickness; MTI Corporation) mounted on copper foil in a half-cell versus a solid lithium metal electrode with a standard, commercial electrolyte consisting of 1.0 M LiPF6 in EC/DEC, 1:1 (v/v) (Novolyte Corporation). A coin cell geometry was used, and the cells were assembled under argon atmosphere in a glove box. They were then cycled at C/50 on a BT2000 multi-channel cycler (Arbin Instruments), and the 3rd cycle was used to construct the OCP curve, to allow for SEI formation (Coulombic efficiency was in excess of 99% by this cycle). Both the charge and discharge curves exhibit the characteristic plateaus and stoichiometric phase transitions associated with Li intercalation into graphite, and the inserted and extracted specific capacity is approaching the theoretical specific capacity for graphite of 372 mAh/g as shown in Figure 3.5-a.

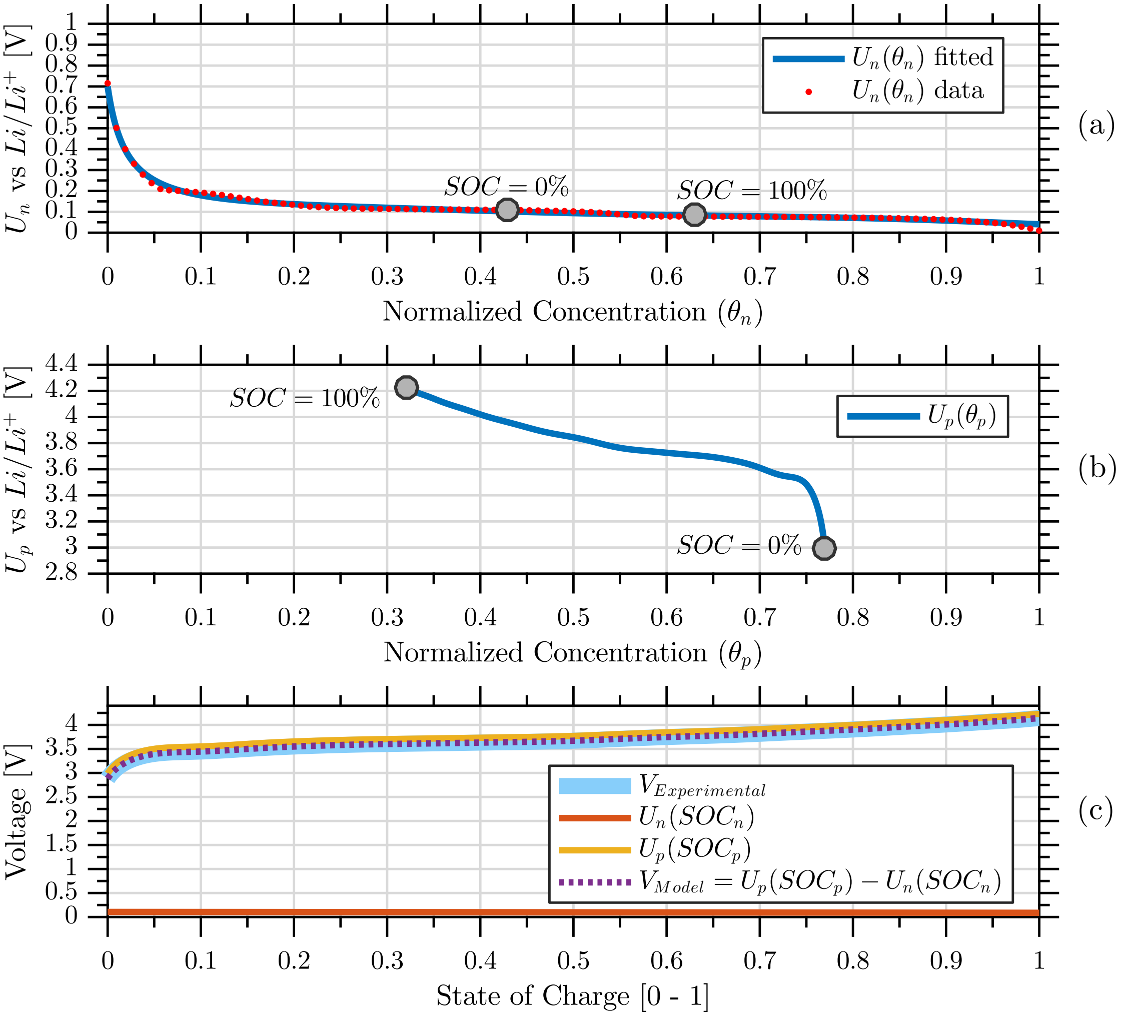

Figure 3.5: Open circuit potential versus normalized concentration for (a) positive electrode, (b) negative electrode, and (c) open circuit potentials, experimental versus model.

The Cathode OCP $U_p(\theta_p)$ is calculated by adding the measured battery open circuit voltage V_{ocv} to the Anode OCP $U_n(\theta_n)$.

$$U_p(\theta_p) = V_{ocv} + U_n(\theta_n) \tag{3.50}$$

The obtained Cathode OCP $U_p(\theta_p)$ is shown in Figure 3.5-b. The open-circuit potential for the positive electrode $U_p(\theta_p)$ and the negative electrode $U_n(\theta_n)$, along with the

OCV (V_{ocv}) relationship are shown in Figure 3.5-c. The capacity-related parameters with their lower bounds (LB) and upper bounds(UB) are summarized in Table 3.4

Symbol	Unit	Anode		Cathode	
		LB	UB	LB	UB
$c_{s,max}^{n,p}$	mol cm^{-3}	$1e^{-4}$	1	$1e^{-4}$	1
$\theta_{0\%}$	-	0	1	0	1
$\theta_{100\%}$	-	0	1	0	1

Table 3.4: Capacity-related parameters lower and upper bounds.

3.6.2 Identification of diffusion-related parameters

The objective of this step is to identify the parameters associated with the battery transient response in each CPWL region. A parameterization cycle that contains charge-sustaining and charge-depleting phases is chosen, as shown in Figure 3.6-a. The cycle frequency content makes it easier to identify the cell parameters, as illustrated in Figure 3.6-b. The test starts with a fully charged battery and then a current profile is applied to discharge the battery until the SOC specified in equation (3.47) is reached. Then, the cell is left to rest at this SOC to allow for full cell relaxation. Finally, the cycle is repeated in each CPWL region until the battery is fully discharged.

The diffusion-related parameters, with their lower and upper bounds, are summarized in Table 3.5.

Symbol	Unit	Anode		Cathode	
		LB	UB	LB	UB
$\varepsilon_s^{n,p}$	$-$	$1e^{-4}$	1	$1e^{-4}$	1
D_e	$cm^2\ s^{-1}$	$1e^{-14}$	1	$1e^{-14}$	1
$R_s^{n,p}$	cm	$\frac{\delta_n}{20}$	δ_n	$\frac{\delta_p}{20}$	δ_p
$\bar{c}_e$	mol cm^{-3}	$[1e^{-4} - 1e^4]$			
R_f	Ωcm^2	$[1e^{-4} - 1e^4]$			
A	cm^2	$[7e^3 - 9e^3]$			

Table 3.5: Diffusion-related parameters lower and upper bounds.

After the identification procedure by the GA, the model shows an accurate voltage prediction, with an approximate Root Mean Square Error (RMSE) of 0.022 [V] and Mean Absolute Error (MAE) of 0.020 [V]. The identified parameter set is listed in Table **3.6**.

Symbol	Unit	Identified values	
		Anode	Cathode
$c_{s,max}^{n,p}$	mol cm^{-3}	0.072	0.080
$\theta_{0\%}$	–	0.428	0.824
$\theta_{100\%}$	–	0.774	0.483
$\varepsilon_s^{n,p}$	–	0.958	0.950
$R_s^{n,p}$	cm	0.00026	0.000475
A	cm^2	8833.9	
$\bar{c}_e$	mol cm^{-3}	[3.13 , 3.11 , 3.11 , 2.07]× 1e2	
R_f	Ωcm^2	[1.73 , 1.93 , 1.97 , 2.81]× 1e-7	
D_e^n	$cm^2\ s^{-1}$	[7.45 , 7.45 , 7.45 , 7.45]× 1e-10	
D_e^p	$cm^2\ s^{-1}$	[8.43 , 7.38 , 5.21 , 4.87]× 1e-10	

Table 3.6: Identified model parameters.

Under the parameterization cycle, the model shows an accurate voltage prediction during both the steady and transient phases, as shown in Figure 3.6-c and 3.6-d. The gray-solid line represents the experimental battery voltage, while the blue-solid and green-dotted lines represent the EAM and CPWL-EAM responses, respectively. The lower part of the figure shows the error between the measured voltage and the calculated voltage of the models. Since the error is determined by subtracting the measured voltage from the estimated voltage; the positive error implies under-calculation, while the negative error indicates over-calculation.

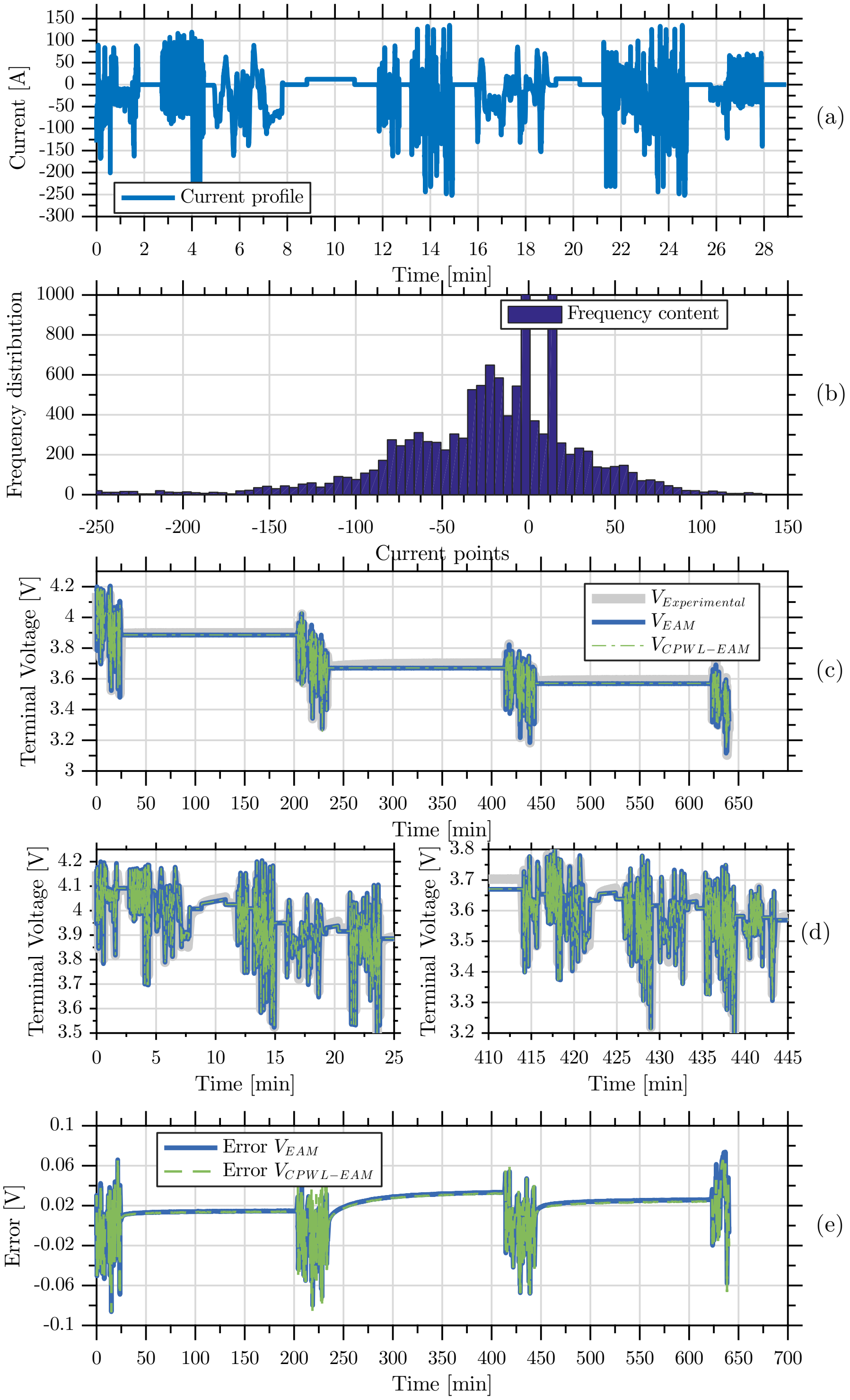

Figure 3.6: Parameterization Cycle - (a) Current profile, (b)frequency distribution of the current profile, (c,d) voltage response, and (e) voltage error.

3.7 Model validation under different driving profiles

In this section, the model performance is compared with experimental data to demonstrate the effectiveness of the preceding methodology. The validation cycles in this section are different from those utilized for the purpose of identification. The two validation cycles used are the US Federal Test Procedure (FTP-72) cycle, also called the Urban Dynamometer Driving Schedule (UDDS), and the Worldwide Harmonized Light Vehicles Test Procedure (WLTP). The two error quantitative matrices are the RMSE and MAE.

3.7.1 Results under FTP72

The first set of validation data is the FTP-72 cycle as shown in Figure 3.7-a. Under the FTP-72 cycle, the calculated voltages of the EAM and the CPWL-EAM are compared against the measured voltage in Figure 3.7-b and 3.7-c, with the voltage error shown in Figure 3.7-d. The gray-solid line represents the experimental battery voltage, while the blue-solid and green-dotted lines represent the EAM and CPWL-EAM responses, respectively. The RMSE between the modeled voltage and the measured voltage over five consecutive cycles with 10 minutes rest between cycles is 0.019 V, and the MAE is 0.014 V.

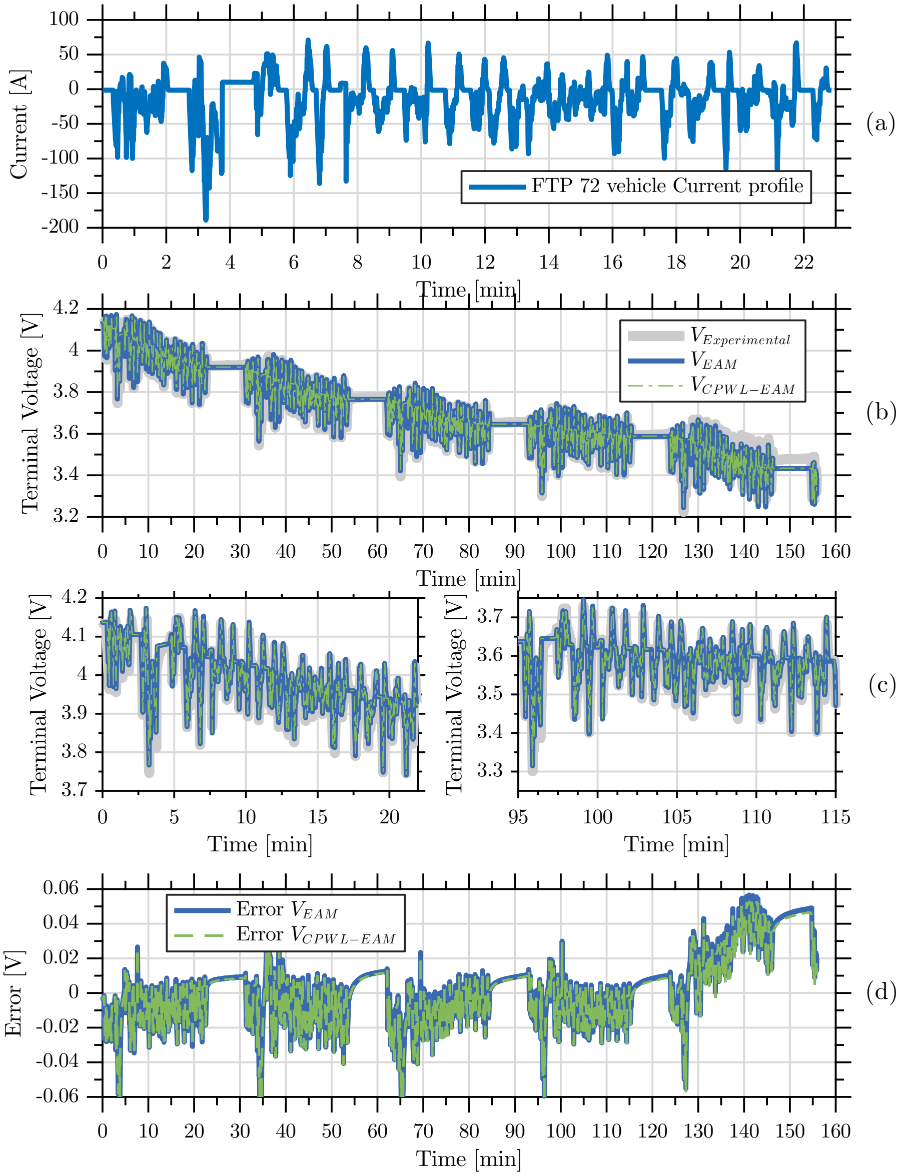

Figure 3.7: Validation Cycle (FTP72) - (a) Current profile, (b,c) voltage response, and (d) voltage error.

3.7.2 Results under WLTP-Case 3

The second set of validation data is Case 3 of the WLTP. Case 3 stands for high-power vehicles with Power to Weight ratio (PWr) > 34. This driving cycle consists of four parts Low, Medium, High, and Extra High-speed as shown in Figure 3.8-a.

Under the WLTP cycle, the calculated voltages of the EAM and the CPWL-EAM are compared against measured voltage in Figure 3.8-b and 3.8-c with the voltage error shown in Figure 3.8-d. Here again, The gray-solid line represents the experimental battery voltage, while the blue-solid and green-dotted lines represent the EAM and CPWL-EAM responses, respectively. The RMSE between the modeled voltage and the measured voltage over four consecutive cycles with 10 minutes rest between cycles is 0.018 V, and the MAE is 0.015 V.

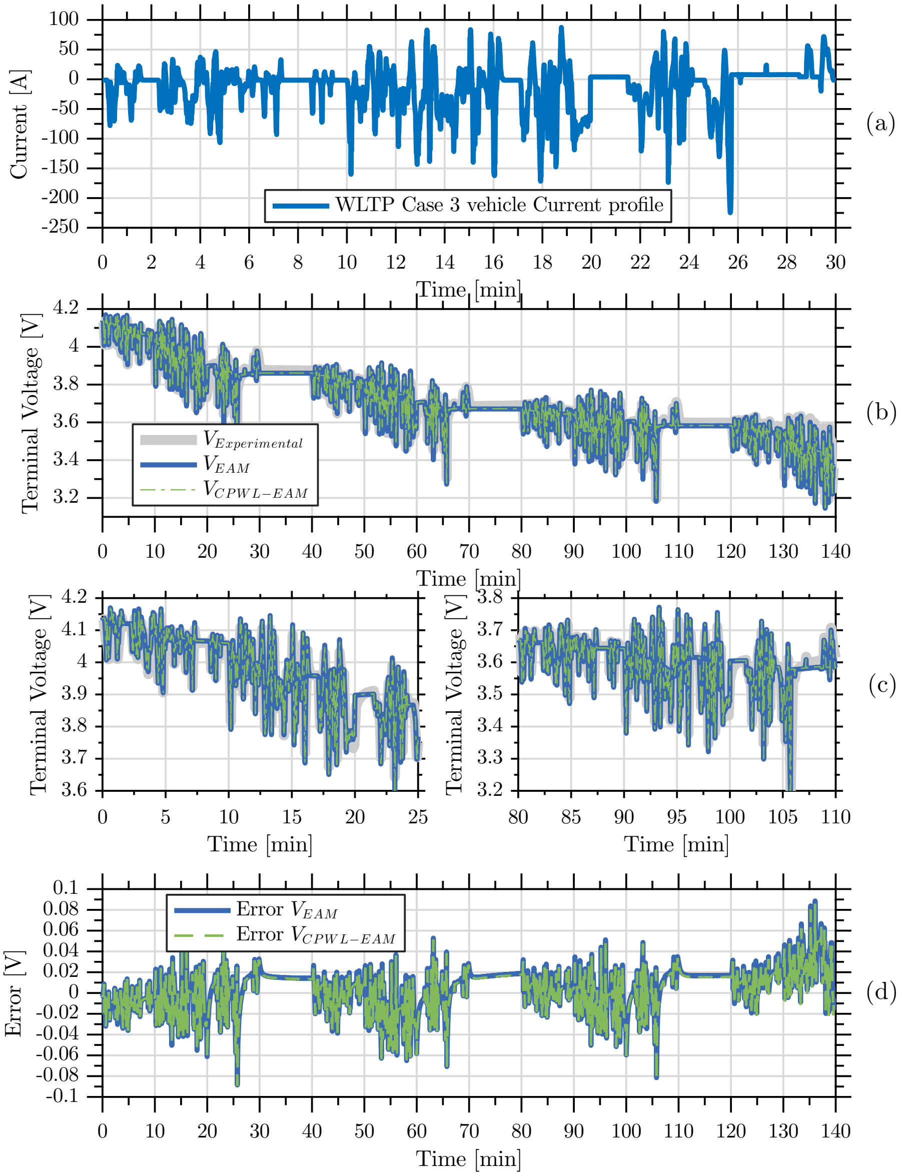

Figure 3.8: Validation Cycle (WLTP- case 3) - (a) Current profile, (b,c) voltage response, and (d) voltage error.

3.8 Results and comparison

By comparing the voltage error under the various different discharge currents in Figure 3.6-c, 3.7-b, and 3.8-b, it is clear that the CPWL-EAM exhibits accurate voltage prediction during the steady and transient phases of cycling. The proposed model was able to maintain the voltage prediction accuracy, while decreasing the mean CPU time as shown in Table 3.7. The reduction in the CPU run-time by around 20% (from 2.12 sec. to 1.64 sec), due to the reformulation of the nonlinear OCP equation as a four-point lookup table, where the voltage values falling between the points are calculated using onboard linear interpolation. The CPU times presented in this publication were run on a 2.30 GHz Intel processor with 16 GB RAM.

a	EAM		CPWL-EAM	
	RSME	MAE	RSME	MAE
Parameterization cycle	0.023	0.021	0.022	0.020
Validation cycle - FTP72	0.020	0.015	0.019	0.014
Validation cycle - WLTP	0.019	0.015	0.018	0.015
Mean	0.020	0.017	0.020	0.016

b	EAM	CPWL-EAM
	CPU time (sec)	CPU time (sec)
Parameterization cycle	4.23	3.82
Validation cycle - FTP72	1.11	1.02
Validation cycle - WLTP	1.01	0.09
Mean	2.12	1.64

Table 3.7: Model results for different cycles (a) RMSE and MAE [V], (b) Computation time [sec].

3.9 Conclusion

In conclusion, a continuous, piecewise- linear, electrode-average model is presented, which exhibits high accuracy and reduced CPU runtime compared with the reduced-order, electrode-average model (EAM). The proposed CPWL-EAM linearizes the univariate, nonlinear relation between the OCP and the cell SOC, while maintaining the continuity and smoothness of the OCP curve. The piecewise-linear regions were identified using a novel optimal knot-placement technique which uses GA to determine the optimal knot-locations, while maintaining the continuity constraints. The model is parametrized using a new technique that provides a trade-off between extensive experimental characterization techniques and purely identifying all parameters using nonlinear techniques. The accuracy of the CPWL-EAM is validated through comparison with experimental data and the EAM under the real-time driving profiles FTP-72 and WLTP. The calculated RMSE and MAE are 0.020 V and 0.016 V respectively. Since the CPWL-EAM model shows accurate voltage prediction, while reducing the running time by 20%, the proposed model can be easily implemented onboard in a real-time BMS. Future work will focus on incorporating optimal state of charge estimation techniques (e.g. Kalman Filter), along with model parameterization and validation under different temperature and aging conditions through changing of the knot-location.

Nomenclature

Symbol	**Description**	**Unit**
Acronyms		
$\mathbf{A}$	State matrix in linear state model state equation	$-$
$\mathbf{B}$	Input matrix in linear state model state equation	$-$
$\mathbf{C}$	State matrix in linear state model output equation	$-$
$\mathbf{D}$	Input matrix in linear state model output equation	$-$
$R_s^{n,p}$	Solid active material particle radius	cm
R_f	Film resistance on the electrodes surface	Ωcm^2
A	Electrode plate Area	cm^2
t_0^+	Transference number of lithium ion	$-$
c	Concentration of lithium ions	mol cm^{-3}
D	Diffusion coefficient of lithium species	$cm^2 s^{-1}$
q	Discretization step	$-$
R	Universal gas constant (R = 8.3143)	J $mol^{-1} K^{-1}$
F	Farady's Constant (F = 96,487)	C mol^{-1}
T	Absolute Temperature	K
a_s	Active surface area per electrode unit volume	$cm^2 cm^{-3}$
I	Applied current	A
r	Radial coordinate	cm
t	Time	s
x	Cartesian coordinate	s
j^{li}	Butler-Volmer current density	A cm^{-3}
R^+, R^-	Internal Resistance of the cell	A cm^{-3}
Greek Symbols		
ε_s	Active material volume fraction	$-$
ε_e	Electrolyte phase volume fraction	$-$
σ	Conductivity of solid active material	$\Omega^{-1} cm^{-1}$
κ	Electrolyte phase ionic conductivity	$\Omega^{-1} cm^{-1}$

κ_D	Electrolyte phase diffusion conductivity	$\Omega^{-1}cm^{-1}$
θ	Reference stoichiometry	$-$
α_a, α_c	Anodic and cathodic charge transfer coefficients	$-$
α_1, α_2	The poles of the low pass filter	$-$
η	Surface overpotential of an electrode reaction	V
ϕ	Volume averaged electrical potential	V
δ	Thickness	cm

Superscripts

eff	Effective	$-$
p	Cathode	$-$
n	Anode	$-$
sep	Separator	$-$

Subscripts

e	Electrolyte phase	$-$
s	Solid phase	$-$

Chapter 4

Combined electrochemical, heat generation, and thermal model for large prismatic lithium-ion batteries in real-time applications [1]

4.1 Abstract

Real-time prediction of the battery's core temperature and terminal voltage is very crucial for an accurate battery management system. In this paper, a combined electrochemical, heat generation, and thermal model is developed for large prismatic cells. The proposed model consists of three sub-models, an electrochemical model,

---

[1] Mohammed Farag, Haitham Sweity, Matthias Fleckenstein, Saeid Habibi
Combined electrochemical, heat generation, and thermal model for large prismatic lithium-ion batteries in real-time applications
Submitted and under revision by the Journal of Power Sources

heat generation model, and thermal model which are coupled together in an iterative fashion through physicochemical temperature dependent parameters. The proposed parameterization cycles identify the sub-models' parameters separately by exciting the battery under isothermal and non-isothermal operating conditions. The proposed combined model structure shows accurate terminal voltage and core temperature prediction at various operating conditions while maintaining a simple mathematical structure, making it ideal for real-time BMS applications. Finally, the model is validated against both isothermal and non-isothermal drive cycles, covering a broad range of C-rates, and temperature ranges [-25°C to 45°C].

4.2 Introduction

In the past decade, lithium-ion batteries have gradually gained acceptance in the automotive sector as electric energy storage due to their high specific energy, low self-discharge rate, and non-memory effect. In order to efficiently integrate the lithium-ion batteries in electric vehicles (EV), different cell sizes have been introduced. Depending on the method of packing, the cells can be shaped into a pouch, cylindrical, or prismatic form. Prismatic lithium-ion batteries have become one of the most attractive options for energy storage systems due to their optimal use of space and light weight. However, abnormal operating conditions such as over discharge, overcharge, or high operating temperature can accelerate their aging and degradation and may lead to thermal runaways in extreme cases. To fully benefit from a lithium-ion energy storage system and avoid its physical degradation, an accurate battery management system (BMS) is required. The BMS is responsible for the battery state of charge (SOC), state of health (SOH), state of power (SOP), and thermal management. It uses state estimation algorithms for monitoring, as well as operating the battery within a range that is considered as nominal in order to ensure safety and performance as well as preserving its projected useful life. One of the main requirements for a successful BMS implementation is the development of a high fidelity battery model that includes thermal and aging dependent parameters. The battery model needs to be dynamically significant while being computationally efficient, robust, and accurate. Of particular interest is the prediction of the terminal voltage which is affected by the cell's core temperature. As such, an accurate thermal model is needed to predict the core temperature and estimate its dynamics. The inclusion of a thermal model within the overall battery model is necessary as it enables the BMS to operate the battery safely and preserve its performance effectively.

Battery models are broadly classified under three categories: equivalent circuit [11, 12, 13, 14], behavioral (or black-box) [7, 8, 9, 10], and electrochemical (physics-based) models [28, 31, 32]. The equivalent circuit models are widely used in BMS due to their acceptable accuracy, complexity, and fidelity. Most of the electrochemical modeling approaches found in the literature are based on the electrochemical pseudo-two-dimensional (P2D) model further developed following the Doyle-Fuller-Newman model [26, 27]. The physics-based P2D model is very accurate; however, it is excessively computationally complex, thereby burdening its real-time implementation. Therefore, many model reduction methods have been proposed to reduce its complexity while maintaining its accuracy. The model reduction methods commonly used can be divided into two categories. One category focuses on reducing the computational complexity involved in solving the concentration of lithium in the solid particles of the electrodes by either simplifying the concentration profile or assuming it to be constant as presented by [15, 34, 36]. Another category focuses on reducing the electrochemical model as a whole, such as to avoid the solution of large sets of differential-algebraic equations (DAEs) of the Li^+ concentration distribution and the potential distribution of the electrolyte phase. Examples of the latter can be found in [16, 37, 39].

In order to investigate the dynamic behavior of the cell, two main approaches are discussed in the literature: (i) electrochemical impedance spectroscopy (EIS) and (ii) measurement of a voltage response using controlled input currents and then applying optimization techniques to determine the model parameters. The general principle of the EIS method is to apply an input signal either current (galvanostatic) or voltage (potentiostatic) and then measure the characteristic response of the cell which depends on the cell impedance. In the scope of this publication, the model is parameterized and validated using the second approach. The battery under test was subjected to charging, charge-sustaining and charge-depleting phases at six different temperature in order to determine the temperature dependency of the parameters. The genetic algorithm (GA) was then used to optimize the model parameters.

In addition, various strategies have been proposed in the literature for modeling the temperature profile inside a cell during its operation. These include coupled partial differential equations (PDE) models, linear parameter-varying state-space models, three-dimensional Finite Element Analysis (FEA) models and relatively simple lumped capacitance zero-dimensional thermal models. Smyshlyaev et al. [51] proposed an analytic solution for solving the thermal model PDEs. Whereas, Hu et al. [52] reduced the PDEs computational complexity by fitting a more complicated computational fluid dynamics (CFD) model to a linear parameter-varying state-space model. Guo et al. [53] presented a three-dimensional FEA thermal model, while Baba et al. [54] developed a full 3D thermal model that takes into account local heat generation and the spatial dependencies to obtain a full 3D temperature distribution of the cell. The FEA thermal models are very accurate; however, they require excessive computational power and specific material properties, which limit their real-time implementation especially when fluid dynamics are considered in the cooling process. Damay et al. [49] developed a lumped capacitance, zero-dimensional thermal model. The model included one heat capacitor coupled with different modes of heat transfer throughout the cell to represent the thermal behavior of a prismatic cell. Similarly, Forgez et al. [50] employed the same technique for cylindrical cells using two heat capacitors. Further to the above, the lumped capacitance modeling approach will also be considered in this work due to its low computational complexity and acceptable accuracy. An accurate set of parameters is required for obtaining a high-fidelity thermal model. The thermal parameters are either determined analytically or experimentally. Lin et al. [55] used detailed information about the material and geometry of the cell for analytically determining the parameters. Perez et al. [24] used the least squares optimization algorithms to fit the model to the experimental data. Lin et al. [56] proposed an online estimation algorithm. Sastry et al. [85] developed a surrogate-based modeling and dimension reduction techniques to assess the role of design variables on multiple competing objectives for a wide range of engineering problems [86, 87].

In this publication, an experimental method involving optimization will be used instead of the analytical methods as they suffer from a high level of uncertainty.

This paper proposes three unique contributions for improving battery modeling.

The first contribution is a combined electrochemical, heat generation, and thermal model capable of accurately predicting the cell's terminal voltage and core temperature. The second contribution is an accurate yet computationally simple four-node thermal model (4NTM). The 4NTM helps in estimating the battery's core temperature leading to an increase in the terminal voltage accuracy within a broad range of temperatures [-25°C to 40°C]. The four-node structure constitutes a reduced order form that renders the model suitable for real-time applications. The third contribution is a model parameterization scheme that allows identification of each sub-model parameters separately.

Paper structure In section 4.3, the combined electrochemical, heat generation and thermal model is illustrated. Section 4.4, 4.5 and 4.6 presents the reduced-order electrochemical model (ROM), the heat generation model, and the thermal model respectively. In section 4.7, the parameter identification procedure and the experimental setup are explained. The ROM, 4NTM, and the combined ECHTM are then validated using battery voltage, current, and temperature measurements against different driving cycles. Finally, the conclusion, results, and future work are presented.

4.3 The combined model

This sections will present the main contribution of this paper, the formulation of a combined electrochemical, heat generation, and thermal model (ECHTM) that allows the BMS to effectively operate the battery in safe conditions and improve its terminal voltage, SOC, and SOH estimation accuracy. Figure 4.1 shows a schematic representation of the combined ECHTM and its sub-models. The combined ECHTM is capable of estimating the cell's SOC, terminal voltage, and core temperature and it is divided into three different sub-models. First, the electrochemical model estimates the cells' terminal voltage V_t, SOC, open circuit potential $U_{p,n}$, and Li-ion concentration gradients $C_s^{n,p}$ as a function of the cell's core temperature T_c using physicochemical temperature dependent parameters. The cell's core temperature is calculated using a specific thermal model and fed back to the electrochemical model as an input. The heat losses are the most difficult elements to model due to the nonlinear nature of the heat sources. Thus, a specific model is developed for heat generation Q_{gen}, which computes reversible, irreversible, and heat of mixing losses, as a function of the measured terminal voltage, the measured current, the modeled $SOC_{p,n}$, the modeled $U_{p,n}$, and the concentration gradients $C_s^{n,p}$ determined by the electrochemical model. Finally, the 4NTM model evaluates the temperatures of the core T_c, bottom T_b, terminal T_t, and housing T_h as a function of the heat generation rate, cooler temperature T_k, cell's geometry and boundary conditions. The experimental results shown in section 4.8 and 4.9, indicates a relatively small difference between the housing and the core temperature of 2°C. Hence, only the core temperature information is then fed back to update the electrochemical model. This iterative procedure is repeated at every time step to model the cell in real time continuously.

In Figure 4.1 the blue arrows represent inputs, the black arrows represent internal variables, and the red arrows represent outputs. The colored-doted blocks represent software functions. The combined ECHTM inputs are data provided by the vehicle sensors, and the outputs are processed data transferred to the main BMS.

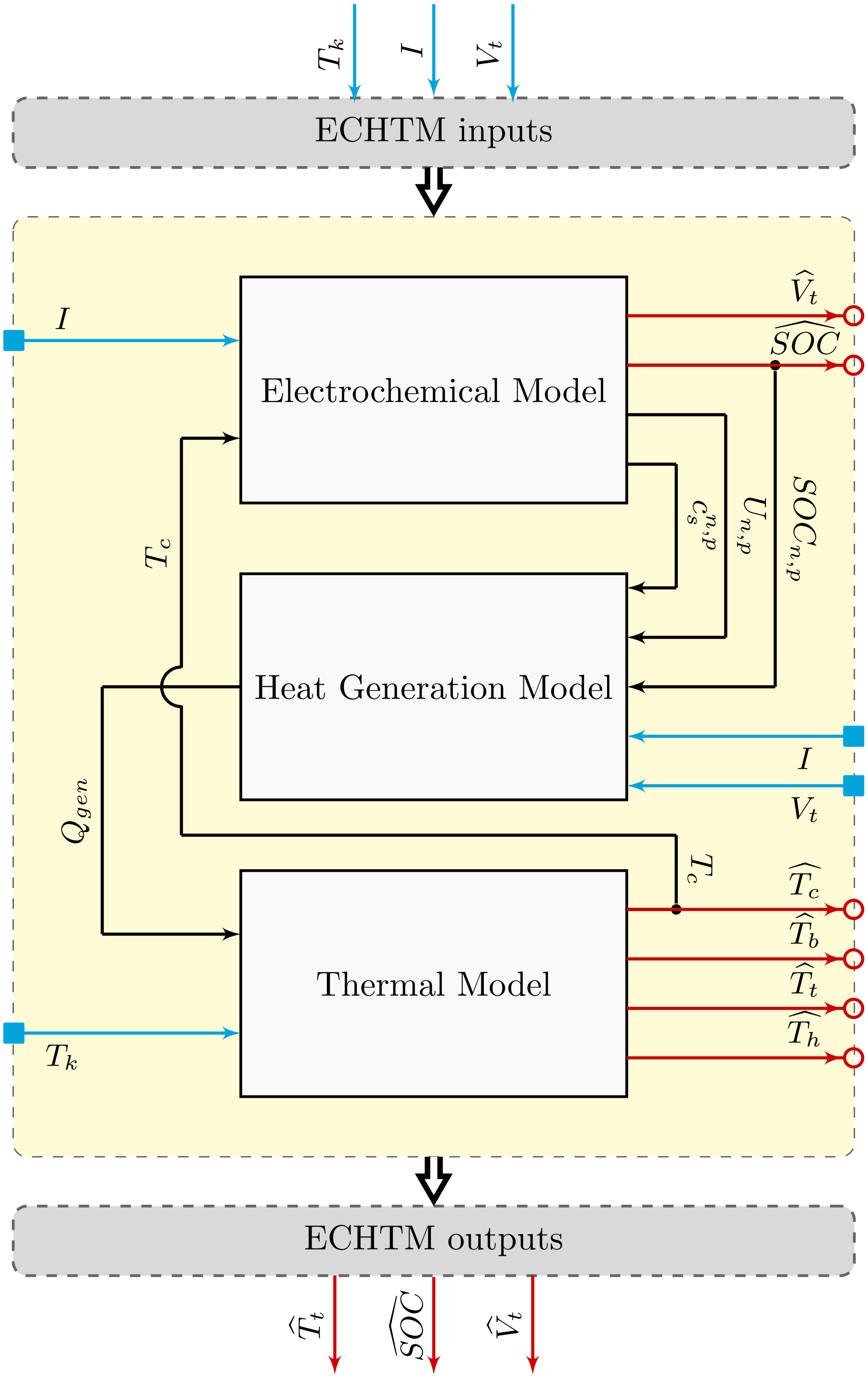

Figure 4.1: Diagram of the combined electrochemical, heat generation and thermal model (ECHTM) modeling approach.

In this section, the general formulation of the combined ECHTM is presented. In the following sections, the three sub-models are discussed in details.

4.4 Electrochemical battery model

4.4.1 Lithium-ion batteries principles of operation

Figure 4.2 shows the basic setup of a battery cell. It consists of four main parts: the positive electrode (cathode), the separator, the electrolyte, and the negative electrode (anode). The battery is connected to an external load using current collector plates. The anode is usually made up of a mixture of carbon (e.g. Li_xC_6), the cathode is typically made of metal oxides (ex. $LiCoO_2$ or $LiMn_2O_4$), while the electrolyte can be made of a salt-containing solvent mixture, polymer, or solid materials (e.g. $LiPF_6$).

Under the presence of a load current, reduction-oxidation reaction occurs. Oxidation reaction takes place at the anode where the trapped lithium particles start to deintercalate or diffuse toward the electrolyte-solid interface splitting lithium into ions and electrons. Lithium ions transfer through the solution due to the potential difference while the electrons move through the current collector because the electrolyte solution serves as a barrier to electrons. Reduction reaction takes place at the cathode where the traveling lithium ions from the anode start to intercalate and react with the electrons coming from the positive collector. An example of the electrochemical reactions are as follows:

$$Li_xC_6 \xrightleftharpoons[charge]{discharge} Li_0C_6 + xLi^+ + xe^- \tag{4.1}$$

$$Li_{(y-x)}Mn_2O_4 + xLi^+ + xe^- \underset{charge}{\overset{discharge}{\rightleftharpoons}} Li_yMn_2O_4 \tag{4.2}$$

The process of lithium ion insertion into the electrode happens without a change in the electrode crystal structure "intercalation" mechanism. The whole phenomenon of intercalation and deintercalation is reversible as lithium ions pass back and forth between the electrodes during charging and discharging. In theory, this phenomenon could go on infinitely. Unfortunately, due to cell material degradation and other irreversible chemical reactions, the cell capacity and power degrade with the number of cycles and usage.

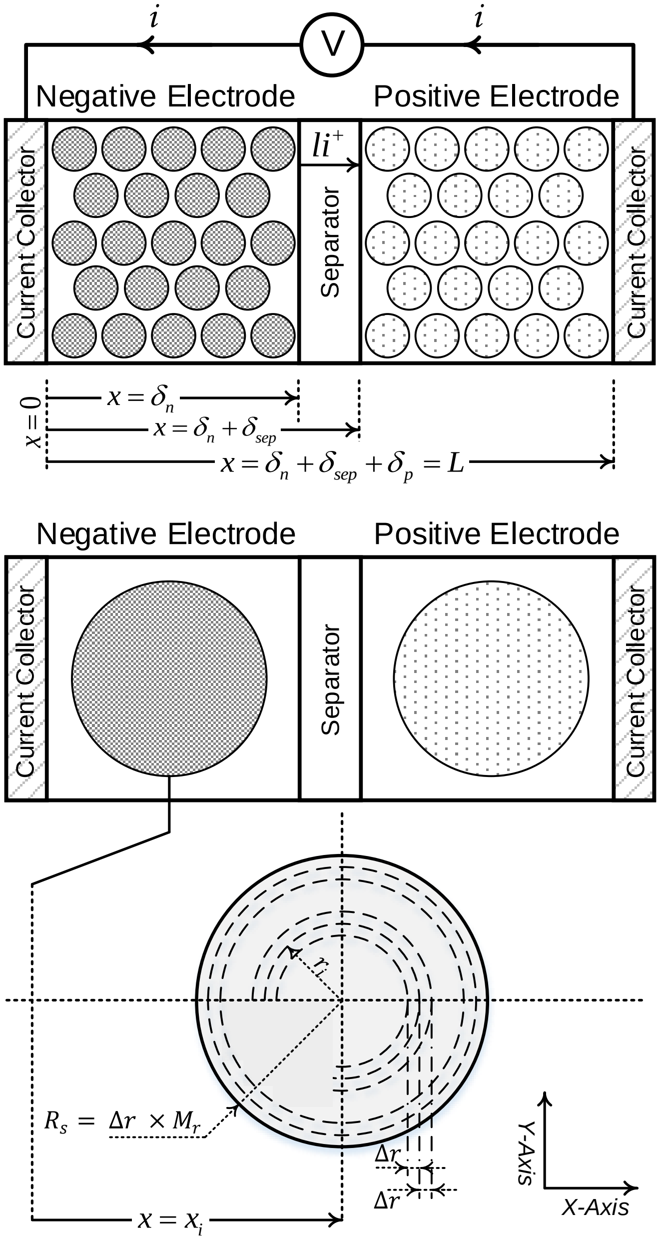

Figure 4.2: Schematic representation of the Li-ion battery operation principles and the single particle model simplification.

4.4.2 Model mathematical formulation

Relationship between concentrations and currents

The mathematical equations governing the charge and mass conservation in the solid and electrolyte phases is discussed in details in [1] and summarized in Table 4.1.

Conservation equations	Boundary conditions	Initial conditions
Mass transport in the solid phase		
$\frac{\partial c_s^{n,p}(x,r,t)}{\partial t} = \frac{D_s}{r^2}\frac{\partial}{\partial r}\left[r^2\frac{\partial c_s^{n,p}(x,r,t)}{\partial r}\right]$ (4.3)	$\left.\frac{\partial c_s^{n,p}}{\partial r}\right\vert_{r=0} = 0,$ $\left.\frac{\partial c_s^{n,p}}{\partial r}\right\vert_{r=R_s^{n,p}} = \frac{-j^{li}}{D_s a_s F}$ (4.4)	$c_s^{n,p}(x,r,t_0) = c_{s_0}^{n,p}(x,r)$ (4.5)
Mass transport in the electrolyte		
$\frac{\partial \varepsilon_e c_e(x,t)}{\partial t} = D_e^{eff}\frac{\partial^2 c_e(x,t)}{\partial x^2} + \frac{1-t_0^+}{F}j^{li}$ (4.6)	$\left.\frac{\partial c_e^n}{\partial x}\right\vert_{x=0} = 0,\ \left.\frac{\partial c_e^p}{\partial x}\right\vert_{x=L} = 0$ (4.7)	$c_e(x,t_0) = c_{e_0}(x)$ (4.8)
Potential in the solid electrodes		
$\sigma^{eff}\frac{\partial^2}{\partial x^2}\phi_s(x,t) = j^{li}$ (4.9)	$\left.\frac{\partial}{\partial x}\phi_s(x,t)\right\vert_{x=0,L} = \frac{-I}{A\sigma^{eff}}$ $\left.\frac{\partial}{\partial x}\phi_s(x,t)\right\vert_{x=\delta_n,\delta_n+\delta_{sep}} = 0$ (4.10)	$\phi_s(x,t_0) = \phi_{s,0}(x)$ (4.11)
Potential in the electrolyte		
$\kappa^{eff}\frac{\partial^2}{\partial x^2}\phi_e(x,t) + \kappa_D^{eff}\frac{\partial^2}{\partial x^2}\ln c_e = -j^{li}$ (4.12)	$\left.\frac{\partial}{\partial x}\phi_e(x,t)\right\vert_{x=0,L} = 0$ (4.13)	$\phi_e(x,t_0) = \phi_{e,0}(x)$ (4.14)

Table 4.1: Set of PDEs equations describing the full-order electrochemical model and its boundary and initial conditions.

Butler-Volmer kinetics equations

The Butler-Volmer current density equation governs the volumetric rate of the chemical reaction. This equation links the four conservation equations (4.3), (4.6), (4.9), (4.12) and is described as [1]:

$$j^{li} = a_s j_0 \left[\exp\left(\frac{\alpha_a F}{RT} \eta \right) - \exp\left(-\frac{\alpha_c F}{RT} \eta \right) \right] \tag{4.15}$$

where the overpotential η is defined as:

$$\eta = \phi_s - \phi_e - U(c_{se}) \tag{4.16}$$

and the coefficient j_0 is a function of the surface electrolyte concentration c_{se} and obtained as:

$$j_0 = (c_e)^{\alpha_a} \left(c_{s,\max}^{n,p} - c_{se}^{n,p} \right)^{\alpha_a} \left(c_{se}^{n,p} \right)^{\alpha_c} \tag{4.17}$$

Finally, the cell potential, V, across the cell terminals is determined as follows:

$$V = \phi_s(x = L) - \phi_s(x = 0) - R_f \frac{I}{A} \tag{4.18}$$

4.4.3 Model reduction

Due to the computational complexity of the Full Order Model (FOM) some assumptions and simplifications are considered in order to obtain a Reduced Order Model (ROM).

The simplification assumptions are as follows: (i) the lithium concentration in electrolyte c_e is assumed to be constant and uniform. (ii) the solid particle distribution along the electrode is neglected, this is due to the averaging procedure in the first assumption. (iii) the aging dependencies of the model parameters have been neglected. As a result of the assumptions mentioned above, a single particle from each electrode (anode and cathode) can describe the diffusion dynamics.

$$\frac{\partial c_s^{n,p}(r,t)}{\partial t} = \frac{D_s}{r^2}\frac{\partial}{\partial r}\left[r^2\frac{\partial c_s^{n,p}(r,t)}{\partial r}\right] \tag{4.19}$$

$$c_e(x,t) = \bar{c}_e \tag{4.20}$$

$$\sigma^{eff}\frac{\partial^2}{\partial x^2}\phi_s(x,t) = \bar{j}^{li}_{n,p} \tag{4.21}$$

$$\kappa^{eff}\frac{\partial^2}{\partial x^2}\phi_e(x,t) = -\bar{j}^{li}_{n,p} \tag{4.22}$$

$$\bar{j}^{li}_{n,p} = \frac{I}{A\delta_{n,p}} \tag{4.23}$$

The ROM is summarized in equation (4.19) to (4.23). The terminal voltage can be rewritten by substituting equation (4.16) in equation (4.18), as shown in [25]:

$$V(t) = [U_p(\theta_p) - U_n(\theta_n)] + \vartheta_\eta^{n,p}(\theta_{n,p}, I) - IK_{res} \tag{4.24}$$

Where K_{res} is described as follows:

$$K_{res} = \frac{R_f}{A} - (\bar{\phi}_e^p - \bar{\phi}_e^n) = \frac{1}{A}\left[R_f + \frac{(\delta_n + 2\delta_{sep} + \delta_p)}{2\kappa^{eff}}\right] \tag{4.25a}$$

$$where \quad \bar{\phi}_e^p - \bar{\phi}_e^n = -\frac{1}{2A\kappa^{eff}}(\delta_n + 2\delta_{sep} + \delta_p) \tag{4.25b}$$

The term $\vartheta_\eta^{n,p}(\theta_{n,p}, I)$ in equation (4.24) is the difference between the cathode and anode overpotentials, and can be calculated by substituting equation (4.23) in (4.15),

$a_s^{n,p} = 3\varepsilon_s^{n,p}/R_s^{n,p}$, and $\alpha_a = \alpha_c = 0.5$ from Table 4.3, as shown below:

$$\vartheta_\eta^{n,p}(\theta_{p,n}, I) = \bar{\eta}_p - \bar{\eta}_n = \frac{RT}{\alpha_a F} \ln \frac{\xi_p + \sqrt{\xi_p^2 + 1}}{\xi_n + \sqrt{\xi_n^2 + 1}} \tag{4.26a}$$

$$where \quad \xi_{n,p} = \Omega^{n,p} \frac{I}{\left(c_{s,\max}^{n,p} c_{se}^{n,p} - c_{se}^{n,p^2}\right)^{0.5}} \tag{4.26b}$$

$$and \quad \Omega^{n,p} = \frac{R_s^{n,p}}{6A\delta_{n,p}\varepsilon_s^{n,p}(\bar{c}_e)^{0.5}} \tag{4.26c}$$

The term $U_p(\theta_p) - U_n(\theta_n)$ in equation (4.24) is the difference between the open circuit voltage for the anode and cathode. The stoichiometry ratio $\theta_{n,p}$ is the normalized solid-electrolyte interface concentration for the anode and cathode respectively.

$$\theta_{n,p} = \frac{\bar{c}_{s,e}^{n,p}}{c_{s,max}^{n,p}} \tag{4.27}$$

where $\bar{c}_s^{n,p}$ is the average bulk concentration and can be obtained as follows [1]:

$$\bar{c}_s^{n,p}(t) = \frac{3}{R_s^3} \int_0^{R_s} r^2 c_s^{n,p}(r,t) dr \tag{4.28}$$

The cell SOC and nominal capacity are defined as follows:

$$SOC = \frac{\theta_{n,p} - \theta_{0\%}}{\theta_{100\%} - \theta_{0\%}} \tag{4.29}$$

$$C_{nom} = \frac{AF\delta_{n,p}\varepsilon_s^{n,p} c_{s,\max}^{n,p}[\theta_{100\%}^{n,p} - \theta_{0\%}^{n,p}]}{3600}, \qquad [\text{Ah}] \tag{4.30}$$

4.4.4 State-space formulation

In order to the ROM to be useful for control and systems engineering, the PDEs must be rewritten in state-space representation. First, the model is discretized using the central finite difference method (CFDM), then a state-space representation is formulated.

By using the CFDM for the radial dimension r, it is possible to describe the spherical PDE by a set of ordinary differential equations (ODE). Equation (4.19) can be written as

$$\frac{\partial c_s(r,t)}{\partial t} = D_s\left(\frac{\partial^2 c_s}{\partial r^2} + \frac{2\partial c_s}{r\partial r}\right) \tag{4.31}$$

By discretizing the solid spherical particle into M_r shells along the radial dimension r as shown in Figure 4.2, such that $R_s = \Delta r \times (M_r)$, and defining $q = 1, ..., M_{r-1}$ where $r_q = q \times \Delta r$ equation (4.31) becomes:

$$\dot{c}_s^{n,p}|_q = \frac{D_s}{\Delta r^2}\left[\left(\frac{q-1}{q}\right) c_s^{n,p}|_{q-1} - 2\,c_s^{n,p}|_q + \left(\frac{q+1}{q}\right) c_s^{n,p}|_{q+1}\right] \tag{4.32}$$

The boundary condition equations (4.4) can be rewritten accordingly:

$$c_s^{n,p}|_0 = c_s^{n,p}|_1 \tag{4.33}$$

$$c_s^{n,p}|_{M_r} = c_s^{n,p}|_{M_{r-1}} + \Delta r\frac{-\bar{j}^{li}}{Fa_sD_s} = c_{se}^{n,p} \tag{4.34}$$

By substituting with the boundary conditions equations (4.33) and (4.34), and rearranging, a state-space representation for equation (4.32) can be formulated as follows:

$$\dot{c}_s^{n,p} = \mathbf{A} c_s^{n,p} + \mathbf{B} j^{li} \tag{4.35}$$

$$c_{se}^{n,p} = c_s^{n,p}|_{M_r} = c_s^{n,p}|_{M_r-1} + \mathbf{D} j^{li} \tag{4.36}$$

where the state-space matrices, A, B, and D, are obtained as follows:

$$\mathbf{A} = \Psi \begin{bmatrix} -2 & \frac{q+1}{q} & 0 & \cdots & 0 & 0 \\ \frac{q-1}{q} & -2 & \ddots & & 0 & 0 \\ 0 & \ddots & \ddots & \ddots & & \vdots \\ \vdots & & \ddots & \ddots & \ddots & 0 \\ 0 & 0 & & \ddots & -2 & \frac{q+1}{q} \\ 0 & 0 & \cdots & 0 & \frac{q-1}{q} & -\frac{q-1}{q} \end{bmatrix} \tag{4.37}$$

$$\mathbf{B} = \mathrm{Z} \begin{bmatrix} 0 \\ 0 \\ 0 \\ \vdots \\ \vdots \\ -\frac{q+1}{q} \end{bmatrix} \tag{4.38}$$

$$\mathbf{D} = -\frac{\mathrm{Z}}{\Psi} \tag{4.39}$$

where $\Psi = D_s/\Delta r^2$ and $\mathrm{Z} = 1/(\Delta r \times a_s \times F)$. The lithium concentration in the solid particle at the outer shell when $r = M_r$ is referred to as the lithium concentration at the solid-electrolyte interface $c_{se}^{n,p}$.

In this publication, the SPM is discretized into four shells $M_r = 4$. This reduces to model's state-space system to 3 states, and one output equation. The computational cost of the system in terms of CPU simulation time is approximately 1.2 sec for every 25 minutes in real time. The CPU times presented in this publication were run on a 2.30 GHz Intel processor with 16 GB RAM.

4.4.5 Thermal dependent parameters

The cell temperature varies due to nonisothermal operating conditions. Arrhenius equation governs the most significant temperature-dependent parameters such as solid phase diffusion coefficient, electrolyte ionic conductivity, electrolyte diffusional ionic conductivity.

$$\psi = \psi_{ref} exp\left[\frac{E_{act}^{\psi}}{R}\left(\frac{1}{T_{ref}} - \frac{1}{T}\right)\right] \tag{4.40}$$

where ψ is temperature dependent model parameter, ψ_{ref} is its value at T_{ref}, R is the universal gas constant and E_{act}^{ψ} is the activation energy. The fitted results for the solid diffusion coefficient and internal resistance were found to follow an Arrhenius relationship with temperature. The results are plotted in Figure 4.3, where the gray points represent the data points, and the solid-blue line represents the data fit.

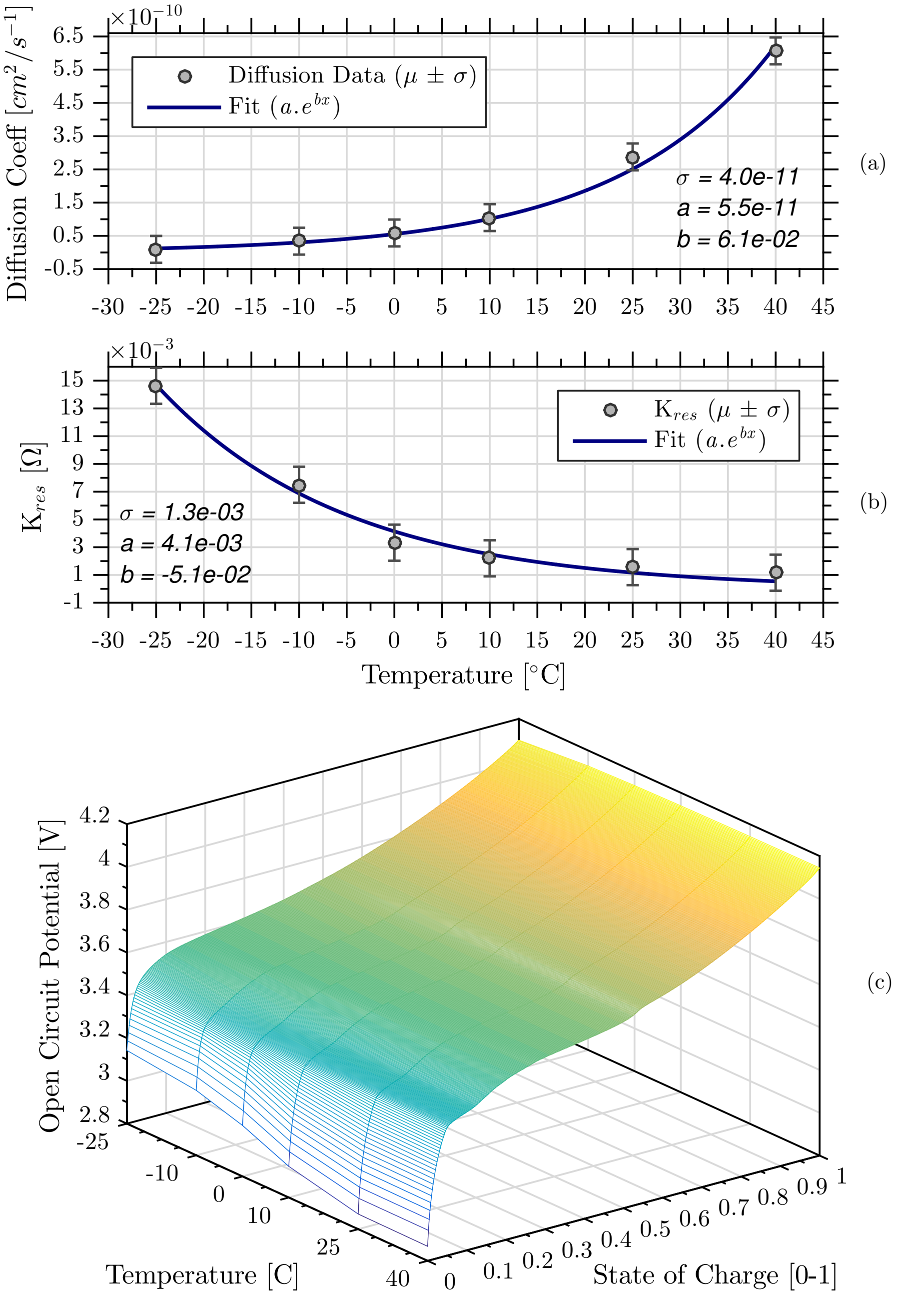

Figure 4.3: Temperature dependent parameters (a) Solid-phase diffusion coefficient (b) Internal resistance (c) Open circuit potential versus SOC.

4.5 Heat generation model

Energy conversion losses through electrical, chemical and mass transport processes are responsible for the heat generation experienced during the cell's operation. In the literature, various ways have been utilized to model the heat generation rate ranging from analytical to experimental approaches. The analytical approach as discussed by Bernadi et al.[43] calculates the heat generation rate using an energy balance that accounts for different sources of heat generation. Whereas, experimental approaches measures the heat generation rate using calorimetry techniques as described by Kobayashi et al.[40].

In this publication, the analytical approach will be considered due to the nature of our application. A complete expression for the heat losses that accounts for all the chemical reactions, mixing processes, polarization effects and electrode kinetics is often impractical. A simplified formulation derived by Berandi et al. [43] is widely used in literature. Bernardi's expression quantified the losses in an electrochemical system taking into account the enthalpy of the reactions, the enthalpy of mixing, the phase-change and the heat capacity.

The total heat sources $\dot{Q}_{gen}$ consist of four different terms and defined as follows:

$$\dot{Q}_{gen} = \dot{Q}_{rev} + \dot{Q}_{irr} + \dot{Q}_{mix} + \dot{Q}_{sr} \tag{4.41}$$

Reversible losses The first term in equation (4.41) is the reversible losses ($\dot{Q}_{rev}$) and can be calculated as shown in (4.42)

$$\dot{Q}_{rev} = IT\frac{\partial(U_p - U_n)}{\partial T} \tag{4.42}$$

The magnitude of $\dot{Q}_{rev}$ can be either positive or negative depending on the sign of the entropic coefficient. The entropic coefficient $\partial U_{p,n}/\partial T$ quantifies the magnitude of the OCP dependency on temperature and is directly correlated with the entropy change and hence the reversible losses. A common way of calculating the entropic coefficient is to discharge the cell to a predefined SOC and wait until the cell relaxes to record the equilibrium potential and then repeat at different temperature points and different SOC points. This can either be done by keeping the SOC constant and then varying the temperature or by varying the SOC while holding the temperature constant, though the latter method results in more uncertainty [44]. The accuracy of the results depends on the number of SOC points considered. It can take extended experimental procedures to get sufficient data. Some novel approaches such as electrothermal impedance spectroscopy [45] as well as methods based on calorimetry [46] are discussed in the literature.

In this publication, the OCP-curve was calculated as the average of continuously charging/discharging the cell at $C/52$. At such discharge rate, the cell is in quasi-equilibrium and the terminal voltage approximately equal to the real equilibrium value [88]. This method is convenient as it provides readings for the whole SOC range, but it can have a lower accuracy due to the relaxation effects. Tests were performed at [-25°C, -10°C, 0°C, 10°C, 25°C, and 40°C]. The entropic coefficient was then obtained by performing a linear fit to each SOC point against the six available temperatures. To obtain the entropic coefficient for both the cathode and anode separately, the value for the anode's entropic coefficient was obtained from Kumaresan et al's publication

[89], while the cathode's entropic coefficient was calculated using equation (4.43).

$$\frac{\partial U}{\partial T}_p = \frac{\partial OCV}{\partial T} + \frac{\partial U}{\partial T}_n \tag{4.43}$$

The experimental results obtained can be found in Figure 4.4. The experimental procedure for obtaining the electrode's OCP curves will be discussed in Section 4.8.

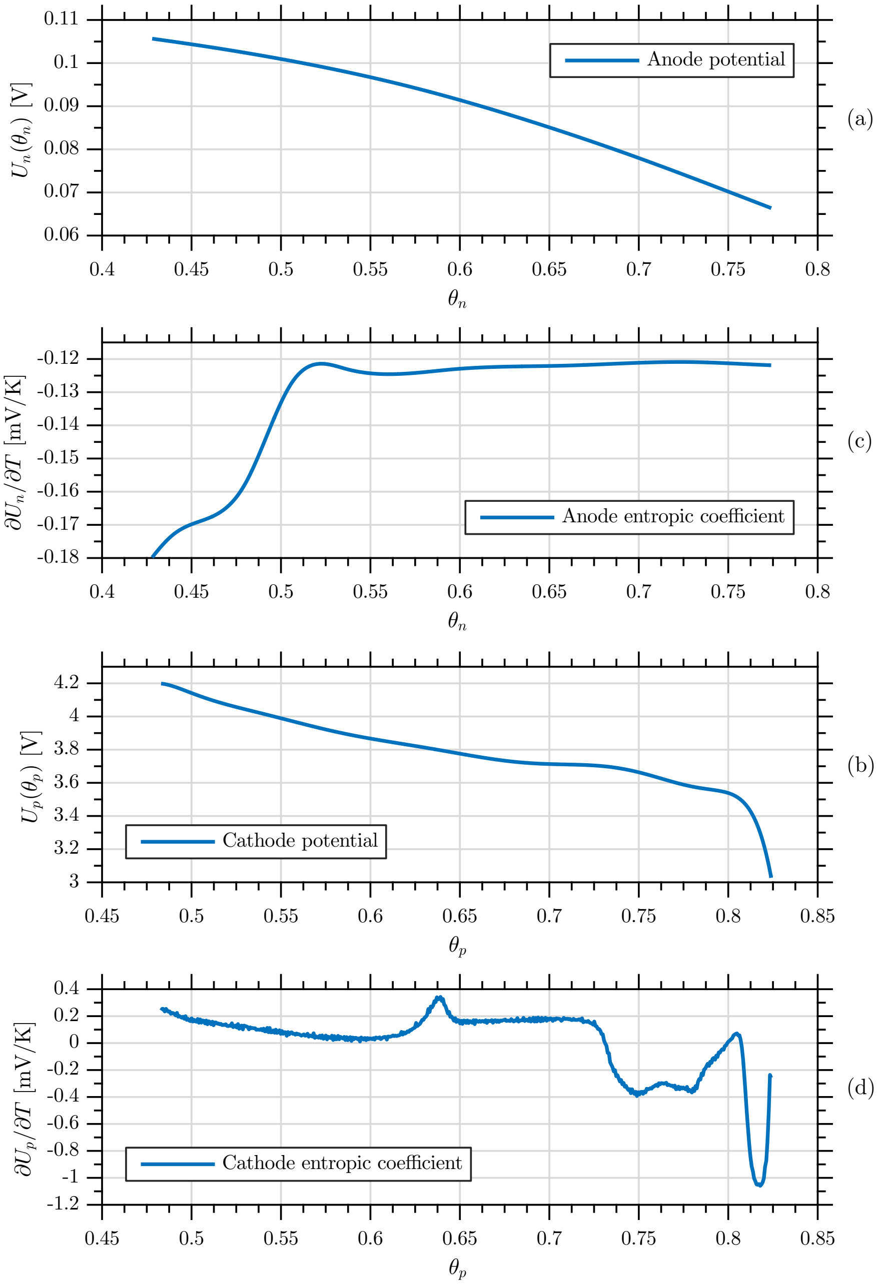

Figure 4.4: OCP for the (a) Anode, (b) Cathode and the entropic coefficient for the (c) Anode, (d) Cathode.

Irreversible losses The second term in equation (4.41) is the irreversible losses ($\dot{Q}_{irr}$) or the polarization losses. Polarization is the deviation of the cell's voltage from its equilibrium voltage due to the ohmic, activation and concentration polarization [47]. The irreversible loss is quantified by how much the instantaneous cell potential deviates from the equilibrium potential and can be calculated as shown in (4.44). Losses induced by polarization have the biggest magnitude out of all the modes of losses.

$$\dot{Q}_{irr} = I[V_t - (U_p - U_n)] \tag{4.44}$$

Heat of Mixing The third term in equation (4.41) is the heat of mixing ($\dot{Q}_{mix}$), and it models the losses released or absorbed from the formation and relaxation of the concentration gradients during the operation of a lithium-ion cell. The heat of mixing in porous insertion electrodes can be divided into four modes (i) the concentration gradients inside the spherical particles, (ii) concentration gradients inside the bulk electrolyte, (iii) concentration gradients inside the electrolyte pores of the insertion electrode, and (iv) concentration gradients inside the bulk electrode.

The heat of mixing within the spherical particles has the biggest magnitude out of these four modes and its formula as derived by Thomas et al. [48] is expressed in equation (4.45). This formula was derived using a Taylor-series expansion for the molar enthalpy of each species while neglecting the effects of pressure and density change and assuming the magnitude of the second derivative of the partial molar enthalpy to be negligible.

$$\Delta H = \frac{1}{2c_{b,\infty}\bar{V}_{b,\infty}} \frac{\partial H_A}{\partial c_a} \int (c_a - c_{a,\infty})^2 dv \tag{4.45}$$

where $c_{b,\infty}$ & $\bar{V}_{b,\infty}$ are the volume-averaged concentration and partial molar volume of species 'b', the product $c_{b,\infty}\bar{V}_{b,\infty}$ was assumed to be 1 [90]. $\partial H_a/\partial c_a$ is the change in enthalpy of mixing for species 'a' per change of concentration and can be calculated as follows:

$$\frac{\partial H_A}{\partial c_a} = -F\frac{\partial U_H}{\partial c_a} \tag{4.46}$$

where

$$U_H = U - T\frac{dU}{dT} \tag{4.47}$$

The coefficient $\partial H_A/\partial c_a$ is calculated using numerical differentiation of (4.47), where U_H is calculated using the knowledge of the OCP and the entropic coefficient of the negative and positive electrodes. The integral in (4.45) is approximated using the trapezoidal rule:

$$\int (c_A - c_{A,\infty})^2 dv = \int (c_A - c_{A,\infty})^2 4\pi r^2 dr = \sum_{i=1}^{n-1} 2\pi\Delta r \left[r_i^2(c_i - c_{avg})^2 + r_{i+1}^2(c_{i+1} - c_{avg})^2\right] \tag{4.48}$$

The power released due to this change of enthalpy during time step Δt is expressed as:

$$\dot{Q}_{mix} = \frac{\Delta H}{\Delta t} \tag{4.49}$$

Using (4.49) and (4.45) the heat of mixing can be calculated as follows:

$$\dot{Q}_{mix} = \frac{\partial}{\partial t}\left[\frac{1}{2}\frac{\partial H_A}{\partial c_a}\int (c_a - c_{a,\infty})^2 dv\right] \tag{4.50}$$

Side reactions The fourth term in equation (4.41) is the heat associated with any side reactions that may occur ($\dot{Q}_{sr}$). During normal operating conditions, this term can be neglected as discussed in [43].

Figure 4.7-c and 4.7-j shows the magnitude of each heat losses component based on the parameterization cycle and the validation cycle, respectively. The parameterization and validation are discussed later in Section 4.8. The irreversible losses have the biggest magnitude out of all the total heat losses. While the reversible losses is the second biggest of heat losses. Finally, the heat of mixing losses is negligible compared to the reversible and irreversible losses. This agrees with Thomas et al. [48] findings of the negligibility of the heat of mixing for porous insertion electrodes in well-designed cells. Now that an estimate of the heat flux can be calculated, a temperature model, therefore, has to be defined to translate the losses and the boundary conditions into the cell's temperature.

4.6 Thermal model

4.6.1 Model mathematical formulation

This section introduces the thermal model of the combined ECHTM. Due to the nature of the application and to reduce the model computational complexity, the detailed geometry of the cell's internal components were not considered and were simply abstracted by a simple 0-D model with four nodes. The four nodes lumped capacitance model is developed to capture the thermal behavior of the prismatic cell adequately as shown in Figure 4.5-a. The terminal node represents the average temperature of the positive and negative terminals. The bottom node represents the temperature change in the cell due to the temperature gradient caused by the cooling. The housing node captures the heat conduction of the outer housing shell. Finally, the core node represents the change in the core temperature of the cell.

Due to the cell's geometry, experimental setup, thermal properties, and temperature range of operation, the following assumptions and simplifications have been proposed. (i) Thermal properties are assumed to be independent of temperature since the operational temperature range of the cell is too small to show any significant dependence of the material thermal properties on temperature. (ii) The cell's core, housing, bottom, and terminals are each represented by a heat capacitor. (iii) The heat transfer from convection and radiation were assumed to be negligible.

The heat generation due to the electrochemical reaction is assumed to be localized in the cell's core, whereas the resistive losses due to the tab and current collector losses are assumed to be confined in the cell's terminal. Based on these assumptions, the heat flux due to the cell's operational losses is generated at both the terminal and the core. For each of the four nodes an ordinary differential equation (energy balance) expresses the heat exchange paths and the boundary conditions.

At the terminals, there is heat transfer to and from the core and the housing along with the losses P_t^{th} originating from the tap's restrictive losses.

$$C_t^{th}.\dot{T}_t = \frac{T_c - T_t}{R_4^{th}} + \frac{T_h - T_t}{R_5^{th}} + P_t^{th} \tag{4.51}$$

Where P_t^{th} is is determined experimentally through considering the resistivity values for both the cathode (Aluminum) and anode (copper) terminals along with the physical dimensions of the current collectors.

Similarly, at the housing heat is exchanged with the terminal, core and bottom nodes as the housing is in contact with all the nodes.

$$C_h^{th}.\dot{T}_h = \frac{T_b - T_h}{R_2^{th}} + \frac{T_c - T_h}{R_1^{th}} + \frac{T_t - T_h}{R_5^{th}} \tag{4.52}$$

At the core (sometimes referred to as the jellyroll), heat is exchanged with all the surrounding nodes and a significant heat flux is generated due to the losses at the core as described in section 4.5.

$$C_c^{th}.\dot{T}_c = \frac{T_b - T_c}{R_3^{th}} + \frac{T_t - T_c}{R_4^{th}} + \frac{T_h - T_c}{R_1^{th}} + P_c^{th} \tag{4.53}$$

The bottom node is in direct contact with the cooler underneath. Heat is exchanged through conduction to the cooler. A constant temperature boundary condition is assumed for the cooler, whose temperature is regulated by the cooling system's controller.

$$C_b^{th}.\dot{T}_b = \frac{T_k - T_b}{R_6^{th}} + \frac{T_c - T_b}{R_3^{th}} + \frac{T_h - T_b}{R_2^{th}} \tag{4.54}$$

Since both the thermal conductance and the heat capacity can be assumed to be physical constants, the system can be modeled using linear ordinary differential equations and represented in a state-space representation.

$$\dot{T} = \mathbf{A}^{\mathrm{th}}T + \mathbf{B}^{\mathrm{th}}u \tag{4.55}$$

$$T_t = \mathbf{C}^{\mathrm{th}}T + \mathbf{D}^{\mathrm{th}}u \tag{4.56}$$

where

$$\dot{T} = \begin{bmatrix} \dot{T}_t \\ \dot{T}_h \\ \dot{T}_c \\ \dot{T}_b \end{bmatrix} \tag{4.57}$$

$$u = \begin{bmatrix} P_c^{th} \\ P_t^{th} \\ T_k \end{bmatrix} \tag{4.58}$$

The state-space matrices, A, B, C and D, are obtained as follows:

$$\mathbf{A}^{\text{th}} = \begin{bmatrix} -\frac{1}{C_t^{th}}\left(\frac{1}{R_4^{th}} + \frac{1}{R_5^{th}}\right) & \frac{1}{C_t^{th}R_5^{th}} & \frac{1}{C_t^{th}R_4^{th}} & 0 \\ \frac{1}{C_h^{th}R_5^{th}} & -\frac{1}{C_h^{th}}\left(\frac{1}{R_1^{th}} + \frac{1}{R_2^{th}} + \frac{1}{R_5^{th}}\right) & \frac{1}{C_h^{th}R_1^{th}} & \frac{1}{C_h^{th}R_2^{th}} \\ \frac{1}{C_c^{th}R_4^{th}} & \frac{1}{C_c^{th}R_1^{th}} & -\frac{1}{C_c^{th}}\left(\frac{1}{R_1^{th}} + \frac{1}{R_3^{th}} + \frac{1}{R_4^{th}}\right) & \frac{1}{C_c^{th}R_3^{th}} \\ 0 & \frac{1}{C_b^{th}R_2^{th}} & \frac{1}{C_b^{th}R_3^{th}} & -\frac{1}{C_b^{th}}\left(\frac{1}{R_2^{th}} + \frac{1}{R_3^{th}} + \frac{1}{R_6^{th}}\right) \end{bmatrix} \tag{4.59}$$

$$\mathbf{B}^{\text{th}} = \begin{bmatrix} 0 & \frac{1}{C_t^{th}} & 0 \\ 0 & 0 & 0 \\ \frac{1}{C_c^{th}} & 0 & 0 \\ 0 & 0 & \frac{1}{C_b^{th}R_6^{th}} \end{bmatrix} \tag{4.60}$$

$$\mathbf{C}^{\text{th}} = \begin{bmatrix} 0 & 0 & 1 & 0 \end{bmatrix} \tag{4.61}$$

$$\mathbf{D}^{\text{th}} = [0] \tag{4.62}$$

Equations (4.59) to (4.62) describe a linear time-invariant state-space system. The system's controllability and observability is described in equation (4.63) and equation (4.64) respectively.

$$\mathbf{Co} = \begin{bmatrix} \mathbf{B} & \mathbf{AB} & \mathbf{A}^2\mathbf{B} & \mathbf{A}^3\mathbf{B} \end{bmatrix} \tag{4.63}$$

$$\mathbf{Ob} = \begin{bmatrix} \mathbf{C} & \mathbf{CA} & \mathbf{CA}^2 & \mathbf{CA}^3 \end{bmatrix}^T \tag{4.64}$$

The system's controllability and observability matrices are full ranks.

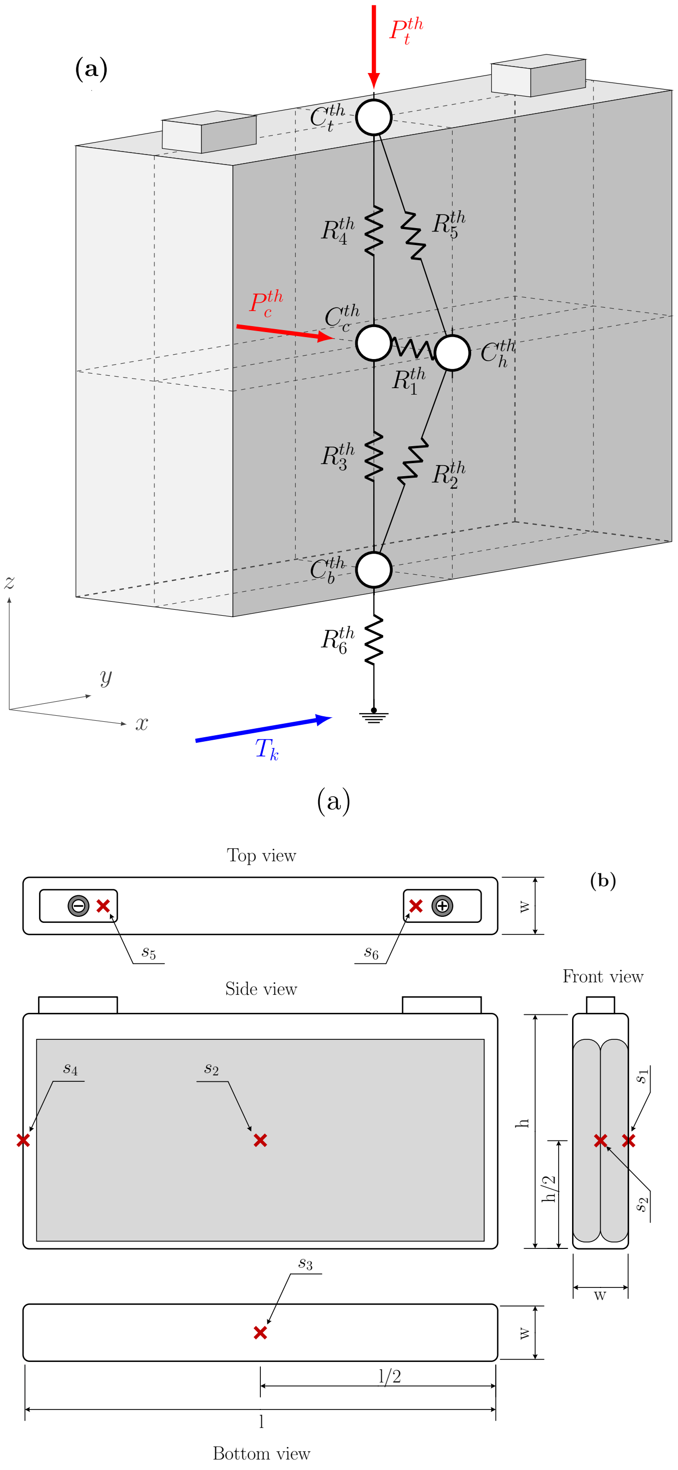

(a)

(b)

Figure 4.5: (a) A visual representation of the lumped temperature model of a prismatic cell, (b) Internal and external sensor locations.

4.7 Experimental setup

In this paper, two experimental setups were implemented. The experiments were conducted on a high-power prismatic lithium-ion battery cell to parameterize and validate each sub-model of the combined ECHTM. The prismatic cell under consideration contains a jelly roll core that consists of alternating layers of anode, separator, and cathode materials. The cell has an NMC-based cathode and graphite-based anode. The properties of the cell are given in Table 4.2.

Parameter	Value	Unit
Anode material	Graphite	-
Cathode material	NMC	-
Nominal voltage	4.25	V
Nominal capacity	26	Ah
Cell length	17.2	cm
Cell width	2.4	cm
Cell height	9.6	cm

Table 4.2: Properties of the lithium-ion cell under test.

In the first experimental setup, the experiment was performed using a Scienlab battery cycler with voltage accuracy of ± 0.05% of the measured value, current accuracy of ± 0.05% of the measured value, and temperature accuracy of ± 1 K. The voltage and current sensors are integrated to the cycler.

The thermocouples were installed both externally and internally in order to measure and validate the cell's temperature. The techniques of placing and protecting the internal thermocouple in order to ensure safety and accuracy of the measurements are discussed in details by Li et al. in [91]. The exact locations of the six internal and external thermocouples are illustrated in Figure 4.5-b. The external thermocouples were attached using heat-resistant tapes at the locations shown. Whereas, the internal thermocouples locations were chosen to ensure the safety of the cells and the accuracy of the measurement. The internal thermocouples are required in order to validate the parameterized thermal model. The Scienlab cycler used during the experiment has 12 channels, four different current profiles were tested on 12 cells (one cell per channel). The tests were performed on a cluster of three cells under the same conditions, in order to minimize the impact of any cell manufacturing variations. The output of each cluster was averaged to obtain the required variables. In order to realize an isothermal condition for the experiment. The batteries were cycled inside a thermal chamber with a continuously controlled ambient temperature. The cell was directly exposed to the chamber air. Also, the thermocouples output was monitored continuously in real time and in case the temperature is 3°C higher than the prescribed chamber temperature a wait buffer was introduced to the current profile.

In the second experimental setup, the tests were performed to parameterize the thermal model under non-isothermal conditions. During the test, in order to replicate the operating conditions in a battery pack of an electric/hybrid vehicle, the cells were placed in a closed container that minimized convection heat transfer. The container had an active cooler that ran below the cell that was directly in contact with the cell's bottom. Such tests allow the thermal dynamics of the prismatic cell to be captured. In order to mimic the vehicle operating conditions, the experiment had two controlled inputs, the cooler's temperature, and the current profile used to excite the cells.

In both setups, the measured variables are sampled every $100ms$ and then used as an input to the presented algorithm in the MATLAB/Simulink environment. Also, two cycles of C/52 CC-CV charge/discharge were conducted first in order to identify the cell's OCV and the nominal capacity of each cell.

The T_c is measured using the internal sensor (s_2), located at the core of the cell. Whereas, The T_b is measured by the external sensor (s_3), located at the bottom of the cell. Similarly, The T_h is calculated as the average of the two external temperature sensors (s_1 and s_4), located at the two sides of the cell. Finally, T_t is calculated as the mean of the two external temperature sensors (s_5 and s_6), located at the cell's negative and the positive terminals, respectively.

4.8 Parameter identification procedure

This section presents the procedure for identifying the electrochemical model and the thermal model parameters. The number of combined ECHTM parameters is relatively high if all of the parameters are considered as unknowns. In order to decrease the number of parameters to be identified, the parameterization process is divided into two steps.

In step one, the battery cell is operated under isothermal conditions using experimental inputs so as to limit the variations in the cell core temperature. The electrochemical dependent parameters are then identified at six different temperatures. The genetic algorithm (GA) was used to optimize the model parameters. The GA is theoretically proven to attain global convergence. The cost function of GA is to minimize the root mean squared error (RMSE) between the model terminal voltage output and experimental data at predefined temperature points.

In step two, the battery cell is excited under non-isothermal conditions using signals that are rich in the temperature range necessary to determine the thermal model parameters. The cost function of GA is to minimize the error between the model terminal, housing, bottom, and core temperature outputs and corresponding experimental data.

Table 4.3 summarizes the electrochemical model constants or formula-based parameters [25].

Symbol	Value		
	Anode	Separator	Cathode
α_a, α_c	0.5	-	0.5
σ	1	-	0.1
σ^{eff}	$\sigma^{eff} = \varepsilon_s^{n,p}\sigma$	-	$\sigma^{eff} = \varepsilon_s^{n,p}\sigma$
$a_s^{n,p}$	$a_s^n = \frac{3\varepsilon_s^{n,p}}{R_s}$	-	$a_s^p = \frac{3\varepsilon_s^{n,p}}{R_s}$
κ	$\kappa = 0.0158 c_e e^{\left(0.85 c_e^{1.4}\right)}$		
κ^{eff}	$\kappa^{eff} = \varepsilon_s^{n,p}\kappa$		

Table 4.3: Model parameters - constant parameters and formula-based parameters.

4.8.1 Identification of the electrochemical model parameters

In this step, a constant low-rate discharge/charge, and a highly dynamic driving cycle were used to identify the electrochemical model parameters. First, the low (C/52) discharge/charge was used to cycle the cell and the 3rd cycles was used to construct the V_{OCV} curve, to allow for SEI formation (Coulombic efficiency was in excess of 99% by this cycle). This step is used to identify the maximum electrode active material solid concentration and stoichiometry cycling range.

The negative electrode active material consists of graphite Li_xC_6. The correlation between the Li_xC_6 open-circuit potential and the negative electrode active material solid concentration has been measured in the laboratory as discussed by Farag et al. [1]. The $U_n(\theta_n)$ correlation is plotted in Figure 4.4-a. The correlation between the open-circuit potential and the positive electrode active material solid concentration is plotted in Figure 4.4-c and calculated by adding the $U_n(\theta_n)$ and the cell's measured open-circuit voltage as shown below:

$$U_p(\theta_p) = V_{OCV} + U_n(\theta_n) \tag{4.65}$$

Next, the highly dynamic driving cycle was used to identify the diffusion-related electrochemical model parameters. As shown in Figure 4.6-a, the cycle contains charge-sustaining and charge-depleting phases, which makes it rich in the frequency content necessary to identify the cell parameters. The test starts with a fully charged battery and then a current profile is applied to discharge the battery until it is fully discharged.

The identified electrochemical model parameters, with their lower and upper bounds, are summarized in Table 4.4.

Symbol	Unit	Identified values	
		Anode	Cathode
$c_{s,max}^{n,p}$	mol cm^{-3}	0.072	0.080
$\theta_{0\%}$	–	0.428	0.824
$\theta_{100\%}$	–	0.774	0.483
$\varepsilon_s^{n,p}$	–	0.958	0.950
$R_s^{n,p}$	cm	0.00026	0.000475
A	cm^2	8833.9	
$\bar{c}_e$	mol cm^{-3}	3.13*1e2	
K_{res}	Ωcm^2	Figure 4.3-a	
D_e^p	$cm^2\ s^{-1}$	Figure 4.3-b	

Table 4.4: Identified model parameters.

After the parametrization procedure by the GA, the model shows an accurate voltage prediction as shown in Figure 4.6-b. The RMSE and MAE in the terminal voltage at the six different temperatures are summarized in Table 4.5.

Core temperature [±1.5°C]	Parameterization cycle	
	RSME [V]	MAE [V]
-25°C	0.072	0.066
-10°C	0.056	0.051
0°C	0.044	0.041
10°C	0.037	0.034
25°C	0.027	0.022
40°C	0.012	0.009

Table 4.5: Electrochemical model results at different temperature - RMSE and MAE [V].

4.8.2 Identification of the thermal model parameters

In this step, the battery is excited under non-isothermal conditions using the cycle shown in Figure 4.7-a and 4.7-b. The thermal parameterization cycle is chosen to mimic real operating conditions. The cycle consists of three stages. First, the cooler is set to 5°C and the cell is subjected to low current (0 to 2 C-rate). During this phase, the battery is cooling down since the net losses are less than the cooling effect. Next, the cell is subjected to high current (2 to 12 C-rate) while keeping the cooler at 5°C. During this phase, the battery heats up. Finally, no current withdrawn from the battery and the battery is allowed to relax to a thermal equilibrium; the temperature of the different nodes eventually cool to the same temperature once the cooler is removed. This cycle sweeps through 25°C temperature range of operation. The identified thermal parameters, with their lower and upper bounds, are summarized in Table 4.6.

Symbol	Unit	Value		
		Identified	LB	UB
C_t^{th}	JK^{-1}	8.36	1	2000
C_h^{th}	JK^{-1}	36.5	1	2000
C_c^{th}	JK^{-1}	683	1	2000
C_b^{th}	JK^{-1}	47.0	1	2000
R_1^{th}	KW^{-1}	1.23	$1e-3$	500
R_2^{th}	KW^{-1}	63.0	$1e-3$	500
R_3^{th}	KW^{-1}	0.713	$1e-3$	500
R_4^{th}	KW^{-1}	193	$1e-3$	500
R_5^{th}	KW^{-1}	4.79	$1e-3$	500
R_6^{th}	KW^{-1}	0.918	$1e-3$	500

Table 4.6: Thermal model parameters.

After the identification procedure by the GA, the model shows an accurate temperature prediction as illustrated in Figures 4.7-d, 4.7-e, 4.7-f, and 4.7-g. The RMSE and MAE in the terminal, housing, core, and bottom temperatures are summarized in Table 4.7.

Symbol	Parameterization cycle	
	RSME [$°C$]	MAE[$°C$]
T_t	0.327	0.259
T_h	0.492	0.389
T_c	0.257	0.207
T_b	0.363	0.290

Table 4.7: Thermal model parameterization cycle results.

4.9 Model validation under different driving profiles

In this section, the combined ECHTM model performance is compared with experimental data to demonstrate the effectiveness of the preceding methodology. The validation cycles in this section are different from those utilized for the purpose of identification. The validation procedure is divided into three steps. First, the electrochemical model is validated under isothermal operating conditions at six different temperature points. Next, using the input of the validated electrochemical model along with the temperature dependent parameters, the thermal model is validated under non-isothermal operating conditions against the experimental thermal measurements. Finally, the combined ECHTM model is validated under non-isothermal operating conditions against the experimental voltage and temperature measurements.

4.9.1 Isothermal electrochemical model validation

The first step validates the electrochemical model under isothermal operating conditions at six different temperature points. Figure 4.6-c shows the Urban Dynamometer Driving Schedule (UDDS) cycle used for validation. The cycle was repeated at six different temperatures points [-25°C, -10°C, 0°C, 10°C, 25°C, 40°C]. Under the UDDS cycle, the error between the calculated voltages of the ROM and the measured voltage is shown in Figure 4.6-d. The RMSE at six different temperatures between the modeled voltage and the measured voltage over five consecutive cycles with 10 minutes' rest between cycles is summarized in Table 4.8.

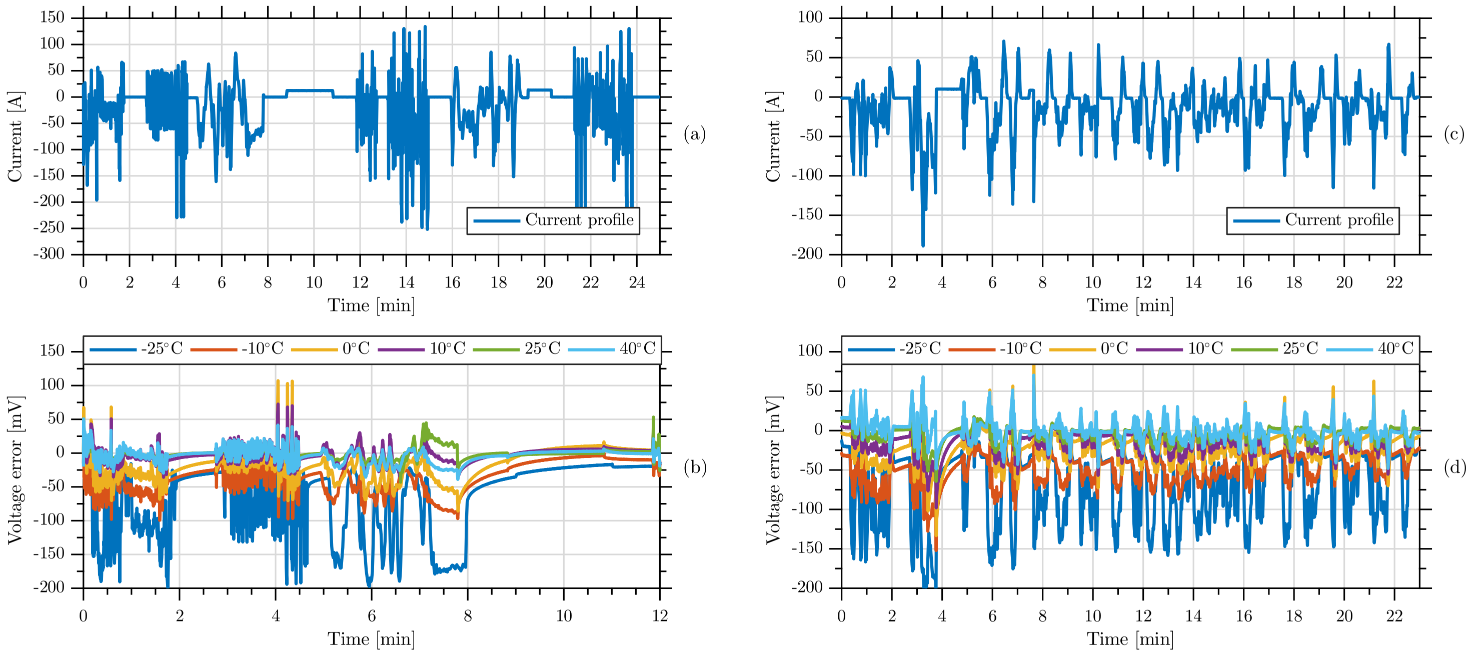

Figure 4.6: Electrochemical model (a) Parameterization cycle - current profile at 25°C (b) Parameterization cycle - voltage error at different temperatures (c) Validation cycle - current profile at 25°C (d) Validation cycle - voltage error at different temperatures.

Core temperature [±1.5°C]	Validation cycle	
	RSME [V]	MAE [V]
-25°C	0.074	0.055
-10°C	0.032	0.025
0°C	0.025	0.02
10°C	0.022	0.017
25°C	0.017	0.013
40°C	0.015	0.014

Table 4.8: Electrochemical model validation results at different temperature - RMSE and MAE [V].

4.9.2 Thermal model validation

The second set of validation data is a consecutive high charge and discharge pulses with constant cooling. The cycle sweeps the cell through 50% SOC and 20°C temperature range of operation. The experimental temperature measurements for the five sensors, the input current, and the output voltage are illustrated in Figure 4.7-h and 4.7-i. The calculated thermal model outputs are compared to the experimentally measured temperature sensors. The experimental versus modeled terminal, housing, core, and bottom temperatures are compared in Figure 4.7-k, 4.7-l, 4.7-m, 4.7-n, respectively. The blue-dotted line represents the experimental temperature, while the solid-orange represents the thermal model response. The RMSE and MAE are summarized in Table 4.9.

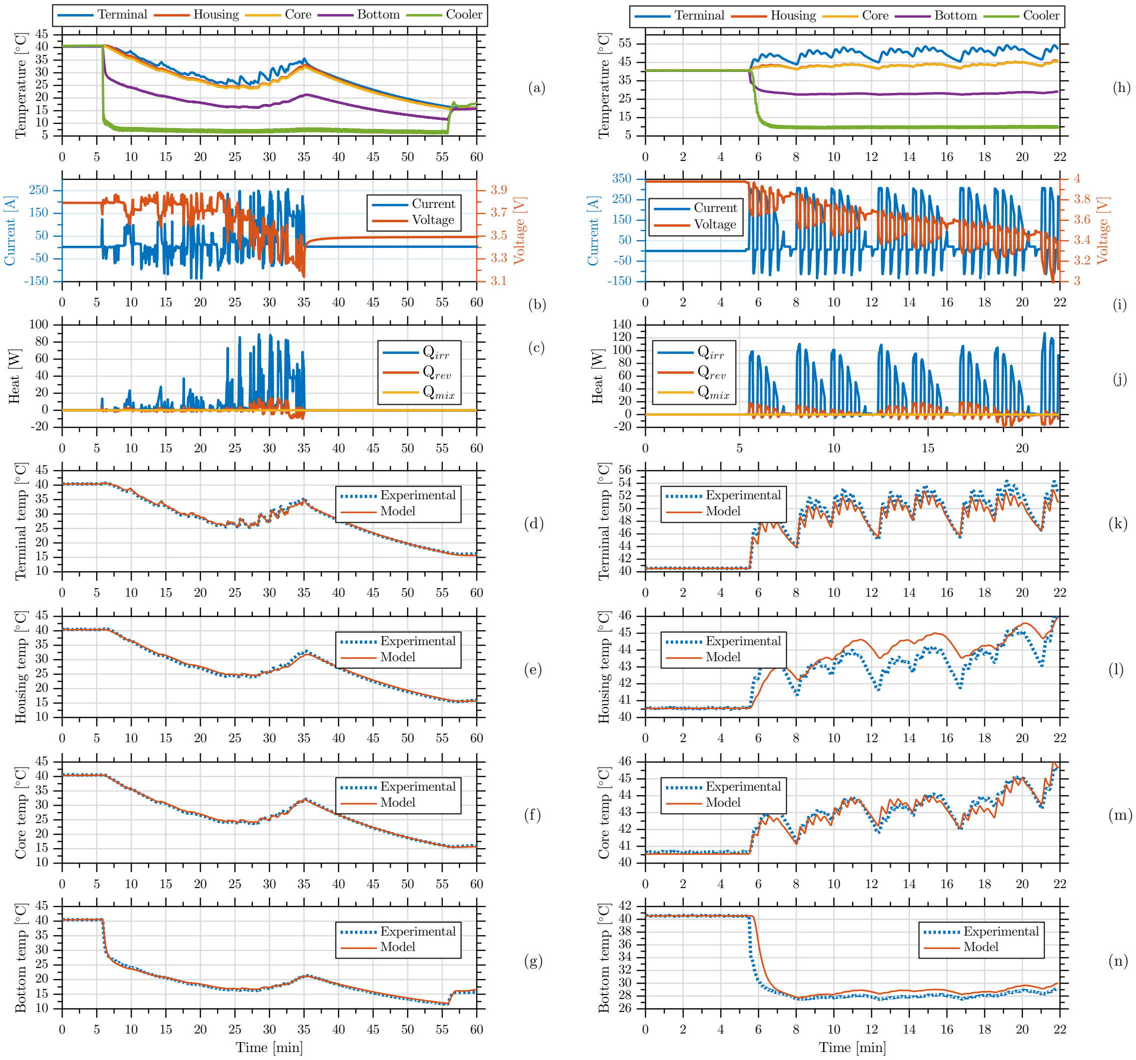

Figure 4.7: On the left side the parameterization cycle (a) Temperature profiles (b) Current and voltage profile (c) Heat losses (d) Terminal temperature (e) Housing temperature (f) Core temperature (g) Bottom temperature, on the right side the validation cycle (h) Temperature profiles (i) Current and voltage profile (j) Heat losses (k) Terminal temperature (l) Housing temperature (m) Core temperature (n) Bottom temperature.

Symbol	Validation cycle	
	RSME [$^\circ C$]	MAE [$^\circ C$]
T_t	0.901	0.675
T_h	0.810	0.591
T_c	0.305	0.245
T_b	1.286	0.718

Table 4.9: Thermal model validation cycle results.

4.9.3 Combined thermal-electrochemical model validation

The aim of the third set of validation is to validate the combined model. The cycle is rich in its temperature variation content and current frequency content. The cooler is turned on and off during operation as shown in Figure 4.8-a. The current profile has a charge-sustaining, charge-depleting, and charging phases and sweeps the full SOC range and $20^\circ C$ range of operation as illustrated in Figure 4.8-b. Figure 4.8-c shows the experimental voltage vs. the combined model output. The experimental versus modeled terminal, housing, core, and bottom temperatures are compared in Figure 4.8-d, 4.8-e, 4.8-f, 4.8-g, respectively. The blue-dotted line represents the experimental temperature, while the solid-orange represents the thermal model response. The RMSE and MAE are summarized in Table 4.10.

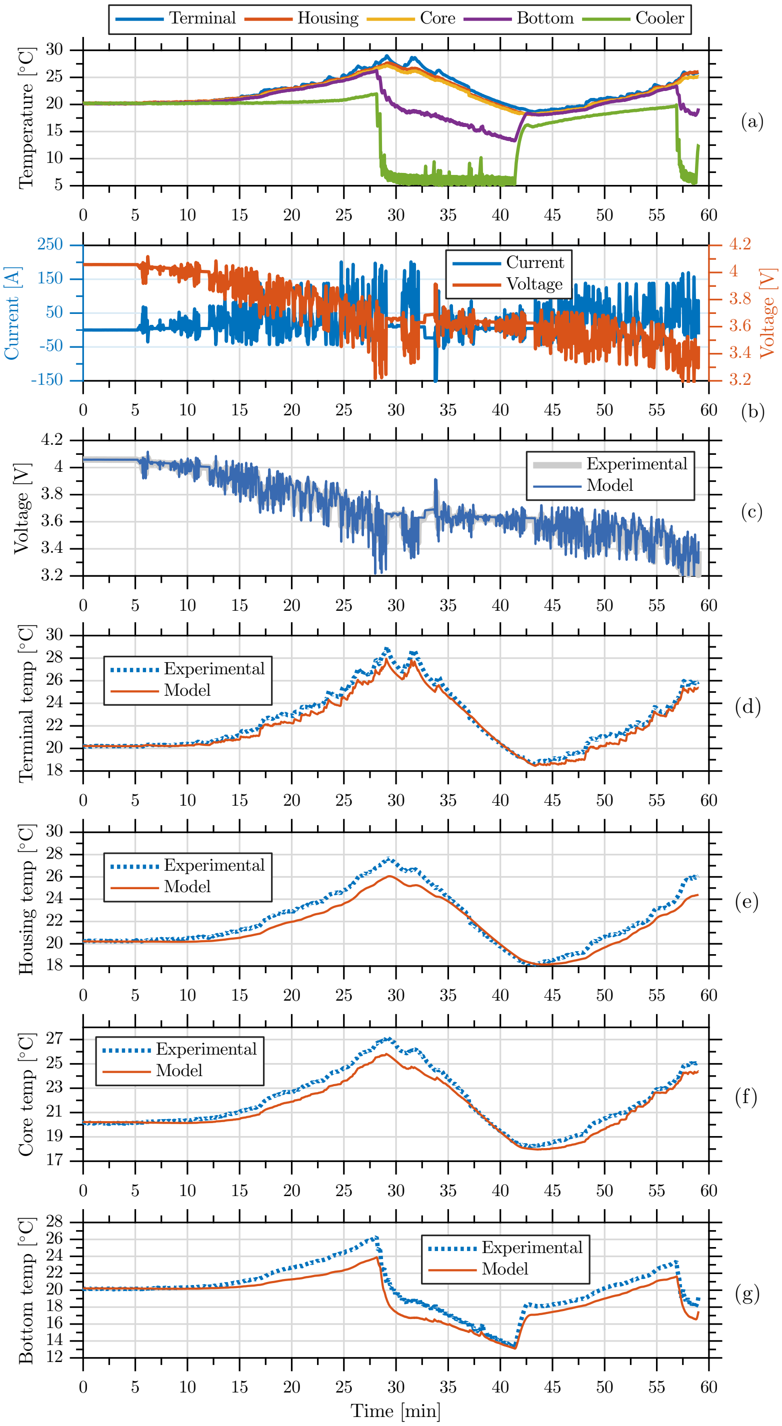

Figure 4.8: Thermal model validation cycle (a) Temperature profiles (b) Current and voltage profile (c) Terminal voltage model versus measurements (d) Terminal temperature (e) Housing temperature (f) Core temperature (g) Bottom temperature.

Symbol	Validation cycle	
	RSME	MAE
Terminal voltage [V]	0.039	0.025
$T_t[^\circ C]$	0.415	0.343
$T_h[^\circ C]$	0.673	0.555
$T_c[^\circ C]$	0.493	0.404
$T_b[^\circ C]$	1.134	0.927

Table 4.10: Combined ECHTM model results - RMSE and MAE in the terminal voltage and the measured temperatures.

4.10 Conclusion

In conclusion, a combined electrochemical, heat generation, and thermal model (ECHTM) is presented, which maintains terminal voltage and core temperature accuracy over a broad range of temperatures and state of charges. The temperature dependent electrochemical model considers the variations in the model parameters through Arrhenius equation. The proposed thermal model consists of lumped four thermal nodes interconnected by thermal resistances and capacitances. The heat generation model considers three sources of heat during operation (irreversible losses, reversible losses, and heat of mixing). The three models (electrochemical, heat generation, and thermal model) are coupled together in an iterative fashion to predict the cell's terminal voltage and core temperature accurately.

The electrochemical model parameters and the thermal model parameters are identified using a new technique that excites the model under isothermal and non-isothermal operating conditions, respectively. First, the electrochemical model with thermal dependent parameters was parameterized and validated under isothermal conditions at six different temperatures points [-25°C, -10°C, 0°C, 10°C, 25°C, 45°C]. It maintains a terminal voltage accuracy of ±80 mV at each temperature point. Next, the thermal model was parameterized and validated under non-isothermal conditions over a broad range of temperatures [-25°C to 45°C]. It predicts the core temperature with an accuracy of ±2°C. Finally, the combined ECHTM is validated under non-isothermal operating conditions, at different current rates, and temperature ranges.

The proposed combined ECHTM structure shows accurate terminal voltage and core temperature prediction at various operating conditions while maintaining a simple mathematical structure, making it ideal for real-time BMS applications. Future work will focus on using the electrochemical impedance spectroscopy (EIS) to investigate the dynamic behavior of the battery along with parameters sensitivity analysis. The use of calorimetry to quantify the heat generated within the cell. Also, incorporating iterative state of charge and core temperature estimation techniques (e.g. Extended Kalman Filter), along with developing a physics based aging model that accounts for power and capacity fade.

Nomenclature

Symbol	Description	Unit
Acronyms		
Ob	Observability matrix of a state-space model	–
Co	Controllability matrix of a state-space model	–
A	State matrix in linear state-space model state equation	–
B	Input matrix in linear state-space model state equation	–
C^{th}	Average Heat capacity	JK^{-1}
D	Input matrix in linear state-space model output equation	–
$\bar{V}$	Partial molar volume	m^3mol^{-1}
H	Enthalpy	J
R_s	Solid active material particle radius	cm
R_f	Film resistance on the electrodes surface	Ωcm^2
A	Electrode plate Area	cm^2
t_0^+	Transference number of lithium ion	–
c	Concentration of lithium ions	$molcm^{-3}$
D	Diffusion coefficient of lithium species	cm^2s^{-1}
Q	Heat transfer rate	W
q	Discretization step	–
R	Universal gas constant (R = 8.3143)	J $mol^{-1}K^{-1}$
R^{th}	Thermal conduction resistance	KW^{-1}
F	Farady's Constant (F = 96,487)	C mol^{-1}
T	Absolute Temperature	K
a_s	Active surface area per electrode unit volume	cm^2cm^{-3}
I	Applied current	A
r	Radial coordinate	cm
t	Time	s
x	Cartesian coordinate	s
j^{li}	Butler-Volmer current density	A cm^{-3}
m	Mass	kg
h	Convection heat transfer coefficient	Wm^-2K^-1

U	Equilibrium potential of an electrode	$-$
E_{act}	Activation energy	J
U_H	Enthalpy potential	V
T_c	Core Temperature	K
T_b	Bottom Temperature	K
T_t	Terminal Temperature	K
T_h	Housing Temperature	K
T_k	Cooler Temperature	K

Greek Symbols

ε_s	Active material volume fraction	$-$
ε_e	Electrolyte phase volume fraction	$-$
σ	Conductivity of solid active material	$\Omega^{-1}cm^{-1}$
κ	Electrolyte phase ionic conductivity	$\Omega^{-1}cm^{-1}$
κ_D	Electrolyte phase diffusion conductivity	$\Omega^{-1}cm^{-1}$
θ	Reference stoichiometry	$-$
α_a, α_c	Anodic and cathodic charge transfer coefficients	$-$
η	Surface overpotential of an electrode reaction	V
ϕ	Volume averaged electrical potential	V
δ	Thickness	cm
ρ	Density	kgm^{-3}

Superscripts

eff	Effective	$-$
p	Cathode	$-$
n	Anode	$-$
sep	Separator	$-$
th	Thermal	$-$

Subscripts

e	Electrolyte phase	–
s	Solid phase	–
rev	Reversible	–
irr	Irreversible	–
mix	Mixing	–
sr	Side reactions	–
amb	Ambient	–
gen	Generation	–
$conv$	Generation	–
∞	Volume average	–
ref	Reference	–

Chapter 5

A critical comparative review of lithium-ion battery modeling categories and nonlinear state of charge estimation strategies [1]

5.1 Abstract

This paper presents a critical review for the most commonly used modeling categories and non-linear state estimation strategies in lithium-ion battery energy storage applications. These modeling categories include the Behavioral models, Equivalent circuit models, and Electrochemical models. A representative model from each category is considered. The two-states enhanced self-correcting model, the two-RC model,

---

[1] Mohammed Farag and Saeid Habibi
A critical comparative review of lithium-ion battery modeling categories and nonlinear state of charge estimation strategies

and the reduced-order, electrode average electrochemical model are considered to represent the behavioral models, the equivalent circuit models, and the electrochemical models, respectively. The performance of the three models are compared with respect to their terminal voltage prediction accuracy, parameterization effort, and computational complexity. Four non-linear estimation strategies are then considered and compared by using the reduced order electrochemical model. The four estimation strategies are: the extended Kalman filter (EKF), the smooth variable structure filter (SVSF), the time-varying smoothing boundary layer (VBL-SVSF), and the unscented Kalman filter (UKF). The estimation strategies are assessed based on their rate of convergence, robustness against modeling and measurement uncertainties, computational complexity, tuning complexity, and SOC estimation accuracy under normal operating conditions.

5.2 Introduction

In the past decade and with increasing social emphasis on reducing greenhouse gas emissions, there has been a transformation in the automotive sector. Cars are being electrified or becoming more fuel efficient. To reduce emissions, the National Highway Traffic Safety Administration (NHTSA) has set standards to improve the Corporate Average Fuel Economy (CAFE) levels on a yearly basis starting from 2017 until 2025 [2]. To meet these standards, automakers are expected to produce more hybrid electric vehicles (HEVs), plug-in hybrid electric vehicles (PHEVs), or battery electric vehicles (BEVs). Lithium-ion batteries are currently most commonly used in the automotive sector for electric energy storage. This is due to their light weight, high specific power and energy, non-memory effect, and low self-discharge rate.

Automotive electrical energy storage systems consist of a battery pack and a battery management system (BMS). The BMS is essential for maximizing the performance of lithium-ion batteries against their physical limitations. The BMS is responsible for performance management which includes but is not limited to the state of charge (SOC), the state of health (SOH), and state of function (SOF) estimation algorithms, as well as cell balancing, power management, and thermal management. The battery model is one of the key elements of a BMS implementation. A robust, high fidelity, and accurate battery model is required to simulate the cell behavior in a highly dynamic environment.

Various cell models have been proposed in the literature. The presented models can be classified into three categories: (i) behavioral (or black-box), (ii) equivalent circuit, and (iii) electrochemical (or physics-based) models. The choice between the three categories is a trade-off between model complexity and accuracy.

Behavioral or Black-box Models [7, 9, 10]simulate the terminal voltage behavior of the batteries without the need for the specification of the underlying physical or electrochemical behavior. These models consist of phenomenological functions that require measured data to be used. Plett et al. [8] introduced six variations of the behavioral model: the combined, simple, zero-state hysteresis, one-state hysteresis and a non-linear enhanced self-correcting (ESC) model two states or four states. The behavioral models take into account the current direction, the OCV-SOC dependencies, and the cell's hysteresis phenomena.

Equivalent circuit models [12, 14] use electrical components such as resistors and capacitors to approximate the behavior of a battery cell [14]. They are widely used in real-time applications because of their simplicity, the low number of parameters to tune, and ease of implementation. They commonly consist of first-order, second-order, or third-order RC models in addition to the hysteresis effect. The model parameters such as resistances and capacitances are calculated by system identification using test data. Present BMSs rely on equivalent circuit models due to their simplicity and robustness, which allow these models to be implemented in real-time applications. However, these models have their limitations and do not provide insight into the electrochemical reactions that occur internally inside the cell.

Electrochemical models (ECM) or physics-based models [1, 25, 27, 92] capture the dynamic battery behavior through modeling of the chemical reactions that takes place inside the cell using partial differential equations (PDE). This type of model links physical parameters to internal electrochemical dynamics of the cell making it very accurate at the expense of computational complexity. For real-time applications, several reduced order electrochemical models have been proposed, all of which have the goal of reducing the computational complexity while maintaining the model accuracy.

In addition to battery models, BMSs also require filtering and estimation strategies that can monitor their state of operation such as SOC. Various SOC estimation techniques have been reported. These techniques can be classified into three categories: (i) coulomb counting, (ii) direct measurement methods, and (iii) estimation and adaptive techniques.

Coulomb-counting (or Ampere-Hour counting) [93, 94] calculates the SOC by integrating the battery current over a period of time. By starting at a known SOC, the value of the current integral is the direct indicator for the SOC. The main drawbacks of this method are the sensitivity to initial conditions and sensor errors. Direct measurement methods [95] calculate the SOC by direct measurement of the battery current, voltage, impedances.

Estimation and adaptive methods estimate the SOC by using a cell model and a filter or observer. The most common choice for filtering and estimation is the Extended Kalman Filter (EKF) [9, 10], the Unscented Kalman Filter (UKF) [96], the Sigma-point Kalman filter (SPKM) [97], the Particle Filter (PF) [98], and the Smooth Variable Structure Filter (SVSF) [14].

Contribution There are limited comparisons of the commonly used battery models that are wholistic in terms of terminal voltage prediction accuracy, parameterization effort, and computational complexity with respect to their real-time estimation of SOC. Therefore, this review paper contributes to the literature by carrying out a critical comparison of a number of representative models together with their use in four non-linear SOC estimation strategies. The models of interest in this publication include the Enhanced self-correcting model, the two-RC model, and the reduced-order, electrode average electrochemical model. These models were selected based on their reported accuracy in the literature [1, 9, 14]. Four non-linear SOC estimation strategies, namely EKF, UKF, VBL-SVSF, and SVSF, are then used with the above-mentioned models for estimating the SOC in real-time. Analysis of the four estimation strategies are conducted with respect to their rate of convergence, robustness against modeling and measurement uncertainties, computational complexity, tuning complexity, and SOC estimation accuracy.

Paper structure This paper is organized as follows. Section 5.3 presents an overview of three battery modeling techniques. Section 5.4 provides an overview of four non-linear estimation strategies. Experimental results are used for the comparative analysis and the experimental setup used for gathering data is described in Section 5.5. It should be noted that experimental data sets are used for both parameterization and validation purposes. Section 5.6 provides a comparative study of the modeling categories. The comparison of the estimation strategies is provided in Section 5.7. The results and discussion are presented in Section 5.8.

5.3 Battery Modeling

Three representative models from the three categories of battery models are presented in this section. The enhanced self-correcting model, the second-order RC model, and the reduced-order single particle electrochemical model are chosen to represent the behavioral models, the equivalent circuit model, and the electrochemical models, respectively. The mathematical formulation of the model is described, and their observability is assessed.

This section presents a representative model from each modeling category. First, the mathematical formulation of the model is described, and then the system observability is studied.

5.3.1 The enhanced self-correcting model

The enhanced self-correction (ESC) model is one of the most accurate behavioral models [8]. The ESC model can precisely mimic the dynamic of the battery with respect to the ohmic losses and the transient response. The state space formulation for the ESC model is as follows:

$$\begin{bmatrix} f_{1,k+1} \\ f_{2,k+1} \\ SOC_{k+1} \end{bmatrix} = \begin{bmatrix} tanh(\alpha_1) & 0 & 0 \\ 0 & tanh(\alpha_2) & 0 \\ 0 & 0 & 1 \end{bmatrix} \begin{bmatrix} f_{1,k} \\ f_{2,k} \\ SOC_k \end{bmatrix} + \begin{bmatrix} 1 \\ 1 \\ -\frac{\eta_i \Delta t}{C_n} \end{bmatrix} \begin{bmatrix} i_k \end{bmatrix} \tag{5.1}$$

$$V_{t,k} = OCV(SOC_k) - Ri_k + g_1 f_{1,k} + g_2 f_{2,k} \tag{5.2}$$

where g_1 is obtained through parameterization and g_2 is defined as follows:

$$g_2 = -g_1 \frac{(1 - tanh(\alpha_2))}{2(1 - tanh(\alpha_1))} \tag{5.3}$$

The parameteric vector is defined as follows:

$$\theta = [R^+, R^-, g_1, \alpha_1, \alpha_2] \tag{5.4}$$

where C_n is the nominal battery capacity, SOC_k is the state of charge, OCV is the open circuit voltage, f_k is the state vector of the filter, R is the internal battery resistance, and $\alpha's$ are the poles of the filter. This model has one input i_k, which is the current and one output $V_{t,k}$, which is the terminal voltage.

In order to perform an observability analysis, the model is linearized. Given the non-linearity of the output function as shown in equation (5.2), the linearized output matrix is obtained around the operating point ($S\bar{O}C$,$\bar{f}_1$,$\bar{f}_2$) as follows:

$$C = \begin{bmatrix} g_1 & g_2 & \frac{\partial OCV(SOC_k)}{\partial SOC_k}\Big|_{SOC_{k|k-1}} \end{bmatrix} \tag{5.5}$$

The observability matrix $\mathcal{O}$ is then obtained according to Equation (5.6)

$$\mathcal{O} = \begin{bmatrix} C \\ CA \\ CA^2 \end{bmatrix} \tag{5.6}$$

The system observability matrix can be obtained by substituting Equation (5.1) and Equation (5.5) into Equation (5.6) as follows:

$$\mathcal{O} = \begin{bmatrix} -g_1 & -g_2 & \frac{\partial OCV(SOC_k)}{\partial SOC_k}\Big|_{SOC_{k|k-1}} \\ -g_1 tanh(\alpha_1) & -g_2 tanh(\alpha_2) & \frac{\partial OCV(SOC_k)}{\partial SOC_k}\Big|_{SOC_{k|k-1}} \\ -g_1 tanh(\alpha_1)^2 & -g_2 tanh(\alpha_2)^2 & \frac{\partial OCV(SOC_k)}{\partial SOC_k}\Big|_{SOC_{k|k-1}} \end{bmatrix} \tag{5.7}$$

As shown by Equation (5.7), the matrix $\mathcal{O}$ is full rank. Therefore, the states of the system are observable from the terminal voltage measurement.

5.3.2 The second order RC models

The second order RC model (2RC) is widely used in real-time applications because of its accuracy, the low number of parameters to tune, and simplicity. However, these models do not provide insight into the electrochemical reactions that occur internally inside the cell. The schematic representation of the 2RC model is shown in Figure 5.1.

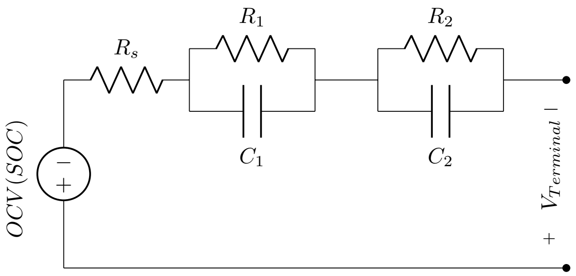

Figure 5.1: Schematic diagram of the second order RC Battery Model.

The system and measurement equations for this model are provided by Equation (5.8) and (5.9), respectively [14].

$$\begin{bmatrix} V_{1,k+1} \\ V_{2,k+1} \\ SOC_{k+1} \end{bmatrix} = \begin{bmatrix} 1-\frac{\Delta t}{R_1 C_1} & 0 & 0 \\ 0 & 1-\frac{\Delta t}{R_2 C_2} & 0 \\ 0 & 0 & 1 \end{bmatrix} \begin{bmatrix} V_{1,k} \\ V_{2,k} \\ SOC_k \end{bmatrix} + \begin{bmatrix} \frac{\Delta t}{C_1} \\ \frac{\Delta t}{C_2} \\ -\frac{\eta_i \Delta t}{C_n} \end{bmatrix} \begin{bmatrix} i_k \end{bmatrix} \tag{5.8}$$

$$V_{t,k} = OCV(SOC_k) - Ri_k - V_{1,k} - V_{2,k} \tag{5.9}$$

The parameters to be identified are given in Equation (5.10).

$$\theta = [R^+, R^-, R_1, C_1, R_2, C_2] \tag{5.10}$$

where, SOC_k is the state of charge, $V_{1,k}$ and $V_{2,k}$ are the voltage drops across the first and the second RC pair, respectively, C_n is the battery nominal capacity, R is the battery ohmic resistance, and η_i is the charging and discharging efficiency. $V_{t,k}$ is the system output and represents the battery terminal voltage, and i_k is the system input and represents the battery input.

Because the output function this system is non-linear as shown in equation (5.9), the linearized output C matrix is calculated as follows:

$$C = \begin{bmatrix} -1 & -1 & \left.\frac{\partial OCV(SOC_k)}{\partial SOC_k}\right|_{SOC_{k|k-1}} \end{bmatrix} \tag{5.11}$$

The system observability matrix can be obtained by substituting Equation (5.8) and

Equation (5.11) in Equation (5.6) as follows:

$$\mathcal{O} = \begin{bmatrix} -1 & -1 & \left.\frac{\partial OCV(SOC_k)}{\partial SOC_k}\right|_{SOC_{k|k-1}} \\ -1+\frac{\Delta t}{R_1C_1} & -1+\frac{\Delta t}{R_2C_2} & \left.\frac{\partial OCV(SOC_k)}{\partial SOC_k}\right|_{SOC_{k|k-1}} \\ -(-1+\frac{\Delta t}{R_1C_1})^2 & -(-1+\frac{\Delta t}{R_2C_2})^2 & \left.\frac{\partial OCV(SOC_k)}{\partial SOC_k}\right|_{SOC_{k|k-1}} \end{bmatrix} \tag{5.12}$$

Further to the observability matrix $\mathcal{O}$ in equation 5.12, it can be concluded that $\mathcal{O}$ is of full rank and that the model is observable. The sates of the system can, therefore, be uniquely extracted from the terminal voltage measurement.

5.3.3 Electrochemical model

The detailed mathematical formulation of the full order electrochemical model is discussed in [1] and summarized in Table 5.1.

Conservation equations	Boundary conditions	Initial conditions
Mass transport in the solid phase		
$\frac{\partial c_s^{n,p}(x,r,t)}{\partial t} = \frac{D_s}{r^2}\frac{\partial}{\partial r}\left[r^2 \frac{\partial c_s^{n,p}(x,r,t)}{\partial r}\right]$ (5.13)	$\left.\frac{\partial c_s^{n,p}}{\partial r}\right\|_{r=0} = 0,$ $\left.\frac{\partial c_s^{n,p}}{\partial r}\right\|_{r=R_s^{n,p}} = \frac{-j^{li}}{D_s a_s F}$ (5.14)	$c_s^{n,p}(x,r,t_0) =$ $c_{s_0}^{n,p}(x,r)$ (5.15)
Mass transport in the electrolyte		
$\frac{\partial \varepsilon_e c_e(x,t)}{\partial t} = D_e^{eff}\frac{\partial^2 c_e(x,t)}{\partial x^2} + \frac{1-t_0^+}{F} j^{li}$ (5.16)	$\left.\frac{\partial c_e^n}{\partial x}\right\|_{x=0} = 0,\ \left.\frac{\partial c_e^p}{\partial x}\right\|_{x=L} = 0$ (5.17)	$c_e(x,t_0) = c_{e_0}(x)$ (5.18)
Potential in the solid electrodes		
$\sigma^{eff}\frac{\partial^2}{\partial x^2}\phi_s(x,t) = j^{li}$ (5.19)	$\left.\frac{\partial}{\partial x}\phi_s(x,t)\right\|_{x=0,L} = \frac{-I}{A\sigma^{eff}}$ $\left.\frac{\partial}{\partial x}\phi_s(x,t)\right\|_{x=\delta_n,\delta_n+\delta_{sep}} = 0$ (5.20)	$\phi_s(x,t_0) = \phi_{s,0}(x)$ (5.21)
Potential in the electrolyte		
$\kappa^{eff}\frac{\partial^2}{\partial x^2}\phi_e(x,t) + \kappa_D^{eff}\frac{\partial^2}{\partial x^2}\ln c_e = -j^{li}$ (5.22)	$\left.\frac{\partial}{\partial x}\phi_e(x,t)\right\|_{x=0,L} = 0$ (5.23)	$\phi_e(x,t_0) = \phi_{e,0}(x)$ (5.24)

Butler-Volmer kinetics equations
$j^{li} = a_s j_0 \left[\exp\left(\frac{\alpha_a F}{RT}\eta\right) - \exp\left(-\frac{\alpha_c F}{RT}\eta\right)\right] \quad (5.25)$
Cell potential equations
$V = \phi_s(x = L) - \phi_s(x = 0) - R_f \frac{I}{A} \quad (5.26)$

Table 5.1: The full-order electrochemical model PDEs and their boundary conditions and initial conditions.

The mathematical formulation, describing the full order electrochemical model of equations (5.13) to (5.26), is presented in Figure 5.2.

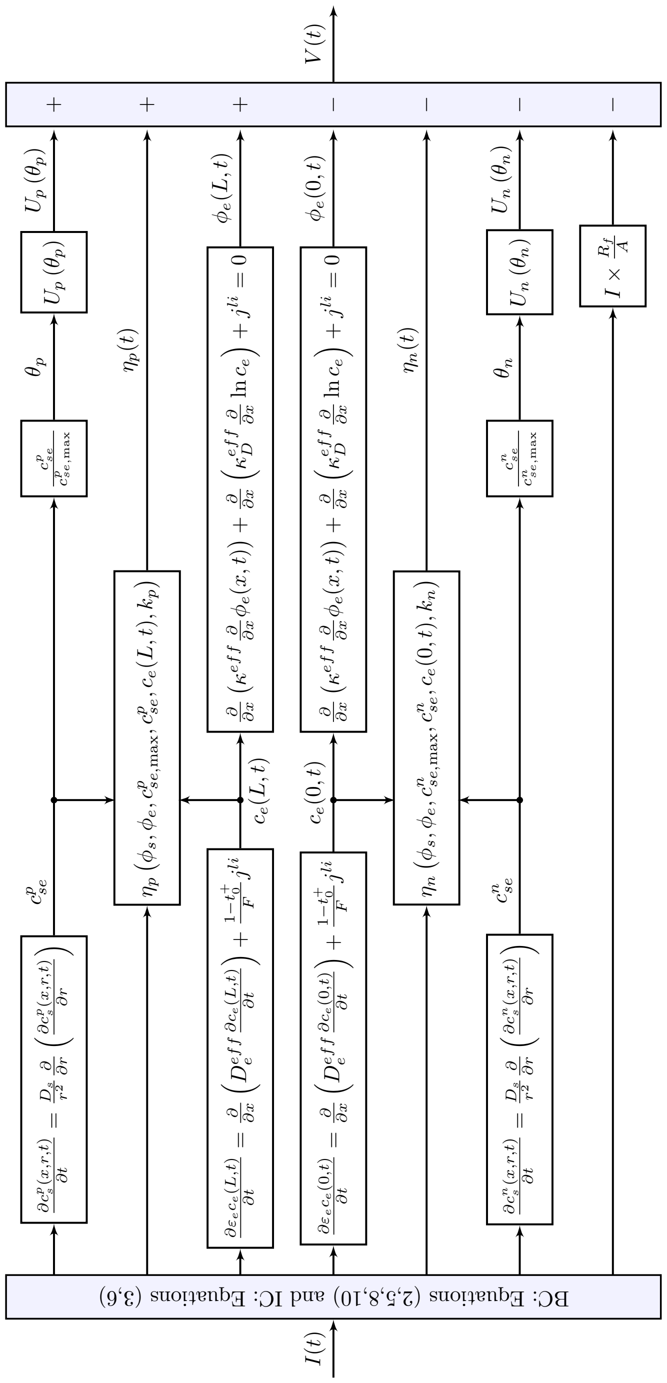

Figure 5.2: Block diagram representation of the coupled nonlinear partial differential equations in the full order electrochemical model. [1]

In order to run the electrochemical model in real-time applications, some assumptions and simplifications need to be made. These assumptions and simplifications reduce the computational complexity of the full order model (FOM). The simplification assumptions are as follows:

- constant and uniform lithium concentration in the electrolyte c_e, this results in equation (5.16) being simplified to a constant average value as shown in equation (5.28).
- As a result of the uniform lithium concentration in the electrolyte, the solid particle distribution along the electrode is neglected.
- The dependence of model parameters on temperature and aging are neglected. These assumptions result in a reduced order model (ROM) that describes the diffusion dynamics within the electrodes using two particles, one for each electrode. The ROM set of equations is summarized in Table 5.2.

Conservation Equation	
ROM - Mass transport in the solid phase	
$\frac{\partial c_s^{n,p}(r,t)}{\partial t} = \frac{D_s}{r^2}\frac{\partial}{\partial r}\left[r^2 \frac{\partial c_s^{n,p}(r,t)}{\partial r}\right]$	(5.27)
ROM - Mass transport in the electrolyte	
$c_e(x,t) = \bar{c}_e$	(5.28)
ROM - Potential in the solid electrodes	
$\frac{\partial}{\partial x}\left(\sigma^{eff}\frac{\partial}{\partial x}\phi_s(x,t)\right) = \bar{j}^{li}_{n,p}$	(5.29)
$\frac{\partial}{\partial x}\left(\kappa^{eff}\frac{\partial}{\partial x}\phi_e(x,t)\right) = -\bar{j}^{li}_{n,p}$	(5.30)
ROM - Butler-Volmer kinetics equation	
$\bar{j}^{li}_{n,p} = \frac{I}{A\delta_{n,p}}$	(5.31)
ROM - Cell potential equations	
$V(t) = [U_p(\theta_p) - U_n(\theta_n)] + \vartheta_\eta^{n,p}(\theta_{n,p}, I) - IK_{res}$	(5.32a)
$where \quad K_{res} = \frac{1}{A}\left[R_f + \frac{(\delta_n + 2\delta_{sep} + \delta_p)}{2\kappa^{eff}}\right]$	(5.32b)
$and \quad \vartheta_\eta^{n,p}(\theta_{p,n}, I) = \frac{RT}{\alpha_a F}\ln\frac{\xi_p + \sqrt{\xi_p^2 + 1}}{\xi_n + \sqrt{\xi_n^2 + 1}}$	(5.32c)
$and \quad \xi_{n,p} = \Omega^{n,p}\frac{I}{\left(c_{s,\max}^{n,p}c_{se}^{n,p} - c_{se}^{n,p^2}\right)^{0.5}}$	(5.32d)
$and \quad \Omega^{n,p} = \frac{R_s^{n,p}}{6A\delta_{n,p}\varepsilon_s^{n,p}(\bar{c}_e)^{0.5}}$	(5.32e)

Table 5.2: Final set of reduced-order model equations.

The mathematical formulation, describing the reduced order electrochemical model (ROM) equations (5.27) to (5.32), is presented in Figure 5.3, where the blue-colored constants represent the model parameters.

The ROM parameters to be identified are also given in Equation (5.33).

$$\theta = [A, c_{s,max}^{n,p}, \theta_{100\%}^{n,p}, \theta_{0\%}^{n,p}, K_{res}, D_s^{n,p}] \tag{5.33}$$

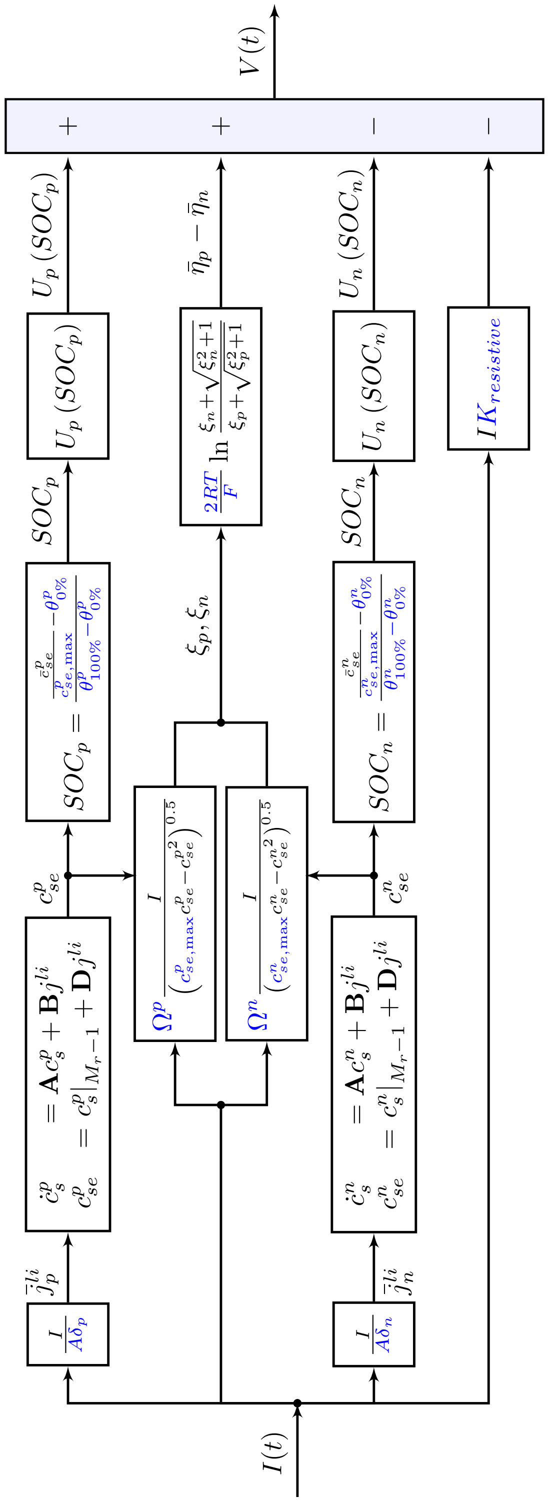

Figure 5.3: Block diagram representation for the reduced-order, electrode-average model [1].

In order to be able to run the ROM in the electronic control unit (ECU) of the battery management system (BMS), the model has to be formulated in a state-space form. The central finite difference method (CFDM) is used to discretize the model, and then a state-space representation is formulated. A state space representation for equations (5.27) to (5.32) is presented in details in [14] and can be formulated as follows:

$$\dot{c}_s^{n,p} = \mathbf{A} c_s^{n,p} + \mathbf{B} j^{li} \tag{5.34}$$

$$c_{se}^{n,p} = c_s^{n,p}|_{M_r} = c_s^{n,p}|_{M_r - 1} + \mathbf{D} j^{li} \tag{5.35}$$

The state-space system and measurement matrices are as follows:

$$\mathbf{A} = \Psi \begin{bmatrix} -2 & \frac{q+1}{q} & 0 & \cdots & 0 & 0 \\ \frac{q-1}{q} & -2 & \ddots & & 0 & 0 \\ 0 & \ddots & \ddots & \ddots & & \vdots \\ \vdots & & \ddots & \ddots & \ddots & 0 \\ 0 & 0 & & \ddots & -2 & \frac{q+1}{q} \\ 0 & 0 & \cdots & 0 & \frac{q-1}{q} & -\frac{q-1}{q} \end{bmatrix} \tag{5.36}$$

$$\mathbf{B} = \mathrm{Z} \begin{bmatrix} 0 \\ 0 \\ 0 \\ \vdots \\ \vdots \\ -\frac{q+1}{q} \end{bmatrix} \tag{5.37}$$

$$\mathbf{D} = -\frac{\mathrm{Z}}{\Psi} \tag{5.38}$$

where $\Psi = D_s/\Delta r^2$ and $\mathrm{Z} = 1/(\Delta r a_s F)$. The lithium concentration at the solid-electrolyte interface $c_{se}^{n,p}$ is the lithium concentration in the solid particle at the outer shell when $r = M_r$.

In order to be able to compare the single particle reduced order model (SPM) to the equivalent circuit model and the enhanced self-correcting model, the same number of states has to be considered in the three models. The SPM is discretized into four shells as follows:

$$A = \Psi \begin{bmatrix} -2 & 2 & 0 \\ 1/2 & -2 & 3/2 \\ 0 & 2/3 & -2/3 \end{bmatrix} \tag{5.39}$$

$$B = \mathrm{Z} \begin{bmatrix} 0 \\ 0 \\ -4/3 \end{bmatrix} \tag{5.40}$$

The physical quantity related to the battery state of charge is the solid concentration at the electrodes. The SOC is defined as follows:

$$SOC = \frac{\theta_{n,p} - \theta_{0\%}}{\theta_{100\%} - \theta_{0\%}} \tag{5.41}$$

where the stoichiometry ratio $\theta_{n,p}$ is the normalized solid-electrolyte interface concentration for the negative and positives electrodes, respectively.

$$\theta_{n,p} = \frac{\overline{c}_{s,e}^{n,p}}{c_{s,max}^{n,p}} \tag{5.42}$$

The single particle reduced order model described in equation (5.34) and (5.35) considers the diffusion effects in two solid material particles, one from the anode and one from the cathode.

As presented in [16] a system that considers a particle from the anode and the cathode is weakly observable due to the cell voltage dependence on the difference between the open circuit voltages $[U_p(\theta_p) - U_n(\theta_n)]$.

In order to mitigate the observability limitation, a relation between the positive and negative electrode average solid concentrations presented in (5.43) and is used to correlate the negative electrode stoichiometry to the positive electrode stoichiometry [16].

$$\theta^n = (\theta^p - \theta^p_{0\%}) \left[\frac{\theta^n_{100\%} - \theta^n_{0\%}}{\theta^p_{100\%} - \theta^p_{0\%}} \right] + \theta^n_{0\%} \tag{5.43}$$

Using the above formula and by linearizing the output equation (5.32) around the operating point, the linearized C matrix can be written as follows:

$$C = \begin{bmatrix} 0 & 0 & \frac{\partial V}{\partial \, \bar{c}^p_s|_{M_r-1}} \end{bmatrix} \tag{5.44}$$

where

$$\frac{\partial V}{\partial \, \bar{c}^p_s|_{M_r-1}} = \frac{\partial U_p}{\partial \bar{c}^p_{se}} \frac{\partial \bar{c}^p_{se}}{\partial \, \bar{c}^p_s|_{M_r-1}} - \frac{\partial U_n}{\partial \bar{c}^n_{se}} \frac{\partial \bar{c}^n_{se}}{\partial \, \bar{c}^p_s|_{M_r-1}} \tag{5.45}$$

Substituting (5.42) and (5.43) in equation (5.45), (5.46) is obtained as follows:

$$\frac{\partial V}{\partial \, \bar{c}^p_s|_{M_r-1}} = \frac{\partial U_p}{\partial \bar{c}^p_{se}} - \frac{\partial U_n}{\partial \bar{c}^n_{se}} \left[\frac{c^n_{s,max}}{c^p_{s,max}} \frac{\theta^n_{100\%} - \theta^n_{0\%}}{\theta^p_{100\%} - \theta^p_{0\%}} \right] \tag{5.46}$$

Finally the observability matrix can be written as follows:

$$\mathcal{O} = \Psi \begin{bmatrix} 0 & 0 & \frac{\partial V}{\partial \bar{c}_s^p\big|_{M_{r-1}}} \\ 0 & \frac{2}{3}\frac{\partial V}{\partial \bar{c}_s^p\big|_{M_{r-1}}} & -\frac{2}{3}\frac{\partial V}{\partial \bar{c}_s^p\big|_{M_{r-1}}} \\ \frac{1}{3}\frac{\partial V}{\partial \bar{c}_s^p\big|_{M_{r-1}}} & -\frac{16}{9}\frac{\partial V}{\partial \bar{c}_s^p\big|_{M_{r-1}}} & \frac{13}{9}\frac{\partial V}{\partial \bar{c}_s^p\big|_{M_{r-1}}} \end{bmatrix} \tag{5.47}$$

The positive electrode solid concentrations that constitute the states are observable from the terminal voltage measurement because of the full rank of the observability matrix $\mathcal{O}$.

5.4 Filtering and estimation

Four common filtering strategies are considered in this section, namely the Extended Kalman Filter (EKF), Unscented Kalman Filter (UKF), the time-varying smoothing boundary layer (VBL-SVSF), and the Smooth Variable Structure Filter (SVSF).

5.4.1 The extended Kalman filter

The Extended Kalman Filter (EKF) is one of the most commonly used estimation methods and is a rendition of the well-known Kalman Filter for nonlinear systems [99]. A generic nonlinear system can be described as follows:

$$\hat{x}_{k+1} = f(x_k, u_k) + w_k \tag{5.48}$$

$$z_{k+1} = h(x_{k+1}) + v_{k+1} \tag{5.49}$$

where, $f(x,u)$ and $h(x)$ are nonlinear functions of system and measurement models, and w and v are the system and measurement noises, with covariance matrices Q and R, respectively. In the EKF algorithm, the nonlinear functions of system and measurement models are used to calculated a priori state estimates and predicted measurements. In EKF, the model needs to be linearized around the prior estimate [99] as follows:

$$F_k = \left.\frac{\partial f(x,u)}{\partial x}\right|_{x=\hat{x}_{k|k},u_k} \tag{5.50}$$

$$H_{k+1} = \left.\frac{\partial h(x)}{\partial x}\right|_{x=\hat{x}_{k+1|k}} \tag{5.51}$$

The a priori state estimate and the corresponding covariance matrix are calculated as:

$$\hat{x}_{k+1|k} = f(\hat{x}_{k|k}, u_k) \tag{5.52}$$

$$P_{k+1|k} = F_k P_{k|k} F_k^T + Q_k \tag{5.53}$$

The measurement error $e_{z,k+1|k}$ and its corresponding covariance are then calculated as:

$$e_{z,k+1|k} = z_{k+1} - h(\hat{x}_{k+1|k}) \tag{5.54}$$

$$S_{k+1} = H_{k+1} P_{k+1|k} H_{k+1}^T + R_{k+1} \tag{5.55}$$

The next step is the calculation of the EKF gain as below.

$$K_{k+1}^{EKF} = P_{k+1|k} H_{k+1}^T S_{k+1}^{-1} \tag{5.56}$$

The a posteriori state estimation and its corresponding covariance matrix are calculated as:

$$\hat{x}_{k+1|k+1} = \hat{x}_{k+1|k} + K_{k+1}^{EKF} e_{z,k+1|k} \tag{5.57}$$

$$P_{k+1|k+1} = (I - K_{k+1}^{EKF} H_{k+1}) P_{k+1|k} \tag{5.58}$$

Due to the linearization process, the EKF estimation might be prone to instabilities for severely nonlinear systems [100].

5.4.2 The unscented Kalman filter

The unscented Kalman filter (UKF) is a nonlinear filtering strategy [101] that relies on a weighted statistical mapping using the nonlinear model. A standard form of UKF is provided in [102] and will be discussed in this paper. A deterministic sampling technique, namely unscented transform, is used in UKF strategy to provide more accurate estimates of the state mean and covariance. A finite number of weighted sample points around the state mean called sigma points, are selected and then propagated through the nonlinear functions to provide an approximation of mean and covariance of the estimated states. When the noise is additive, the UKF algorithm may be summarized as follows [102]. The first step is the generation of sigma points. The n-dimensional state vector, with mean $\hat{x}_{k|k}$ and covariance $P_{k|k}$, is approximated by 2n+1 sigma points. The 2n+1 sigma points are calculated as follows [102]:

$$\chi_{o,k|k} = \hat{x}_{k|k} \tag{5.59}$$

$$\chi_{i,k|k} = \hat{x}_{k|k} + \left(\sqrt{(n+\lambda)P_{k|k}}\right)_i, i = 1, ..., n \tag{5.60}$$

$$\chi_{i,k|k} = \hat{x}_{k|k} - \left(\sqrt{(n+\lambda)P_{k|k}}\right)_i, i = n+1, ..., 2n \tag{5.61}$$

where, $\left(\sqrt{(n+\lambda)P_{k|k}}\right)_i$ i is the i^{th} row or column of the matrix square root of $(n+\lambda)P_{k|k}$. These sigma points are in turn propagated through the nonlinear system model of (5.48), and then the predicted state estimate is calculated as their weighted sum, as follow [102]:

$$\chi_{i,k+1|k} = f(\chi_{i,k|k}, u_k) \tag{5.62}$$

$$\hat{x}_{k+1|k} = \sum_{i=0}^{2n} \omega_{m,i}\chi_{i,k+1|k} \tag{5.63}$$

The predicted state covariance is then calculated as:

$$P_{k+1|k} = \sum_{i=0}^{2n} \omega_{c,i}(\chi_{i,k+1|k} - \hat{x}_{k+1|k})(\chi_{i,k+1|k} - \hat{x}_{k+1|k})^T + Q \tag{5.64}$$

where the weights for the state and covariance are given by:

$$\omega_{m,0} = \frac{\lambda}{n+\lambda} \tag{5.65}$$

$$\omega_{c,0} = \frac{\lambda}{n+\lambda} + 1 + \beta - \alpha^2 \tag{5.66}$$

$$\omega_{m,i} = \omega_{c,i} = \frac{1}{2(n+\lambda)}, i = 1, ..., 2n \tag{5.67}$$

$$\lambda = \alpha^2(n+\kappa) - L \tag{5.68}$$

where α, κ, β are the UKF design parameters. To calculate the predicted measurement, the sigma points are propagated through the nonlinear measurement function of equation (5.49), as follows:

$$Z_{i,k+1|k} = h(\chi_{i,k+1|k}) \tag{5.69}$$

$$\hat{z}_{k+1|k} = \sum_{i=0}^{2n} \omega_{m,i} Z_{i,k+1|k} \tag{5.70}$$

The measurement covariance is then calculated as:

$$P_{zz,k+1|k} = \sum_{i=0}^{2n} \omega_{c,i} (Z_{i,k+1|k} - \hat{z}_{k+1|k})(Z_{i,k+1|k} - \hat{z}_{k+1|k})^T + R \tag{5.71}$$

The cross-covariance between measurement and state is calculated as follows:

$$P_{xz,k+1|k} = \sum_{i=0}^{2n} \omega_{c,i} (\chi_{i,k+1|k} - \hat{x}_{k+1|k})(Z_{i,k+1|k} - \hat{z}_{k+1|k})^T \tag{5.72}$$

The UKF gain is then calculated as below:

$$K_{k+1}^{UKF} = P_{xz,k+1|k} P_{zz,k+1|k}^{-1} \tag{5.73}$$

The update step of the UKF is similar to EKF and as follows:

$$\hat{x}_{k+1|k+1} = \hat{x}_{k+1|k} + K_{k+1}^{UKF} (z_{k+1} - \hat{z}_{k+1|k}) \tag{5.74}$$

$$P_{k+1|k+1} = P_{k+1|k} - K_{k+1}^{UKF} P_{zz,k+1|k} (K_{k+1}^{UKF})^T \tag{5.75}$$

The computational complexities of EKF and UKF are roughly of the same order[99], however for severely nonlinear systems UKF becomes more advantageous over EKF.

5.4.3 The smooth variable structure filter

The smooth variable structure filter (SVSF) is a model-based estimation strategy based on the variable structure theory [103]. This strategy uses a hyperplane along the desired state trajectory in an effort to improve upon stability and robustness issues of the estimation process. The objective is to push the estimated states towards the hyperplane and then keep them within a vicinity of the actual state through a corrective gain. The SVSF algorithm can be applied to both linear systems and nonlinear systems. A summary of the SVSF estimation is provided in this section [104]. The predicted state estimation and its corresponding a priori measurement error are calculated as:

$$\hat{x}_{k+1|k} = f(\hat{x}_{k|k}, u_k) \tag{5.76}$$

$$e_{z,k+1|k} = z_{k+1} - h(\hat{x}_{k+1|k}) \tag{5.77}$$

Then, the SVSF corrective gain and updated state estimates are respectively calculated as follows:

$$K_{k+1}^{SVSF} = H_{k+1}^{-1} \left(\left| e_{z,k+1|k} \right|_{abs} + \gamma \left| e_{z,k|k} \right|_{abs} \right) \circ sat \left(\frac{e_{z,k+1|k}}{\psi} \right) \tag{5.78}$$

$$\hat{x}_{k+1|k+1} = \hat{x}_{k+1|k} + K_{k+1}^{SVSF} \tag{5.79}$$

The SVSF gain is a function of the a priori and the a posteriori measurement error vectors $e_{z,k+1|k}$ and $e_{z,k|k}$; the smoothing boundary layer width ψ, and the SVSF convergence rate γ with elements $0 \leqslant \gamma_i < 1$; and linearized measurement matrix, H.

The a posteriori measurement error to be used in the next step is then calculated as:

$$e_{z,k+1|k+1} = z_{k+1} - h(\hat{x}_{k+1|k+1}) \tag{5.80}$$

The SVSF corrective gain is designed in a way that according to [104] making the estimation process stable and convergent to an existence subspace. The SVSF estimation is inherently robust and stable to modeling uncertainties because of its discontinuous corrective gain outside of the smoothing boundary layer. This makes SVSF estimation particularly suitable when the system model is not well-known [104].

5.4.4 The time-varying smoothing boundary layer - VBL-SVSF

The time-varying smoothing boundary layer (VBL-SVSF) was first introduced by Gadsden et al. [105] in order to increase the estimation accuracy and avoid the chattering effect. On the one hand, The SVSF estimation accuracy is reduced by the chattering effect caused by the SVSF gain definition. On the contrary, the chattering effect drastically enhances filter robustness and stability against modeling errors and uncertainties [104].

To obtain the VBL formulation, a correlation between the partial derivative of the trace of a posteriori covariance and the smoothing boundary layer term was introduced to the filter gain derivation. The VBL-SVSF prediction phase is similar to Equation (5.76) and (5.77).

The time-varying smoothing boundary layer (VBL) is calculated as follows:

$$S_{k+1} = H_{k+1} P_{k+1|k} H_{k+1}^T + R_{k+1} \tag{5.81}$$

$$A_{k+1} = \left|e_{z,k+1|k}\right|_{Abs} + \gamma \left|e_{z,k|k}\right|_{Abs} \tag{5.82}$$

$$\psi_{k+1} = \left(\bar{A}_{k+1}^{-1} H_{k+1} P_{k+1|k} H_{k+1}^T S_{k+1}^{-1}\right)^{-1} \tag{5.83}$$

The VBL-SVSF corrective gain is calculated as follows:

$$K_{k+1}^{VBL-SVSF} = H_{k+1}^{-1} \bar{A}_{k+1} \psi_{k+1}^{-1} \tag{5.84}$$

$$\hat{x}_{k+1|k+1} = \hat{x}_{k+1|k} + K_{k+1}^{VBL-SVSF} e_{z,k+1|k} \tag{5.85}$$

$$P_{k+1|k+1} = \left(I - K_{k+1} H_{k+1}\right) P_{k+1|k} (I - K_{k+1} H_{k+1})^T + K_{k+1} R_{k+1} K_{k+1}^T \tag{5.86}$$

$$e_{z,k+1|k+1} = z_{k+1} - h\left(\hat{x}_{k+1|k+1}\right) \tag{5.87}$$

Similar to the SVSF, the VBL-SVSF works in a predictor -corrector fashion, the main difference is the corrective gain calculation. The VBL-SVSF improves the estimation accuracy by calculating a near-optimal value for the boundary layer.

5.5 Experimental study

The comparative study used experimental results from a lithium-ion battery cell for validation. The experimental setup and the comparative results are provided in this section.

5.5.1 Experimental setup

The experimental setup consists of Scienlab battery test bench, thermal chamber and a computer for data logging and control. A prismatic high-power battery cell suitable for PHEVs, HEV, and EV is used to gather the parameterization and validation data. The test bench voltage accuracy is $\pm$ 0.05% ($\simeq \pm$ 1mV) of the measured value, the current accuracy is $\pm$ 0.05% ($\simeq \pm$ 20mA) of the measured value. During testing, the cells are placed in a 25°C thermal chamber. The integrated current of the test bench is considered to be the actual SOC; this is due to the accuracy of the current sensor and the relatively high frequency of the sampling time (=100ms).

The battery cycler used for testing has 12 channels; four different test sequences were tested on 12 cells (one cell per channel). Three cells of the same type were subjected to the same current profile under the same conditions. The output of the three cells was averaged to account for any cell manufacturing variations. The test sequence is presented in Table 5.2 and shown in Figure 5.4.

Test	Procedure	Figure
1	Capacity test + OCV-SOC test	Figure 5.4-a
2	Capacity test + Parameterization test	Figure 5.4-b
3	Capacity test + Validation test (1)	Figure 5.4-c
4	Capacity test + Validation test (2)	Figure 5.4-d

Table 5.3: Battery test sequence.

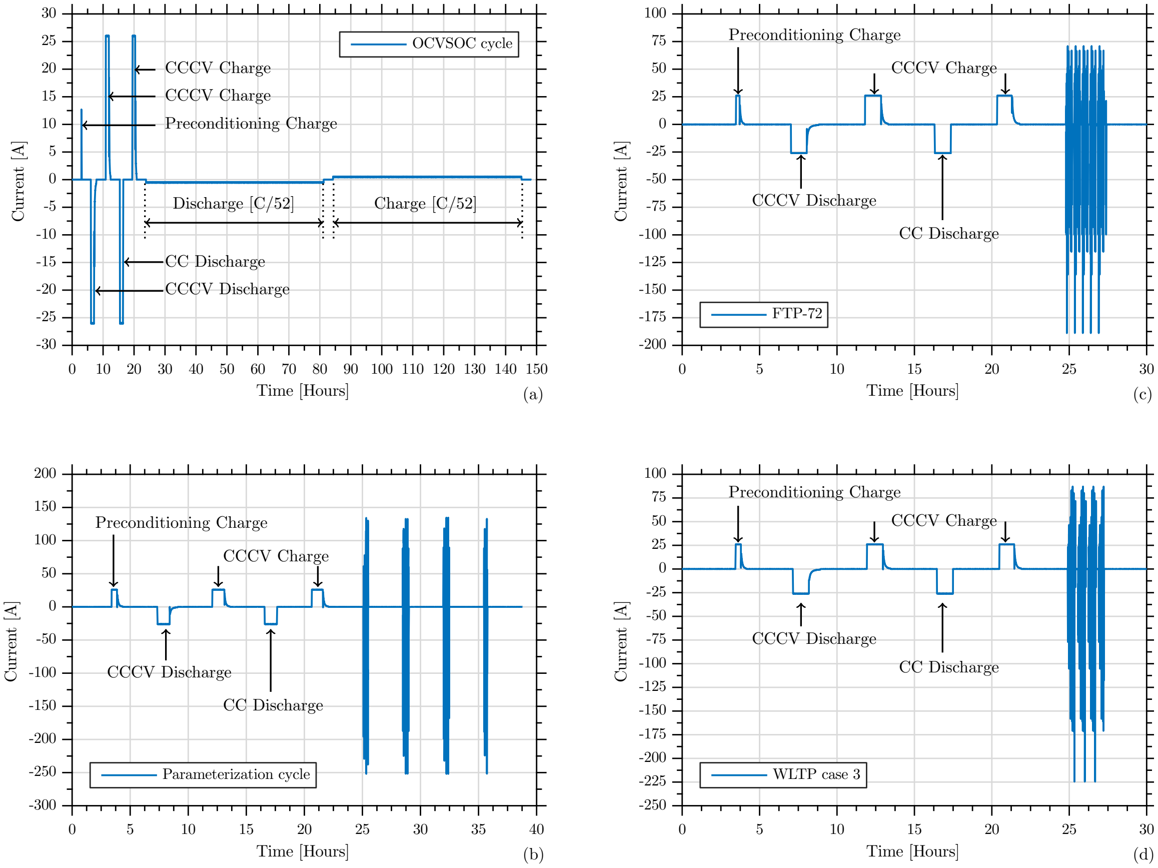

Figure 5.4: Battery test sequence: (a) OCVSOC cycle, (b) Parameterization cycle, (c) FTP-72, (d) WLTP-case 3

5.5.2 Capacity test

At the beginning of each test, the cells are left at rest at a prescribed temperature inside the temperature chamber in order to achieve homogeneous temperature distribution inside the cell. After 3 hours, the cells undergo a preconditioning charging cycle to get fully charged. After a 3 hours rest period, a standard constant-current constant voltage (CCCV) charge and discharge is performed to cycle the cells. A capacity test is then performed which consist of a 1C constant-current discharge until the battery reaches the manufacturer's discharge voltage limit. The quantity of charge in Ampere hours removed from the cell is considered as the nominal capacity C_n of the cell and is used for the SOC calculation.

5.5.3 OCV-SOC test

The OCV-SOC tests are used to characterize the nonlinear relationship between the open-circuit voltage and the state of charge. The test begins with a standard capacity test followed by a CCCV charge in order to fully charge the cell as shown in Figure 5.4-a. After 3 hours, the cells undergo a constant discharge at a very low current (C/52) followed by a rest period of 3 hours and then a constant charge at the same C-rate. The low current is necessary to minimize the internal dynamics of the cell and the ohmic loss effects due to the internal resistances of the battery. After the completion of the test, the extracted data for charging and discharging are averaged and fit to a sixth order polynomial to describe the average OCV-SOC relationship as follows:

$$OCV = a_6 SOC^6 + a_5 SOC^5 + ...a_0 \tag{5.88}$$

Figure 5.5-a shows the OCV versus SOC curve during charging and discharging. Figure 5.5-b shows the hysteresis phenomena. In this publication, the hysteresis will be ignored due to its small value and to simplify the model complexity.

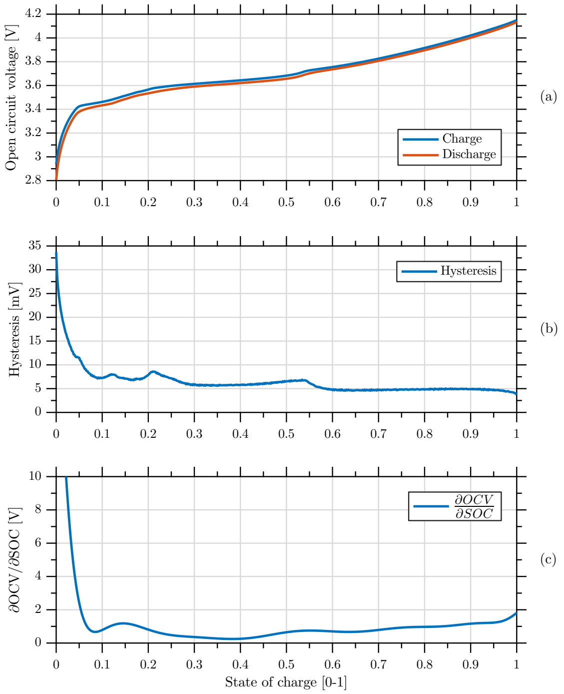

Figure 5.5: (a) Relationship between the OCV and the SOC, (b) Hysteresis level, (c) Change in the OCV with respect to the change in SOC

5.5.4 Parameterization test

The objective of this test is to allow the identification of the cell parameters associated with the battery transient response. The test begins with a standard capacity test followed by a CCCV charge in order to fully charge the cell as shown in Figure 5.4-b. After a rest period of 3 hours, the parameterization current profile is applied to discharge the cell until the battery is fully discharged. A rest period is introduced within the discharge profile to allow for temperature relaxation. The parameterization cycle contains a charge, charge-sustaining, and charge-depleting phases as shown in Figure 5.6-a. The frequency of the cycle simplifies the identification of the cell parameters, as illustrated in Figure 5.6-b.

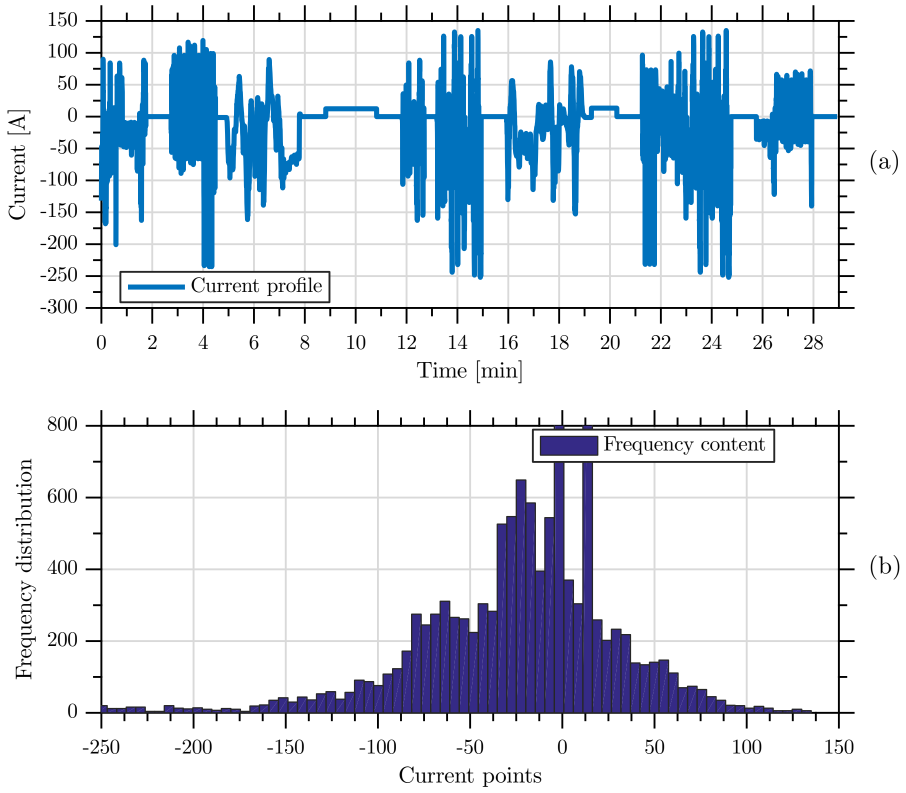

Figure 5.6: Parameterization cycle (a) Current profile, (b) Frequency distribution of the current profile

5.5.5 Validation tests

In this publication, two validation data sets are used to demonstrate the effectiveness of the preceding methodology. Both data sets are different from those utilized for the purpose of parameter identification. The two validation data sets are the US Federal Test Procedure (FTP-72) cycle shown in Figure 5.4-c, and the Worldwide Harmonized Light Vehicles Test Procedure (WLTP) - Case 3 illustrated in figure 5.4-d. Case 3 stands for high-power vehicles with Power to Weight ratio (Pwr) > 34. Both tests begin with a standard capacity test followed by a CCCV charge in order to fully charge the cell as shown in Figure 5.4-c and Figure 5.4-d. After a rest period of 3 hours, the validation current profiles are applied to discharge the cell until the battery is fully discharged.

5.6 Model performance comparisons

This section presents a comparative study of the three models discussed in section 5.3 with respect to their terminal voltage prediction accuracy, parameterization efforts, and computational complexity.

5.6.1 Comparison criteria

Terminal voltage accuracy: This criterion measures the terminal voltage accuracy of the three models during the parameterization and validation cycles. The two error indicator matrices are the RMSE and MAE.

$$RMSE = \sqrt{\frac{\sum_{t=1}^{n}\left(V_t - \widehat{V}_t\right)_t^2}{n}} \tag{5.89}$$

$$MAE = \frac{1}{n}\sum_{t=1}^{n}\left|\left(V_t - \widehat{V}_t\right)_t\right| \tag{5.90}$$

Figures 5.7, Figure 5.8, and Figure 5.9 present a comparison of the models under the parameterization cycle and two different validation cycles. The gray lines represent the experimental measurements, while the green lines, red lines, and blue lines represent the ESC, 2RC, and the SPM models, respectively.

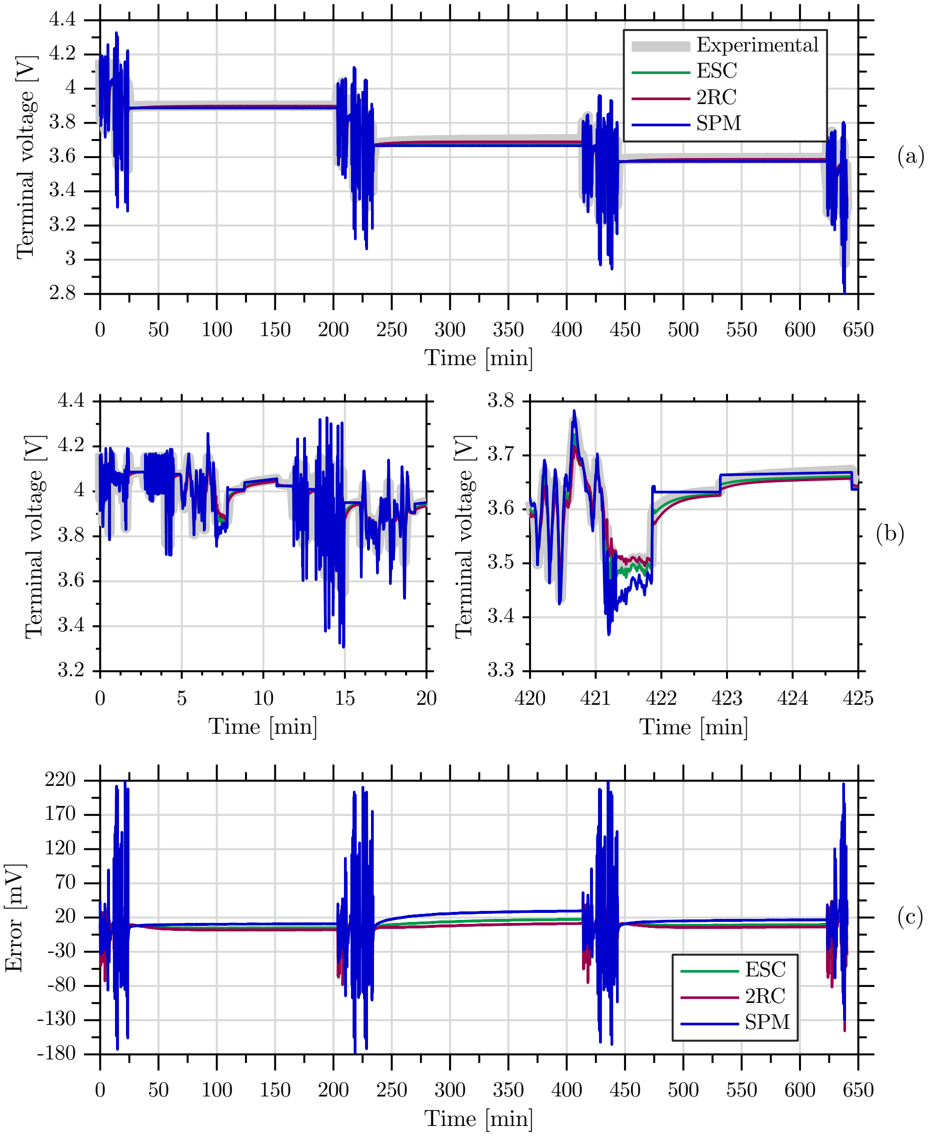

Figure 5.7: Parameterization Cycle, (a,b) Voltage response, (c) Voltage error.

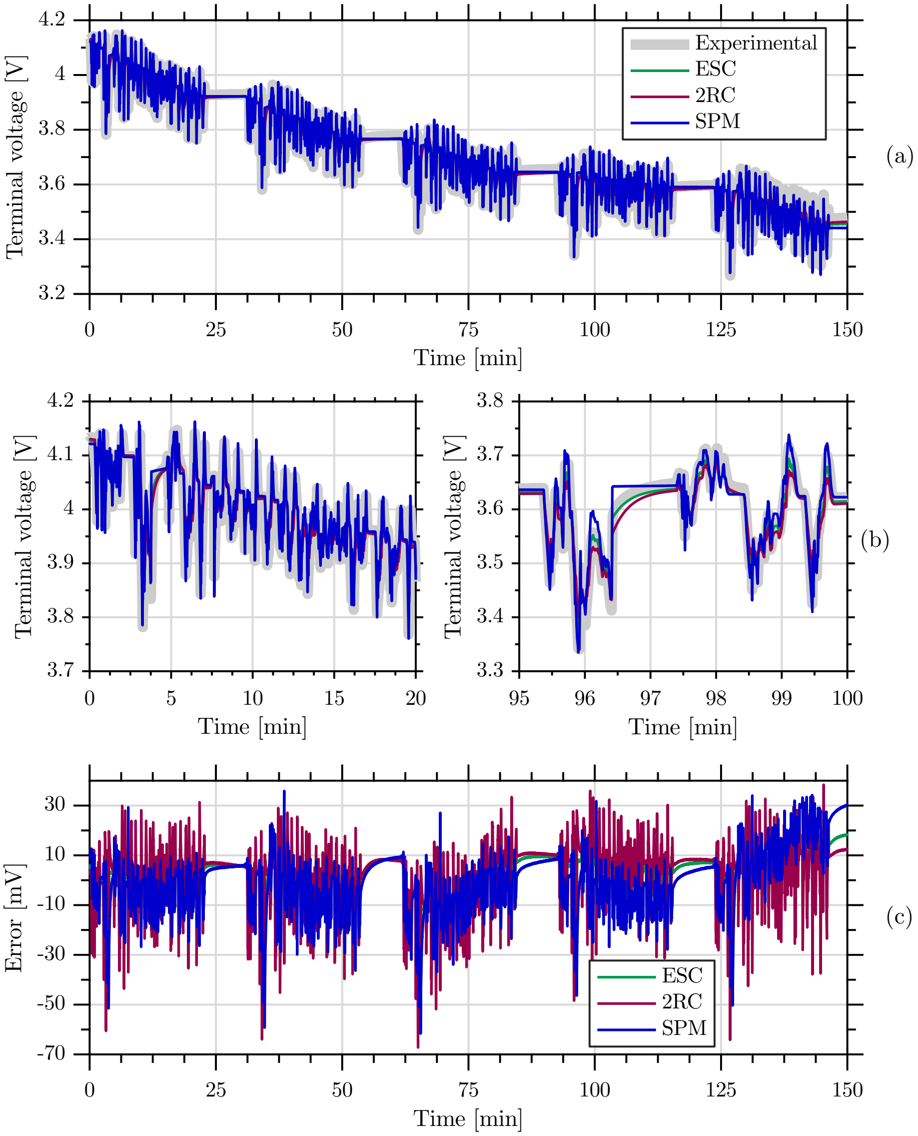

Figure 5.8: Validation Cycle - FTP 72, (a,b) Voltage response, (c) Voltage error.

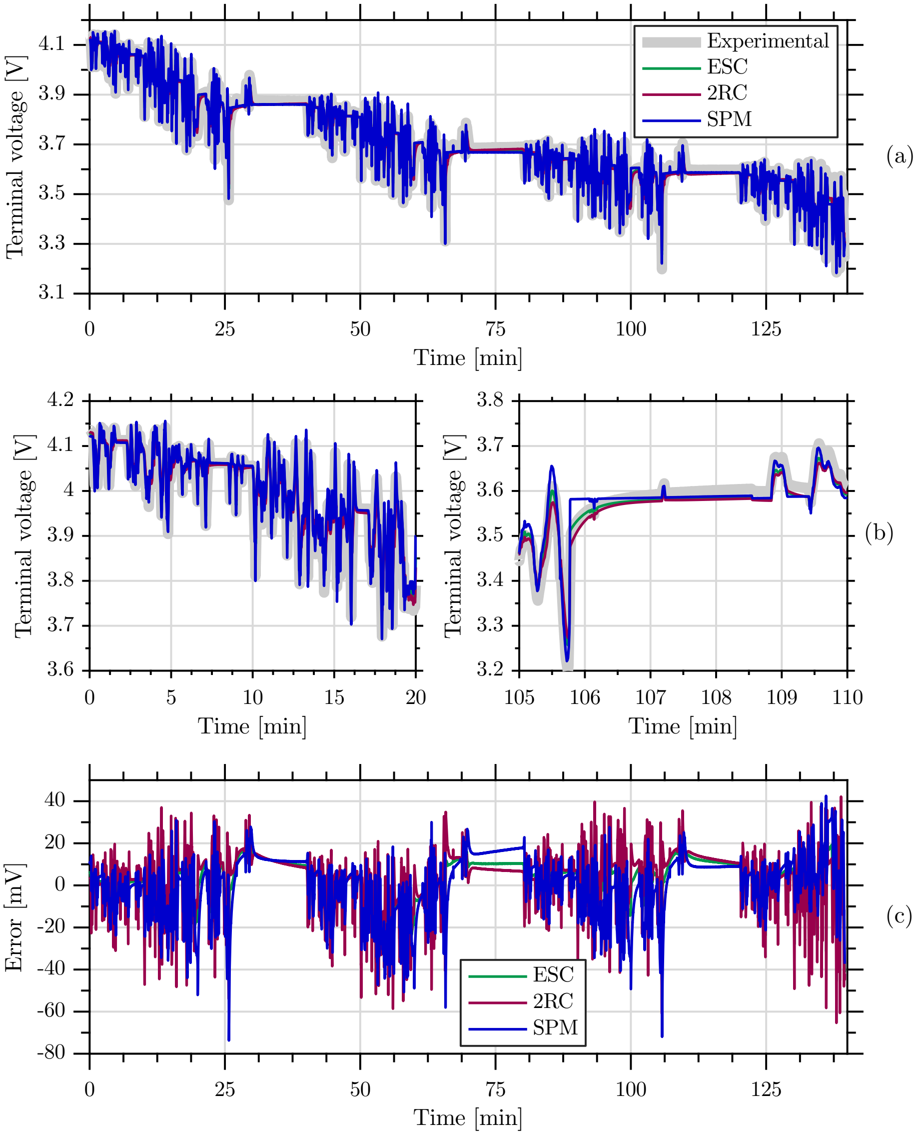

Figure 5.9: Validation Cycle - WLTP case 3, (a,b) Voltage response, (c) Voltage error.

Figure 5.7-c, Figure 5.8-c, and Figure 5.9-c present the error between the experimental voltage and each model voltage. Table 5.3 compares the terminal voltage RMSE and the MAE for the three models.

Terminal voltage accuracy [V]	ESC		2RC		SPM	
	RSME	MAE	RSME	MAE	RSME	MAE
Parameterization cycle	0.013	0.012	0.011	0.009	0.027	0.022
Validation cycle - FTP72	0.014	0.012	0.012	0.01	0.017	0.013
Validation cycle - WLTP	0.017	0.013	0.013	0.011	0.017	0.014
Mean	0.014	0.012	0.012	0.01	0.020	0.017

Table 5.4: Comparison of the models' terminal voltage accuracy

Parameterization efforts: This criterion compares the three models based on the number of parameters to be identified for each model. The ESC model parameteric vector has five parameters as presented in Equation (5.4). The 2RC model has 6 parameters as described in Equation (5.10), and the SPM model has 10 parameters as shown in Equation (5.33).

Parameterization effort	ESC	2RC	SPM
Number of parameters	5	6	10

Table 5.5: Comparison of the models' number of parameters to be identified

Complexity analysis: This criterion shows the computational complexity of the models. The computational complexity is measured as the mean of the CPU running time during the parameterization and validation cycle. In this publication, the CPU times were calculated using a 2.30 GHz Intel processor with 16 GB RAM.

CPU time [sec]	ESC	2RC	SPM
Parameterization cycle	3.24	2.70	4.27
Validation cycle - FTP72	0.87	0.70	1.10
Validation cycle - WLTP	0.70	0.62	0.99
Mean	1.60	1.34	2.12

Table 5.6: Comparison of the models' CPU time [sec]

5.6.2 Results and discussion

A quantitative comparison of results is presented in Figure 5.10. The second order equivalent circuit model (2RC) has the highest accuracy in predicting the battery terminal voltage, the lowest CPU time, and comes second in the number of parameters to be identified. The single particle electrochemical model (SPM) has the lowest accuracy in estimating the terminal voltage. This loss in accuracy compared to the full order model is due to the simplifications and the assumptions required to reduce the model computational complexity. The enhanced-self correcting model (ESC) has the lowest number of parameters to be identified, the second best voltage prediction accuracy and CPU time.

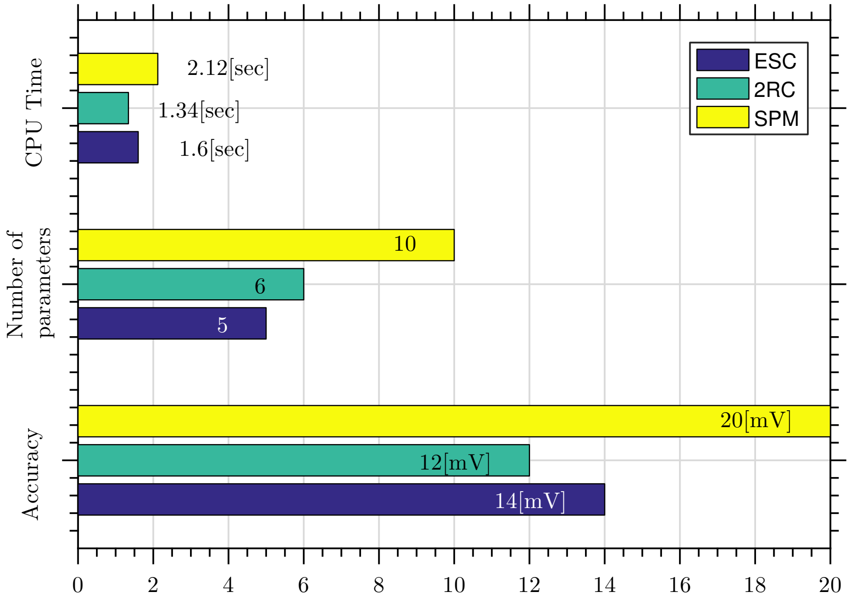

Figure 5.10: Comparison between the three models with respect to terminal voltage accuracy, number of parameters, and CPU time.

5.7 Comparative study of SOC Estimation Strategies

This section presents a comparative study between four non-linear SOC estimation strategies with respect to their rate of convergence, robustness, computational complexity, tuning complexity, and SOC estimation accuracy. As shown in Figure 5.10, the second order equivalent circuit model has the highest accuracy, lowest computational complexity, and the second lowest number of parameters when compared with the other two models. The four SOC estimation techniques will be applied to the second-order equivalent circuit model.

5.7.1 Comparison criteria

Convergence time: This criterion evaluates the time required by each filter to converge the SOC estimate to a 2% error band under different initial SOC errors. The error is calculated as the difference between the measured SOC and the estimated SOC. The quantitative results of the convergence time in presented in Table 5.7. Figure 5.11 shows the speed of convergence of the estimated SOC and the estimated terminal voltage, under four different initialization errors [5%, 10%, 20%, 30%].

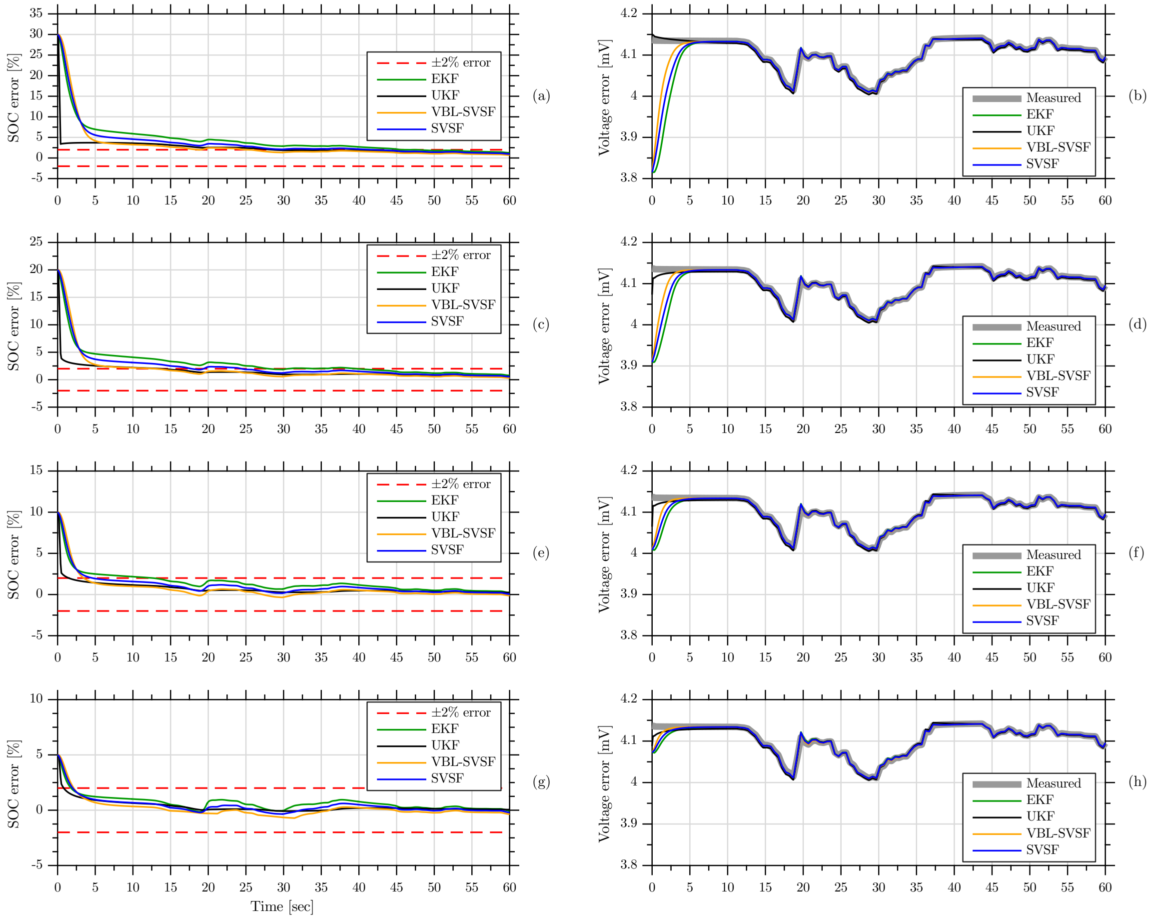

Figure 5.11: Comparison between the speed of convergence the estimated SOC and voltage under different initialization errors (a,c,e,g) SOC estimate, (b,d,f,h) voltage estimate.

Initial SOC error	SOC Convergence time [sec]				Figure
	EKF	SVSF	VBL-SVSF	UKF	
30%	45	25	25	25	Figure 5.11-a
20%	30	15	10	10	Figure 5.11-c
10%	10	5	<5	<5	Figure 5.11-e
5%	<5	<5	<5	<5	Figure 5.11-f

Table 5.7: Comparison between the convergence time of the SOC estimate under different initialization errors.

Robustness test: This criterion evaluates the SOC estimation robustness against modeling and measurement uncertainties. The modeling uncertainties resemble the model's parametric variation due to temperature and aging effects, while the measurement uncertainties resemble sensor errors due to operating in a harsh environment or sensor aging. In order to mimic the modeling uncertainties a percentage error is added to the model nominal capacitance and resistance as described in Table 5.8.

Parameter	Introduced modeling uncertainties
C_n	±20%
R_s	±20%
R_1	±20%
R_2	±20%
C_1	±20%
C_2	±20%

Table 5.8: The added modeling uncertainties to the model parameters in percentage.

The measurement uncertainty is introduced as a white Gaussian noise with mean of 1% percent error of the terminal voltage and has a variance of 1. Figure 5.12 shows the comparison results of the described robustness test for the four estimation methods for estimated SOC and estimated terminal voltage. Also, Table 5.9 tabulates the comparison between the RMSE in the estimated voltage and the estimated SOC during the robustness test under different SOC initialization errors.

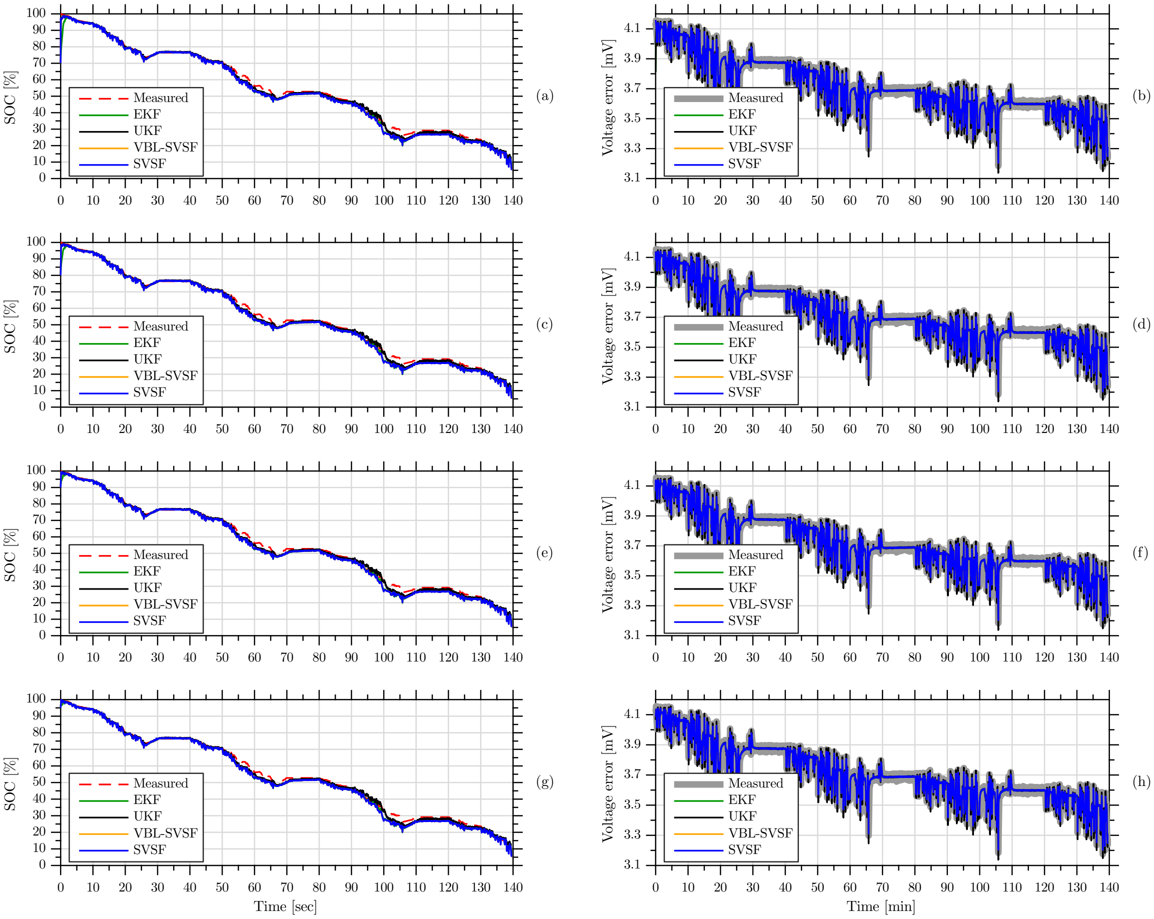

Figure 5.12: Comparison between the robustness of the estimated SOC and estimated voltage under modeling and measurement uncertainties (a,c,e,g) SOC estimate, (b,d,f,h) voltage estimate

Terminal Voltage RMSE [mV]	Filters				Figure
	EKF	SVSF	VBL-SVSF	UKF	
30%	7.14	5.69	5.58	4.86	Figure 5.12-b
20%	6.72	5.69	5.56	4.24	Figure 5.12-d
10%	6.44	4.87	4.74	4.19	Figure 5.12-f
5%	6.35	4.76	4.72	4.09	Figure 5.12-h
SOC RMSE [%]	Filters				Figure
	EKF	SVSF	VBL-SVSF	UKF	
30%	2.59	2.29	2.27	1.6	Figure 5.12-a
20%	2.38	2.28	2.26	1.56	Figure 5.12-c
10%	2.26	2.26	2.24	1.54	Figure 5.12-e
5%	2.24	2.25	2.22	1.53	Figure 5.12-g

Table 5.9: Comparison between the RMSE in the estimated voltage and the estimated SOC during the robustness test under different initialization errors.

Computational complexity analysis: This criterion presents the computational complexity of the filters. The computational cost of EKF, VBL-SVSF, and UKF are of order $O(n^3)$, while the SVSF is of order $O(n^2)$.

Tuning complexity: This criterion compares the four filters based on the number of tuning parameters. Table 5.10 shows the number of parameters of each filter. The UKF has the highest number of parameters whereas SVSF, VBL-SVSF, EKF have the same number of parameters.

Filter	EKF	SVSF	VBL-SVSF	UKF
Number of tuning parameters	4	4	4	7

Table 5.10: Comparison of the number of parameters to be tuned for each filter.

The tuning parameters used in this publication for the four filters are presented in Equations (5.91), (5.92), (5.93), and (5.94).

$$Q^{EKF} = \begin{bmatrix} 1.56e-2 & 0 & 0 \\ 0 & 1.00e-6 & 0 \\ 0 & 0 & 7.82e-3 \end{bmatrix} \quad , \quad R^{EKF} = 0.9 \tag{5.91}$$

$$\psi^{SVSF} = \begin{bmatrix} 0.91 \\ 0.34 \\ 0.15 \end{bmatrix} \quad , \quad \gamma^{SVSF} = 0.4 \tag{5.92}$$

$$Q^{VBL-SVSF} = \begin{bmatrix} 1.84e-2 & 0 & 0 \\ 0 & 1.00e-6 & 0 \\ 0 & 0 & 7.66e-3 \end{bmatrix} \quad , \quad R^{VBL-SVSF} = 0.87 \tag{5.93}$$

$$\begin{aligned} Q^{UKF} &= \begin{bmatrix} 1.86e-3 & 0 & 0 \\ 0 & 2.65e-5 & 0 \\ 0 & 0 & 2.08e-3 \end{bmatrix} \quad , \quad R^{UKF} = 4.8e-5 \\ \alpha^{UKF} &= 6.07e-1 \quad , \quad \beta^{UKF} = 1.2 \quad , \quad \kappa^{UKF} = 0 \end{aligned} \tag{5.94}$$

Performance test: This criterion compares the four different SOC estimation strategies under normal operating conditions. To represent the normal operation condition, the initialization error in the SOC error is set to 5%, and the errors of model parameters are set to ± 2%.

Performance test	Filters				Figure
	EKF	SVSF	VBL-SVSF	UKF	
Terminal Voltage RMSE [mV]	8.20	8.48	8.18	8.09	Figure 5.13-a
SOC RMSE [%]	2.26	2.23	2.23	1.53	Figure 5.13-b

Table 5.11: Comparison between the RMSE in the estimated voltage and SOC during the performance test.

Table 5.11 show the comparison results between the RMSE in the estimated voltage and estimated SOC during the performance test. Figure 5.13 demonstrates the performance of the filter in predicting the SOC and the terminal voltage.

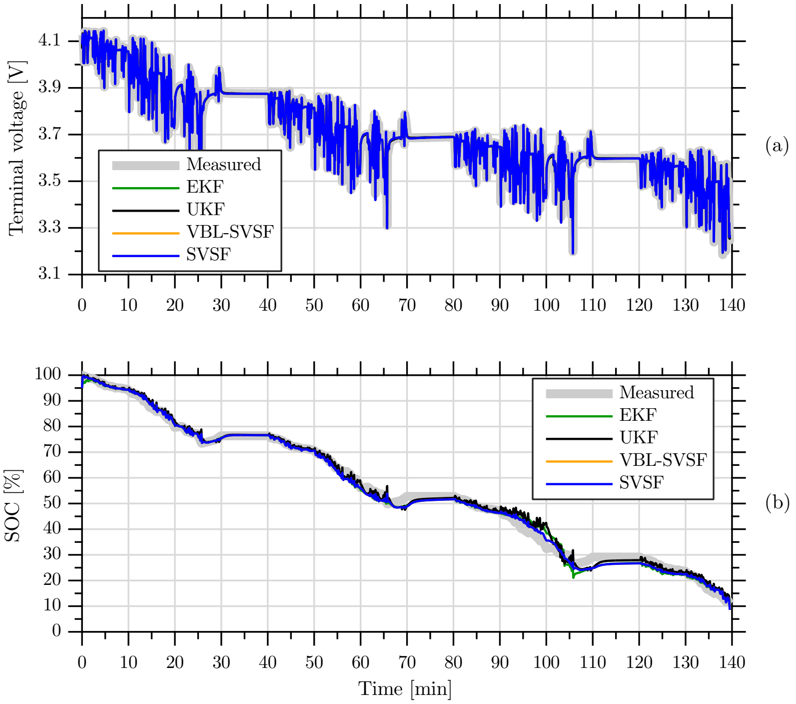

Figure 5.13: Comparison between different filters' estimated SOC and voltage under normal conditions (a) voltage, (b) SOC.

5.7.2 Results and discussion

In order to have a comprehensive comparative study of the nonlinear estimators of interest, five comparison criteria are considered and described, that include convergence time, robustness against modeling and measurement uncertainties, computational complexity, tuning complexity, and normal condition performance. The results indicate, as expected that each of the estimators has its own advantages and disadvantages.

Convergence rate criteria examine the performance of the estimators in the presence of different initial condition errors in the SOC. With respect to this criterion, both the UKF and VBL-SVSF outperform the SVSF and the EKF. The VBL-SVSF and the SVSF are designed to inherently be robust against uncertainties, which enables them to recover from initialization error and converge the estimated value to the true values.

The robustness test is designed to resemble the uncertainties that a battery system normally encounters in a real world operation. These include modeling uncertainties due to temperature and aging effects and measurement uncertainties due to the sensor operating in harsh conditions and sensor aging. Furthermore, to provide even more challenging tests, the estimators are also tested under the combination of robustness criteria and different SOC initialization errors. Under this latter test, for terminal voltage estimation error, the UKF outperforms the SVSF by about 10% to 15%, the VBL-SVSF by about 5% to 10% and it also outperforms the EKF by about 50% to 60%. The UKF algorithm in comparison to the EKF tolerates nonlinearities of a higher order. For SOC estimation under this test, the UKF outperforms the three other filters.

The main drawback of the UKF is its computational and tuning complexity. This, for real world applications in the vehicles, is a major hindrance which may dramatically increase the costs related to computational resources and even eliminate the UKF as an option. On the other hand, the SVSF has the least of computational burdens and outperforms the EKF in all tests.

The normal condition performance test tries to capture a reasonable working condition where the uncertainties are within a limited bound. In general, the EKF has the least favorable performance. Although the UKF outperforms the VBL-SVSF and the SVSF, the performance of the three filters are reasonably acceptable. Figure 5.14 summarizes the results for all comparative study tests.

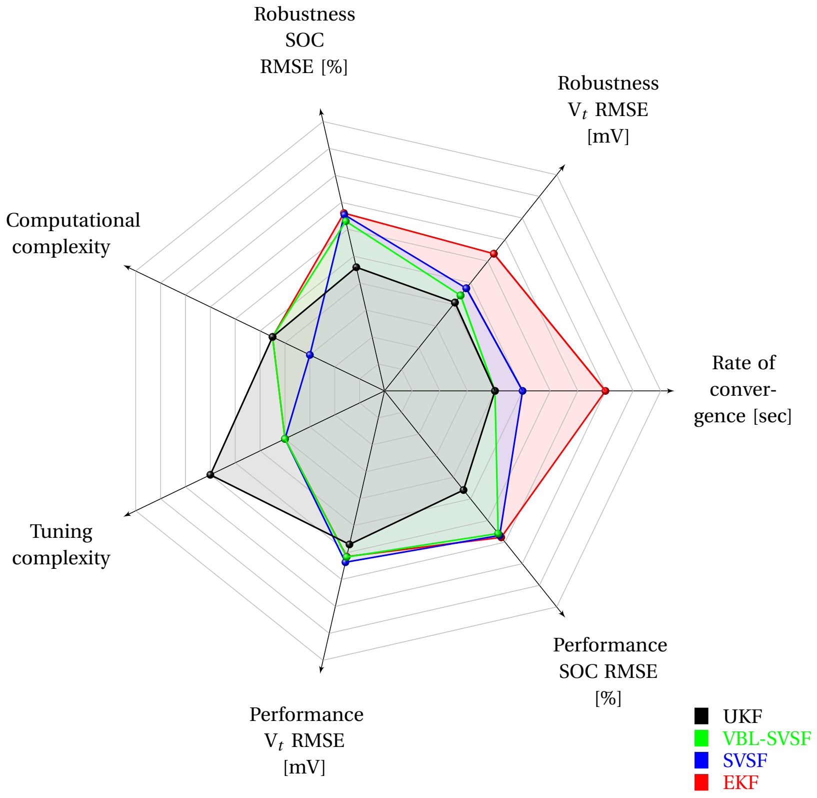

Figure 5.14: Comparison between different SOC estimation strategies

5.8 Conclusion

For electrical vehicles, BMS plays an important role to fully utilize the energy storage system's potential within its physical limitations. First, this study has quantitatively reviewed three of the most common models used in Li-ion electric storage systems. Three models representing three main battery modeling categories, i.e., equivalent circuit models, behavioral models, and electrochemical models, were considered. The three models were parameterized and validated under real driving conditions. The accuracy of the models was validated through comparison with experimental data under the real-time driving profiles FTP-72 and WLTP case-3. The merits for the modeling comparison were the terminal voltage prediction accuracy in terms of its RMSE and MAE, parameterization efforts, and computational complexity. The results demonstrated that the second order equivalent circuit model (2RC) provides the most favorable trade of between computational complexity and estimation accuracy. It is, therefore, the preferred model for real-time implementation in battery management systems.

Four model-based nonlinear state of charge estimation strategies were used to estimate the state of charge of the battery using the second order equivalent circuit model (2RC). The EKF, SVSF, VBL-SVSF; and UKF are compared with respect to their rate of convergence, robustness to modeling and measurement uncertainties, computational complexity, tuning complexity in terms of the number of tuning parameters, and SOC estimation accuracy using the RMSE and the MAE measures. The results indicate that the UKF and the VBL-SVSF outperform the SVSF and the EKF in the rate of convergence rate, robustness to uncertainties, and normal operation performance tests. In general, the UKF and the VBL-SVSF have comparable results in the tests as mentioned earlier, though UKF slightly outperforms the VBL-SVSF. The UKF design, in comparison to the EKF design, is more tolerant to nonlinearities and can handle uncertainties of that sort. Also, the VBL-SVSF and the SVSF algorithms benefit from an inherently stable design that provides them with robustness against uncertainties. The main drawback of the UKF is in the computational and tuning complexity tests that limit its applicability, particularly in electric vehicle applications. In contrast, the SVSF has the least computational burden among the four estimators under study. Future work will focus on incorporating a state of health and core temperature estimation strategies, along with parameterization and validation under different aging conditions.

Nomenclature

Symbol	**Description**	**Unit**
Acronyms		
$\mathbf{A}$	State matrix in linear state model state equation	–
$\mathbf{B}$	Input matrix in linear state model state equation	–
$\mathbf{C}$	State matrix in linear state model output equation	–
$\mathbf{D}$	Input matrix in linear state model output equation	–
$\mathcal{O}$	Observability matrix	–
F	Linearized state model state equation	–
H	Linearized state model output equation	–
P	The a posteriori error covariance matrix	–
z_k	The experimental measurement	–
$R_s^{n,p}$	Solid active material particle radius	cm
R_f	Film resistance on the electrodes surface	Ωcm^2
A	Electrode plate Area	cm^2
t_0^+	Transference number of lithium ion	–
c	Concentration of lithium ions	mol cm^{-3}
D	Diffusion coefficient of lithium species	$cm^2 s^{-1}$
q	Discretization step	–
R	Universal gas constant (R = 8.3143)	J $mol^{-1}K^{-1}$
F	Farady's Constant (F = 96,487)	C mol^{-1}
T	Absolute Temperature	K
a_s	Active surface area per electrode unit volume	cm^2cm^{-3}
I	Applied current	A
r	Radial coordinate	cm
t	Time	s
x	Cartesian coordinate	s
j^{li}	Butler-Volmer current density	A cm^{-3}
R^+, R^-	Internal Resistance of the cell	A cm^{-3}

Greek Symbols		
ε_s	Active material volume fraction	$-$
ε_e	Electrolyte phase volume fraction	$-$
σ	Conductivity of solid active material	$\Omega^{-1}cm^{-1}$
κ	Electrolyte phase ionic conductivity	$\Omega^{-1}cm^{-1}$
κ_D	Electrolyte phase diffusion conductivity	$\Omega^{-1}cm^{-1}$
θ	Reference stoichiometry	$-$
α_a, α_c	Anodic and cathodic charge transfer coefficients	$-$
α_1, α_2	The poles of the low pass filter	$-$
η	Surface overpotential of an electrode reaction	V
ϕ	Volume averaged electrical potential	V
δ	Thickness	cm

Superscripts		
eff	Effective	$-$
p	Cathode	$-$
n	Anode	$-$
sep	Separator	$-$

Subscripts		
e	Electrolyte phase	$-$
s	Solid phase	$-$

Chapter 6

Li-ion battery state of charge estimation using one state hysteresis model with non-linear estimation strategies [1]

6.1 INTRODUCTION

In the last ten years, battery management systems (BMS) have garnered lots of attention from many researchers. Accurate BMS increases the life of a battery and reduces fast aging-effects, thermal runaways, and performance ceasing. It is, therefore,

---

[1] Mohammed Farag, Mina Attari, Andrew Gadesden, Saeid Habibi
Li-ion battery state of charge estimation using one state hysteresis model with non-linear estimation strategies
Accepted by the International Journal of Chemical, Molecular, Nuclear, Materials and Metallurgical Engineering.
http://waset.org/publications/10006626

vital and fundamental for the BMS to accurately predict and estimate the SOC, among other critical parameters. Several methods have been implemented for SOC estimation; starting from very abstract models dealing with batteries as a black-box, to very detailed electrochemical models which are used to capture the battery internal physical behavior [1].

The most popular battery chemistery in use today is the lithium-ion batteries [106, 107, 108]. Li-Ion batteries are often found in portable electronic devices due to their lightweight and ability to recharge relatively well. During operation, the BMS estimate parameters that affect the battery packs and their operating conditions [7, 8, 9]. A number of excellent surveys have been performed on BMS modeling and estimation [10, 14, 109, 110]. Parameters of interest include terminal voltage (typically measured), battery state of charge (SOC), state of health (SOH), power and capacity fade, and instantaneous power. These parameters must be estimated using a filtering strategy such as the Extended Kalman filter (EKF).

In section 6.2, the EKF, SVSF, and VBL-SVSF filtering methods are briefly described. Section 3 provides an overview of the one state hysteresis (OSH) model. In section 4, three nonlinear estimation strategies are applied on the OSH battery model and compared. The paper then concludes in the final section.

6.2 Estimation strategies

This section provides an overview of the three nonlinear estimation strategies used in this paper.

6.2.1 Extended Kalman Filter

Rudolph Kalman introduced the Kalman filter (KF) in the 1960s. Since then, KF has been one of the most commonly used state and parameter estimation strategies. KF strategies calculate a statistically optimal gain to correct predicted the system state estimates [111]. For Kalman filter to be optimal many strict assumptions must be followed, such as the system and measurements functions must be linear and known, and the noise must be white and Gaussian-distributed [112].

Many variations for Kalman filter have been introduced. Andrews et al. [99] formulated the extended Kalman filter (EKF) for the case of nonlinear systems and measurements. The EKF method uses the first-order Taylor series approximations to linearize the nonlinearities about the operating point. The EKF equations are similar to the KF, except for the linearization. The prediction phase of the EKF begins as follows [99]:

$$\hat{x}_{k+1|k} = f\left(\hat{x}_{k|k}, u_k\right) \tag{6.1}$$

$$P_{k+1|k} = F_k P_{k|k} F_k^T + Q_k \tag{6.2}$$

Note that the update phase is defined by the following set of equations [99]:

$$e_{z,k+1|k} = z_{k+1} - h\left(\hat{x}_{k+1|k}\right) \tag{6.3}$$

$$S_{k+1} = H_{k+1} P_{k+1|k} H_{k+1}^T + R_{k+1} \tag{6.4}$$

$$K_{k+1} = P_{k+1|k} H_{k+1}^T S_{k+1}^{-1} \tag{6.5}$$

$$\hat{x}_{k+1|k+1} = \hat{x}_{k+1|k} + K_{k+1} e_{z,k+1|k} \tag{6.6}$$

$$P_{k+1|k+1} = \left(I - K_{k+1} H_{k+1}\right) P_{k+1|k} \tag{6.7}$$

The first-order Taylor series approximation is used to linearize the non-linear state and measurement equations as follows :

$$F_k = \left.\frac{\partial f\left(x\right)}{\partial x}\right|_{x=\hat{x}_{k|k},u_k} \tag{6.8}$$

$$H_{k+1} = \left.\frac{\partial h\left(x\right)}{\partial x}\right|_{x=\hat{x}_{k+1|k}} \tag{6.9}$$

For a complete list of the nomenclature and the corresponding definitions, please refer to the Appendix.

6.2.2 Smooth Variable Structure Filter - SVSF

Saeid Habibi introduced the smooth variable structure filter (SVSF) in 2007 [104]. The SVSF is a relatively new estimation strategy with respect to the KF and EKF. The SVSF uses the sliding mode concepts in calculating the correction gain. Formulaically, the SVSF is a predictor-corrector estimator; however, its gain is fundamentally different from KF gain. The theory behind the SVSF estimation process is shown in Figure 6.1.

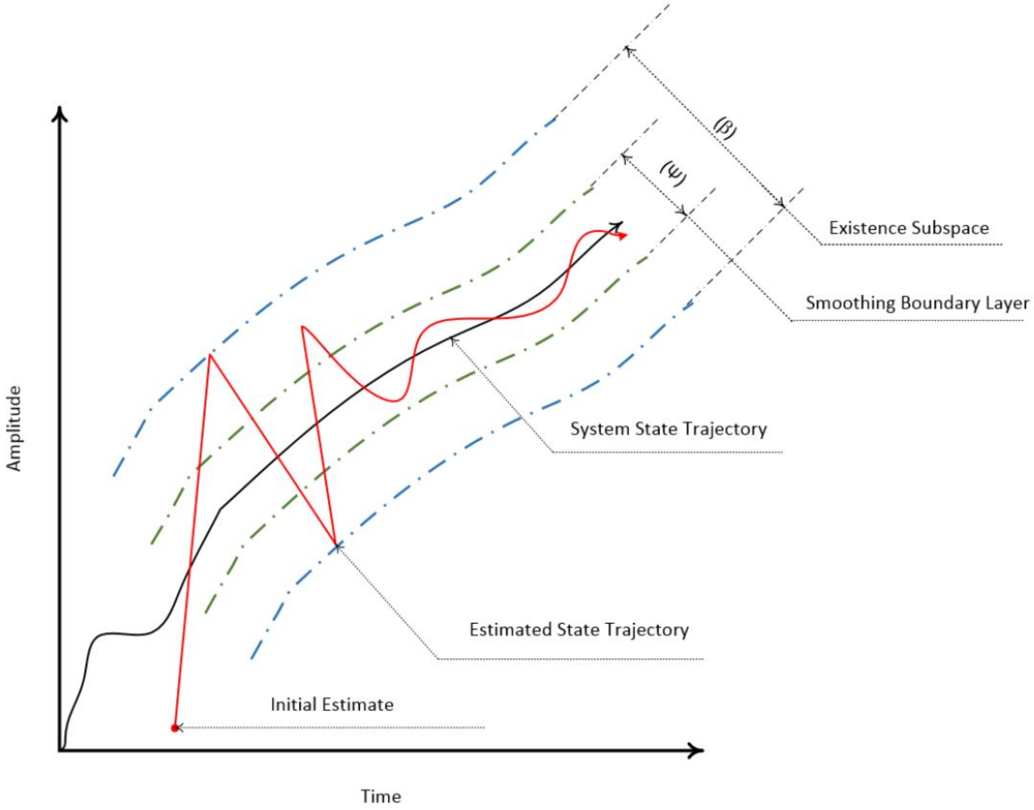

Figure 6.1: The SVSF estimation concept.

The prediction phase of the SVSF is similar to the EKF, and can be described as follows:

$$\hat{x}_{k+1|k} = f\left(\hat{x}_{k|k}, u_k\right) \tag{6.10}$$

$$P_{k+1|k} = F_k P_{k|k} F_k^T + Q_k \tag{6.11}$$

$$e_{z,k+1|k} = z_{k+1} - h\left(\hat{x}_{k+1|k}\right) \tag{6.12}$$

The SVSF gain is defined by Equation (6.13).

$$K_{k+1} = C^{+} diag\left[\left(\left|e_{z,k+1|k}\right|_{Abs} + \gamma\left|e_{z,k|k}\right|_{Abs}\right) \circ sat\left(\bar{\psi}^{-1} e_{z,k+1|k}\right)\right] diag\left(e_{z,k+1|k}\right)^{-1} \tag{6.13}$$

The update phase is defined as follows:

$$\hat{x}_{k+1|k+1} = \hat{x}_{k+1|k} + K_{k+1} e_{z,k+1|k} \tag{6.14}$$

$$P_{k+1|k+1} = \left(I - K_{k+1} H_{k+1}\right) P_{k+1|k} (I - K_{k+1} H_{k+1})^T + K_{k+1} R_{k+1} K_{k+1}^T \tag{6.15}$$

$$e_{z,k+1|k+1} = z_{k+1} - h\left(\hat{x}_{k+1|k+1}\right) \tag{6.16}$$

Note that the SVSF gain is a function of: (i) a priori measurement error, (ii) a posteriori measurement error, (iii) SVSF memory, (iv) and a smoothing boundary layer term. The smoothing boundary layer term is utilized to decrease the magnitude of chattering created by the switching term in Equation (6.13).

The existence subspace shown in Figure 6.1 represents the estimation processes' amount of uncertainties [113]. This value is defined in terms of modeling errors or measurement uncertainties, and is often tuned by trial and error based on the amount of system or measurement noise. The width of the existence subspace β is time variant and is correlcated to inaccuracy of the filter and battery model as well as the measurement model [104]. The existence subspace value is not known, however prior knowledge of the system is helpful to set an upper limit.

6.2.3 Time-Varying Smoothing Boundary Layer - VBL SVSF

Gadsden et al. [105] introduced the time-varying smoothing boundary layer formulation of the SVSF in 2012 in order to increase the estimation accuracy and avoid the chattering effect. On the one hand, The SVSF estimation accuracy is reduced by the chattering effect caused by the SVSF gain definition. On the contrary, the chattering effect drastically enhances filter robustness and stability against modeling errors and uncertainties [104].

To obtain the VBL formulation, a correlation between the partial derivative of the trace of a posteriori covariance and the smoothing boundary layer term was introduced to the filter gain derivation. The VBL-SVSF prediction phase is similar to Equation (6.10) through (6.12). The time-varying smoothing boundary layer (VBL) is calculated using the following three equations:

$$S_{k+1} = H_{k+1} P_{k+1|k} H_{k+1}^{T} + R_{k+1} \tag{6.17}$$

$$A_{k+1} = \left| e_{z,k+1|k} \right|_{Abs} + \gamma \left| e_{z,k|k} \right|_{Abs} \tag{6.18}$$

$$\psi_{k+1} = \left(\bar{A}_{k+1}^{-1} H_{k+1} P_{k+1|k} H_{k+1}^{T} S_{k+1}^{-1} \right)^{-1} \tag{6.19}$$

The VBL-SVSF gain is then used to update the state estimates and state error covariance matrix, as follows:

$$K_{k+1} = H_{k+1}^{-1} \bar{A}_{k+1} \psi_{k+1}^{-1} \tag{6.20}$$

$$\hat{x}_{k+1|k+1} = \hat{x}_{k+1|k} + K_{k+1} e_{z,k+1|k} \tag{6.21}$$

$$P_{k+1|k+1} = \left(I - K_{k+1} H_{k+1} \right) P_{k+1|k} (I - K_{k+1} H_{k+1})^{T} + K_{k+1} R_{k+1} K_{k+1}^{T} \tag{6.22}$$

$$e_{z,k+1|k+1} = z_{k+1} - h\left(\hat{x}_{k+1|k+1} \right) \tag{6.23}$$

Both VBL-SVSF and SVSF works in a predictor -corrector fashion, the main difference is the equations used to calculate the filters gain. The main drawback of the SVSF is the fact that its conservative fixed smoothing boundary layer is fixed throughout the operation. This reduces the overall estimation accuracy. The VBL-SVSF calculates a near-optimal value for the boundary layer, to improve the estimation accuracy.

6.3 One state hysteresis model

Various methods for battery modeling exist in literature. Plett et al. [8] developed the most common used behavioral models: the combined model, simple model, zero and one state hysteresis models, and enhanced self-correcting model. All of the models have the terminal voltage as an output and the SOC as a system state. The one state hysteresis (OSH) is a popular behavioral model and has been selected for use in this paper. The hysteresis phenomena is very important to increase the system performance and improve the SOC estimation accuracy [10] The description of the one state hysteresis model shown here may be found in details in [8].

In the OSH model,the terminal voltage is calculated as follows:

$$y_k = OCV\left(z_k\right) - s_k M\left(z_k\right) - R i_k \tag{6.24}$$

where s_k represents the sign of the current. For some sufficiently small and positive value ε, one has:

$$s_k = \begin{cases} +1 & i_k > \varepsilon \\ -1 & i_k < -\varepsilon \\ s_k - 1 & |i_k| \leq \varepsilon \end{cases} \tag{6.25}$$

where $M(z_k)$ is a constant value and equal to half the difference between the charge and discharge values [8]. As shown in the previous equation, the hysteresis state is not a function of time, but of SOC. The state-space representation of the OSH model is defined as follows:

$$\begin{bmatrix} h_{k+1} \\ z_{k+1} \end{bmatrix} = \begin{bmatrix} F\left(i_k\right) & 0 \\ 0 & 1 \end{bmatrix} \begin{bmatrix} h_k \\ z_k \end{bmatrix} + \begin{bmatrix} 0 & 1 - F\left(i_k\right) \\ -\frac{\eta_i \Delta t}{C} & 0 \end{bmatrix} \begin{bmatrix} i_k \\ M\left(z, \dot{z}\right) \end{bmatrix} \tag{6.26}$$

$$y_k = OCV\left(z_k\right) - Ri_k + h_k \tag{6.27}$$

Furthermore, note that $F(i_k) = exp(-|\eta_i i(t)\gamma/C_n|)$. The parameters vector for the OSH is shown in Equation (6.28) and the values for the parameters is presented in Appendix 6.6.

$$\theta = [R^+, R^-, M^+, M^-, \gamma] \tag{6.28}$$

6.4 Estimation problem and results

This section discusses the estimation problem and the results of applying the nonlinear estimation strategies for the purposes of estimating the Li-Ion state of charge.

6.4.1 Problem setup

In this paper, the simulation data was collected from AVL CRUISE software. This software is used to mimic a real-time scenario for vehicles and power-trains modeling. The vehicle simulation model was subjected to an urban dynamometer driving schedule (UDDS) cycle. The vehicle velocity profile for the UDDS cycle is shown in Figure 6.2, and the corresponding battery current profile is shown in Figure 6.3. The main parameters of interest include the terminal voltage (measurement) and the state of charge (SOC).

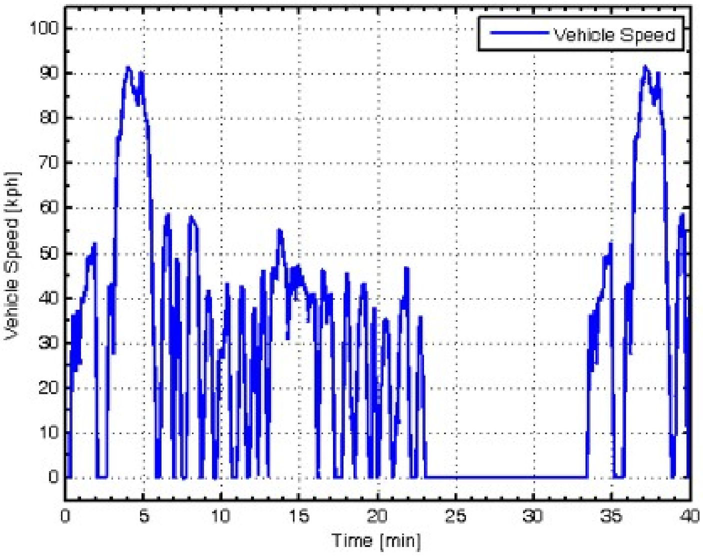

Figure 6.2: The UDDS velocity profile

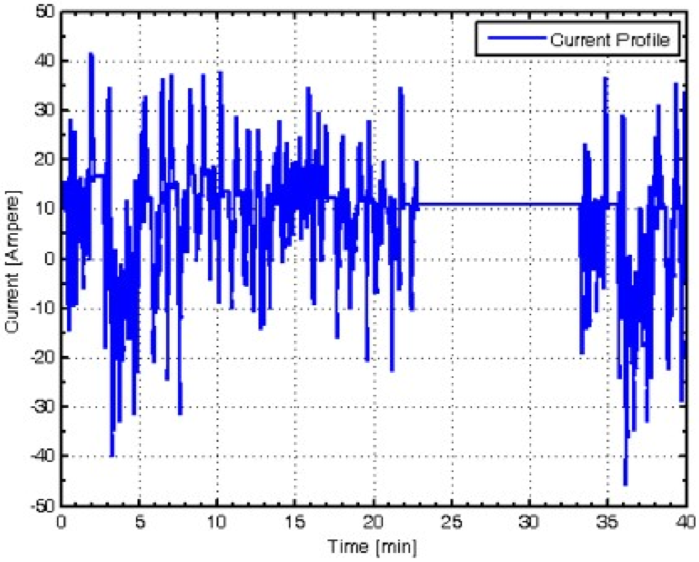

Figure 6.3: The UDDS current profile

The system and measurement noise covariance matrices used by the EKF, and VBL-SVSF for state estimation are defined as follows:

$$Q = diag\left(\left[\begin{array}{cc} 0.05 & 5 \times 10^{-3} \end{array}\right]\right) \tag{6.29}$$

$$R = 0.1 \tag{6.30}$$

The SVSF memory or forgetting factor is set as $\gamma = 0.3$, and the fixed smoothing boundary layer width are set to $\psi = 2$ for the state estimates. These values were selected based on designer knowledge of Q and R, and also by trial-and-error, in an effort to improve the estimation accuracy. Note also that the sample rate of the simulation is $\delta T = 100$ milliseconds.

6.4.2 Estimation Results

The three filters (EKF, SVSF, and VBL-SVSF) are used to estimate the state of charge for the model discussed in section 6.2.

Figure 6.4 illustrates the SOC estimation results for the three filters. The true SOC is a result of coulomb counting that is used as the basis to compare the estimation performance for the filters. As it is shown in Figure 6.4 the VBL-SVSF has the best performance when compared to other filters in estimating the SOC followed by SVSF and EKF. Particularly, the better performance is more noticeable after the idle interval between minutes 22 and 33. This improvement in SOC estimation is significant because it solves the SOC estimation accuracy problem for the battery systems of vehicles after they start from a stop or idle condition.

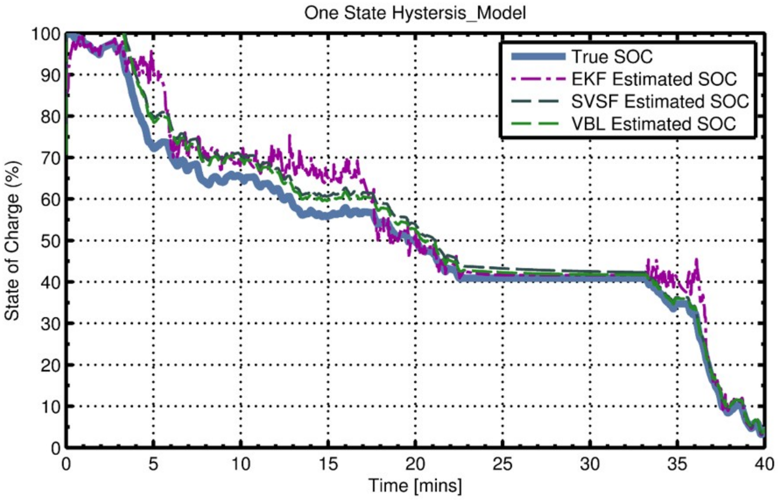

Figure 6.4: State of charge estimation using the three filters

Figure 6.5 displays the corresponding terminal voltage estimates using the three filters. All filters are capable of providing estimates of terminal voltage.

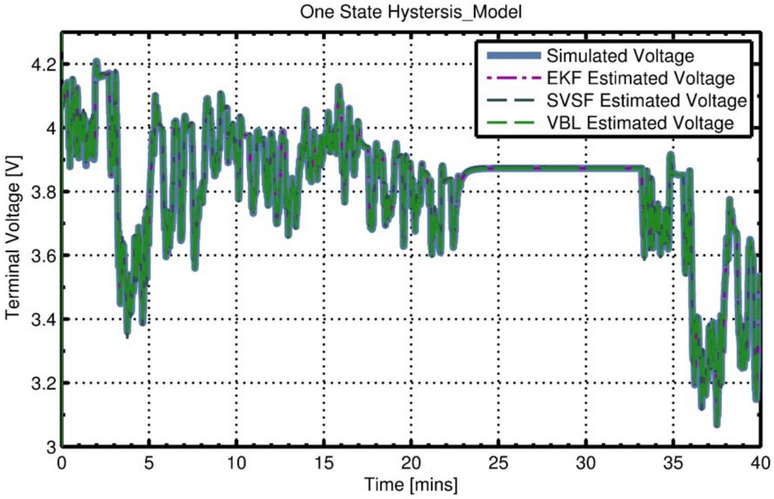

Figure 6.5: Battery terminal voltage estimation using the three filters.

For better comparison, Figure 6.6 shows the root mean squared error (RMSE) in the state of charge calculated for three estimators. The VBL-SVSF provides the best estimation accuracy followed by the SVSF and EFK. The superior performance of SVSF based estimation comes the specific design of the corrective gain in this strategy that makes it more robust to modeling uncertainties. Furthermore, VBL-SVSF inherits the robustness from SVSF and estimation accuracy from its optimal gain design.

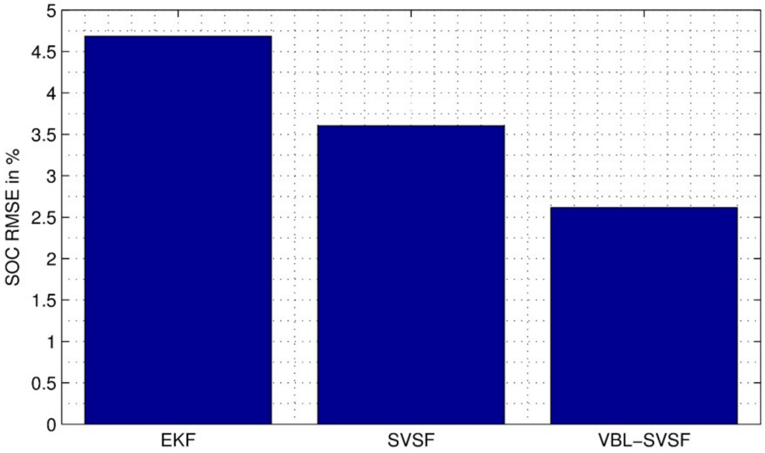

Figure 6.6: Terminal voltage RMSE using the three filters.

6.5 Conclusion

This paper presented the results of applying three nonlinear estimation strategies on a Li-Ion battery model. The one state hysteresis model was used as a standard benchmark for three filters: the extended Kalman filter (EKF), the smooth variable structure filter (SVSF), and the time-varying smoothing boundary layer formulation of the SVSF (VBL-SVSF). It was found that the VBL-SVSF yielded the best results in terms of the SOC estimation accuracy. This was to be expected based on the formulation of the gain.

Future work will involve applying additional filtering strategies, such as the unscented Kalman filter (UKF), cubature Kalman filter (CKF), and the particle filter (PF). In addition, a number of other popular battery models will be studied; such as behavioural, equivalent circuit, and electrochemical models.

6.6 Nomenclature

The following is a list of important nomenclature and parameters used throughout the paper.

Symbol	**Description**	**Unit**
Acronyms		
x	State vector or values	–
z	Measurement (system output) vector or values	–
w	System noise vector	–
v	Measurement noise vector	–
F	Linearized system transition matrix	–
H	Linearized measurement (output) matrix	–
A	SVSF error vector (or matrix)	–
K	Filter gain matrix	–
P	State error covariance matrix	–
Q	System noise covariance matrix	–
S	Innovation covariance matrix	–
e_z	Measurement (output) error vector	–
γ	SVSF memory or convergence rate	–
ψ	SVSF smoothing boundary layer	–
diag[a] or $\bar{a}$	Diagonal of some vector or matrix a	–
sat()	Saturation function	–
$\|a\|$	Absolute value of a	–
$\bar{a}$	Diagonal matrix of some vector a	–
T	Transpose of a vector	–
+	Pseudoinverse of some non-square matrix	–
$\circ$	Denotes a Schur product	–

Appendix

The following is a list of the model parameters.

Parameter	**Value**	**Unit**
R^+	0.0022	Ω
R^-	0.0018	Ω
M^-	0.0105	$-$
M^-	-0.016	$-$
γ	0.1	$-$

Chapter 7

Conclusions

This chapter provides the conclusions and recommendation for future work.

7.1 General conclusion

This dissertation presented contributions in the area of lithium-ion battery electrochemical modeling, thermal modeling, heat generation modeling, state of charge estimation, core temperature estimation, and thermal management strategies, with the focus on their real-time application in the Battery Management Systems (BMS) of hybrid and electric vehicles.

Chapter 3 presents a Continuous, Piecewise-Linear, Electrode-Average Model (CPWL-EAM). This is a new model formulation for real-time implementation within BMS and exhibits high accuracy and reduced CPU run-time compared with the reduced-order, electrode-average model (EAM). The proposed CPWL-EAM linearizes the univariate, nonlinear relation between the OCP and the cell SOC, while maintaining the continuity and smoothness of the OCP curve. The piecewise-linear regions were identified using a novel optimal knot-placement technique which uses GA to determine the optimal knot-locations, while maintaining the continuity constraints. The model is parametrized using a new technique that provides a trade-off between extensive experimental characterization techniques and purely identifying all parameters using nonlinear techniques. The accuracy of the CPWL-EAM is validated through comparisons with experimental data and the EAM under the real-time driving profiles FTP-72 and WLTP. Since the CPWL-EAM model shows accurate voltage predictions, while reducing the running time by 20%, the proposed model can be easily implemented on-board of real-time BMS.

A novel integrated combined Electrochemical, Heat Generation, and Thermal Model (ECHTM) is also one of main contributions of this research and is presented. This model is capable of maintaining terminal voltage and core temperature accuracy over a broad range of temperatures and state of charges. The temperature dependent electrochemical model considers the variations in the model parameters through Arrhenius equation. The proposed thermal model consists of lumped four thermal nodes interconnected by thermal resistances and capacitances. The heat generation model considers three sources of heat during operation (irreversible losses, reversible losses, and heat of mixing). The three models (electrochemical, heat generation, and thermal model) are coupled together in an iterative fashion to predict the cell's terminal voltage and core temperature accurately.

The electrochemical model parameters and the thermal model parameters are identified using a new technique that excites the model under isothermal and non-isothermal operating conditions, respectively. First, the electrochemical model with thermal dependent parameters is parameterized and validated under isothermal conditions at six different temperatures points [-25°C, -10°C, 0°C, 10°C, 25°C, 45°C]. It maintains a terminal voltage accuracy of ±80 mV at each temperature point. Next, the thermal model is parameterized and validated under non-isothermal conditions over a broad range of temperatures [-25°C to 45°C]. It predicts the core temperature with an accuracy of ±2°C. Finally, the combined ECHTM is validated under non-isothermal operating conditions, at different current rates, and temperature ranges.

The proposed combined ECHTM structure shows accurate terminal voltage and core temperature prediction at various operating conditions while maintaining a simple mathematical structure, making it ideal for real-time BMS applications.

Finally, a study that quantitatively reviewed three of the most common models used in Li-ion electric storage systems is presented. A model from each modeling category (Equivalent circuit models, Behavioral models, and electrochemical models) is considered. The three models are parameterized and validated under isothermal conditions. The accuracy of the models is validated through comparison with experimental data under the real-time driving profiles FTP-72 and WLTP case-3. The merits of the models are discussed with respect to their terminal voltage prediction accuracy in terms on RMSE and MAE, parameterization efforts, and computational complexity. The results showed that the second order equivalent circuit model (2RC) is the ideal model for real-time implementation in battery management systems. This is due to its high accuracy and low computational complexity.

Four model-based nonlinear state of charge estimation strategies were used to estimate the state of charge of the battery using the second order equivalent circuit model (2RC). The EKF, SVSF, VBL-SVSF; and UKF are compared with respect to their rate of convergence, robustness to modeling and measurement uncertainties, computational complexity, tuning complexity in terms of the number of tuning parameters, and SOC estimation accuracy using the RMSE and the MAE measures. The results indicate that the UKF and the VBL-SVSF outperform the SVSF and the EKF in the rate of convergence rate, robustness to uncertainties, and normal operation performance tests. In general, the UKF and the VBL-SVSF have comparable results in the aforementioned tests, though UKF slightly outperforms the VBL-SVSF. The UKF design, in comparison to the EKF design, is more tolerant to nonlinearities and can handle uncertainties of that sort. Also, the VBL-SVSF and the SVSF algorithms benefit from an inherently stable design that provides them with robustness against uncertainties. The main drawback of the UKF is in the computational and tuning complexity tests that limits its applicability, particularly in electric vehicle applications. In contrast, the SVSF has the least computational burden among the four estimators under study.

In general, the research has concluded that the models have shown higher accuracy at lower C-rates compared to higher C-rates. Also, driving patterns have show to affect the longevity of the battery.

In conclusion, the Continuous, Piecewise-Linear, Electrode-Average Model (CPWL-EAM) is developed. The CPWL-EAM is a new formulation for the reduced-order, electrode-average model (EAM). The CPWL-EAM formulation reduces the CPU runtime compared with the reduced-order, electrode-average model (EAM) while maintaining accuracy. The electrochemical model is then augmented with thermal model and heat generation model in order to be capable of predicting the cell's terminal voltage and core temperature over a broad range of temperatures and state of charges.

Finally, different model-based nonlinear state of charge estimation strategies were used to estimate the state of charge of the battery.

Bibliography

[1] Mohammed Farag, Matthias Fleckenstein, and Saeid Habibi. Continuous piecewise-linear, reduced-order electrochemical model for lithium-ion batteries in real-time applications. *Journal of Power Sources*, 342:351–362, feb 2017.

[2] The United States Environmental Protection Agency (EPA). Sources of greenhouse gas emissions, 2014. URL https://www.epa.gov/ghgemissions/sources-greenhouse-gas-emissions.

[3] The National Highway Traffic Safety Administration (NHTSA). Nhtsa and epa establish new national program to improve fuel economy and reduce greenhouse gas emissions for passenger cars and light trucks, 05 2010. URL https://www.nhtsa.gov/staticfiles/rulemaking/pdf/cafe/CAFE-GHG_Fact_Sheet.pdf.

[4] The U.S. Advanced Battery Consortium (USABC) LLC. Energy storage system goals. USABC. URL http://www.uscar.org/guest/article_view.php?articles_id=85.

[5] ISO/TC 22/SC 21. Electrically propelled road vehicles — test specification for

lithium-ion traction battery packs and systems — part 1: High-power applications. Standard, International Organization for Standardization - ISO/TC 22/SC 21, 2011.

[6] Languang Lu, Xuebing Han, Jianqiu Li, Jianfeng Hua, and Minggao Ouyang. A review on the key issues for lithium-ion battery management in electric vehicles. *Journal of power sources*, 226:272–288, 2013.

[7] Gregory L Plett. Extended kalman filtering for battery management systems of lipb-based hev battery packs: Part 1. background. *Journal of Power sources*, 134(2):252–261, 2004.

[8] Gregory L Plett. Extended kalman filtering for battery management systems of lipb-based hev battery packs: Part 2. modeling and identification. *Journal of power sources*, 134(2):262–276, 2004.

[9] Gregory L Plett. Extended kalman filtering for battery management systems of lipb-based hev battery packs: Part 3. state and parameter estimation. *Journal of power sources*, 134(2):277–292, 2004.

[10] Mohammed Farag, SA Gadsden, SR Habibi, and J Tjong. A comparative study of li-ion battery models and nonlinear dual estimation strategies. In *2012 IEEE Transportation electrification conference and expo (ITEC)*, pages 1–8. IEEE, 2012.

[11] Bernhard Schweighofer, Klaus M Raab, and Georg Brasseur. Modeling of high power automotive batteries by the use of an automated test system. *Instrumentation and Measurement, IEEE Transactions on*, 52(4):1087–1091, 2003.

[12] Min Chen, Gabriel Rincón-Mora, et al. Accurate electrical battery model capable of predicting runtime and iv performance. *Energy conversion, ieee transactions on*, 21(2):504–511, 2006.

[13] Mark W Verbrugge and Robert S Conell. Electrochemical and thermal characterization of battery modules commensurate with electric vehicle integration. *Journal of the Electrochemical Society*, 149(1):A45–A53, 2002.

[14] Mohammed Farag, Matthias Fleckenstein, and Saeid R Habibi. Li-ion battery SOC estimation using non-linear estimation strategies based on equivalent circuit models. In *SAE Technical Paper Series*. SAE International, apr 2014.

[15] CY Wang, WB Gu, and BY Liaw. Micro-macroscopic coupled modeling of batteries and fuel cells i. model development. *Journal of the Electrochemical Society*, 145(10):3407–3417, 1998.

[16] Domenico Di Domenico, Giovanni Fiengo, and Anna Stefanopoulou. Lithium-ion battery state of charge estimation with a kalman filter based on a electrochemical model. In *Control Applications, 2008. CCA 2008. IEEE International Conference on*, pages 702–707. Ieee, 2008.

[17] W Peukert. Über die abhängigkeit der kapazität von der entladestromstärke bei bleiakkumulatoren. *Elektrotechnische Zeitschrift*, 20:20–21, 1897.

[18] Dennis Doerffel and Suleiman Abu Sharkh. A critical review of using the peukert equation for determining the remaining capacity of lead-acid and lithium-ion batteries. *Journal of Power Sources*, 155(2):395–400, 2006.

[19] Clarence M Shepherd. Design of primary and secondary cells ii. an equation describing battery discharge. *Journal of the Electrochemical Society*, 112(7): 657–664, 1965.

[20] Stephan Buller. *Impedance-Based Simulation Models for Energy Storage Devices in Advanced Automotive Power Systems.* Shaker Verlag, 2002. ISBN 3832212256.

[21] Richard Lee Hartmann et al. *An aging model for lithium-ion cells.* PhD thesis, University of Akron, 2008.

[22] Alvin J Salkind, Craig Fennie, Pritpal Singh, Terrill Atwater, and David E Reisner. Determination of state-of-charge and state-of-health of batteries by fuzzy logic methodology. *Journal of Power Sources*, 80(1):293–300, 1999.

[23] V Pop, HJ Bergveld, JHG Op het Veld, PPL Regtien, D Danilov, and PHL Notten. Modeling battery behavior for accurate state-of-charge indication. *Journal of The Electrochemical Society*, 153(11):A2013–A2022, 2006.

[24] Hector E Perez, Jason B Siegel, Xinfan Lin, Anna G Stefanopoulou, Yi Ding, and Matthew P Castanier. Parameterization and validation of an integrated electro-thermal cylindrical lfp battery model. In *ASME 2012 5th Annual Dynamic Systems and Control Conference joint with the JSME 2012 11th Motion and Vibration Conference*, pages 41–50. American Society of Mechanical Engineers, 2012.

[25] Domenico Di Domenico, Anna Stefanopoulou, and Giovanni Fiengo. Lithium-ion battery state of charge and critical surface charge estimation using an electrochemical model-based extended kalman filter. *Journal of dynamic systems, measurement, and control*, 132(6):061302, 2010.

[26] Marc Doyle, Thomas F Fuller, and John Newman. Modeling of galvanostatic charge and discharge of the lithium/polymer/insertion cell. *Journal of the Electrochemical Society*, 140(6):1526–1533, 1993.

[27] Thomas F Fuller, Marc Doyle, and John Newman. Simulation and optimization of the dual lithium ion insertion cell. *Journal of the Electrochemical Society*, 141(1):1–10, 1994.

[28] Venkat R Subramanian, Vinten D Diwakar, and Deepak Tapriyal. Efficient macro-micro scale coupled modeling of batteries. *Journal of The Electrochemical Society*, 152(10):A2002–A2008, 2005.

[29] Venkat R Subramanian, Vijayasekaran Boovaragavan, and Vinten D Diwakar. Toward real-time simulation of physics based lithium-ion battery models. *Electrochemical and Solid-State Letters*, 10(11):A255–A260, 2007.

[30] Venkat R Subramanian, Vijayasekaran Boovaragavan, Venkatasailanathan Ramadesigan, and Mounika Arabandi. Mathematical model reformulation for lithium-ion battery simulations: Galvanostatic boundary conditions. *Journal of The Electrochemical Society*, 156(4):A260–A271, 2009.

[31] Long Cai and Ralph E White. Reduction of model order based on proper

orthogonal decomposition for lithium-ion battery simulations. *Journal of The Electrochemical Society*, 156(3):A154–A161, 2009.

[32] Joel C Forman, Saeid Bashash, Jeffrey L Stein, and Hosam K Fathy. Reduction of an electrochemistry-based li-ion battery model via quasi-linearization and padé approximation. *Journal of the Electrochemical Society*, 158(2):A93–A101, 2011.

[33] Kandler A Smith, Christopher D Rahn, and Chao-Yang Wang. Model order reduction of 1d diffusion systems via residue grouping. *Journal of Dynamic Systems, Measurement, and Control*, 130(1):011012, 2008.

[34] Kandler Smith, Christopher D Rahn, Chao-Yang Wang, et al. Model-based electrochemical estimation and constraint management for pulse operation of lithium ion batteries. *Control Systems Technology, IEEE Transactions on*, 18 (3):654–663, 2010.

[35] Bharath Bhikkaji and Torsten Söderström. Reduced order models for diffusion systems using singular perturbations. *Energy and buildings*, 33(8):769–781, 2001.

[36] Martin Golubitsky, Ian Stewart, et al. *Singularities and groups in bifurcation theory*, volume 2. Springer Science & Business Media, 2012.

[37] Bala S Haran, Branko N Popov, and Ralph E White. Determination of the hydrogen diffusion coefficient in metal hydrides by impedance spectroscopy. *Journal of Power Sources*, 75(1):56–63, 1998.

[38] Shriram Santhanagopalan, Qingzhi Guo, Premanand Ramadass, and Ralph E White. Review of models for predicting the cycling performance of lithium ion batteries. *Journal of Power Sources*, 156(2):620–628, 2006.

[39] Saeed Khaleghi Rahimian, Sean Rayman, and Ralph E White. Extension of physics-based single particle model for higher charge–discharge rates. *Journal of Power Sources*, 224:180–194, 2013.

[40] Yo Kobayashi, Nobuo Kihira, Katsuhito Takei, Hajime Miyashiro, Kazuma Kumai, Nobuyuki Terada, and Rikio Ishikawa. Electrochemical and calorimetric approach to spinel lithium manganese oxide. *Journal of Power Sources*, 81-82: 463–466, sep 1999.

[41] S Al Hallaj, J Prakash, and J.R Selman. Characterization of commercial li-ion batteries using electrochemical–calorimetric measurements. *Journal of Power Sources*, 87(1-2):186–194, apr 2000.

[42] Carolyn R. Pals. Thermal modeling of the lithium/polymer battery. *Journal of The Electrochemical Society*, 142(10):3282, 1995.

[43] D. Bernardi. A general energy balance for battery systems. *Journal of The Electrochemical Society*, 132(1):5, 1985. ISSN 00134651.

[44] S. J. Bazinski and X. Wang. The influence of cell temperature on the entropic coefficient of a lithium iron phosphate (lfp) pouch cell. *Journal of the Electrochemical Society*, 161(1):A168–A175, 2013. ISSN 0013-4651.

[45] Jan Philipp Schmidt, André Weber, and Ellen Ivers-Tiffée. A novel and precise

measuring method for the entropy of lithium-ion cells. *Electrochimica Acta*, 137:311–319, 2014. ISSN 00134686.

[46] K. Jalkanen, T. Aho, and K. Vuorilehto. Entropy change effects on the thermal behavior of a lifepo4/graphite lithium-ion cell at different states of charge. *Journal of Power Sources*, 243:354–360, 2013. ISSN 03787753.

[47] Songrui Wang. Entropy and heat generation of lithium cells/batteries. *Chinese Physics B*, 25(1):010509, 2016. ISSN 1674-1056.

[48] Karen E. Thomas and John Newman. Thermal modeling of porous insertion electrodes. *Journal of The Electrochemical Society*, 150(2):A176, 2003. ISSN 00134651.

[49] Nicolas Damay, Christophe Forgez, Marie-Pierre Bichat, and Guy Friedrich. Thermal modeling of large prismatic lifepo 4/graphite battery. coupled thermal and heat generation models for characterization and simulation. *Journal of Power Sources*, 283:37–45, 2015.

[50] Christophe Forgez, Dinh Vinh Do, Guy Friedrich, Mathieu Morcrette, and Charles Delacourt. Thermal modeling of a cylindrical lifepo 4/graphite lithium-ion battery. *Journal of Power Sources*, 195(9):2961–2968, 2010.

[51] Andrey Smyshlyaev, Miroslav Krstic, Nalin Chaturvedi, Jasim Ahmed, and Aleksandar Kojic. Pde model for thermal dynamics of a large li-ion battery pack. In *Proceedings of the 2011 American Control Conference*, pages 959–964. IEEE, 2011.

[52] Xiao Hu, Saeed Asgari, Shaohua Lin, Scott Stanton, and Wenyu Lian. A linear parameter-varying model for hev/ev battery thermal modeling. In *2012 IEEE Energy Conversion Congress and Exposition (ECCE)*, pages 1643–1649. IEEE, 2012.

[53] Guifang Guo, Bo Long, Bo Cheng, Shiqiong Zhou, Peng Xu, and Binggang Cao. Three-dimensional thermal finite element modeling of lithium-ion battery in thermal abuse application. *Journal of Power Sources*, 195(8):2393–2398, 2010.

[54] Naoki Baba, Hiroaki Yoshida, Makoto Nagaoka, Chikaaki Okuda, and Shigehiro Kawauchi. Numerical simulation of thermal behavior of lithium-ion secondary batteries using the enhanced single particle model. *Journal of Power Sources*, 252:214–228, 2014.

[55] Cheng Lin, Ke Chen, Fengchun Sun, Peng Tang, and Hongwei Zhao. Research on thermo-physical properties identification and thermal analysis of ev li-ion battery. In *2009 IEEE Vehicle Power and Propulsion Conference*, pages 1643–1648. IEEE, 2009.

[56] Xinfan Lin, Hector E Perez, Jason B Siegel, Anna G Stefanopoulou, Yonghua Li, R Dyche Anderson, Yi Ding, and Matthew P Castanier. Online parameterization of lumped thermal dynamics in cylindrical lithium ion batteries for core temperature estimation and health monitoring. *IEEE Transactions on Control Systems Technology*, 21(5):1745–1755, 2013.

[57] Sudipta Chakraborty, Marcelo G. Simoes, and William E. Kramer. *Power*

Electronics for Renewable and Distributed Energy Systems. Springer London, 2013.

[58] Suleiman Abu-Sharkh and Dennis Doerffel. Rapid test and non-linear model characterisation of solid-state lithium-ion batteries. *Journal of Power Sources*, 130(1-2):266–274, may 2004.

[59] Shalini Rodrigues, N. Munichandraiah, and A.K. Shukla. A review of state-of-charge indication of batteries by means of a.c. impedance measurements. *Journal of Power Sources*, 87(1-2):12–20, apr 2000.

[60] Evgenij Barsoukov, Jong Hyun Kim, Chul Oh Yoon, and Hosull Lee. Universal battery parameterization to yield a non-linear equivalent circuit valid for battery simulation at arbitrary load. *Journal of Power Sources*, 83(1-2):61–70, oct 1999.

[61] Sabine Piller, Marion Perrin, and Andreas Jossen. Methods for state-of-charge determination and their applications. *Journal of Power Sources*, 96(1):113–120, jun 2001.

[62] Jean Alzieu, Hassan Smimite, and Christian Glaize. Improvement of intelligent battery controller: state-of-charge indicator and associated functions. *Journal of Power Sources*, 67(1-2):157–161, jul 1997.

[63] T. Weigert, Q. Tian, and K. Lian. State-of-charge prediction of batteries and battery–supercapacitor hybrids using artificial neural networks. *Journal of Power Sources*, 196(8):4061–4066, apr 2011.

[64] N. Abolhassani Monfared, N. Gharib, H. Moqtaderi, M. Hejabi, M. Amiri, F. Torabi, and A. Mosahebi. Prediction of state-of-charge effects on lead-acid

battery characteristics using neural network parameter modifier. *Journal of Power Sources*, 158(2):932–935, aug 2006.

[65] S. Grewal. A novel technique for modelling the state of charge of lithium ion batteries using artificial neural networks. In *Twenty-Third International Telecommunications Energy Conference. INTELEC 2001*. Institution of Engineering and Technology (IET), 2001.

[66] K. Amine, C.H. Chen, J. Liu, M. Hammond, A. Jansen, D. Dees, I. Bloom, D. Vissers, and G. Henriksen. Factors responsible for impedance rise in high power lithium ion batteries. *Journal of Power Sources*, 97-98:684–687, jul 2001.

[67] I Bloom, B.W Cole, J.J Sohn, S.A Jones, E.G Polzin, V.S Battaglia, G.L Henriksen, C Motloch, R Richardson, T Unkelhaeuser, D Ingersoll, and H.L Case. An accelerated calendar and cycle life study of li-ion cells. *Journal of Power Sources*, 101(2):238–247, oct 2001.

[68] R. Spotnitz. Simulation of capacity fade in lithium-ion batteries. *Journal of Power Sources*, 113(1):72–80, jan 2003.

[69] Andrea Cordoba-Arenas, Simona Onori, Yann Guezennec, and Giorgio Rizzoni. Capacity and power fade cycle-life model for plug-in hybrid electric vehicle lithium-ion battery cells containing blended spinel and layered-oxide positive electrodes. *Journal of Power Sources*, 278:473–483, mar 2015.

[70] Anthony Barré, Benjamin Deguilhem, Sébastien Grolleau, Mathias Gérard, Frédéric Suard, and Delphine Riu. A review on lithium-ion battery ageing

mechanisms and estimations for automotive applications. *Journal of Power Sources*, 241:680–689, nov 2013. doi: 10.1016/j.jpowsour.2013.05.040.

[71] J Li, E Murphy, J Winnick, and P.A Kohl. Studies on the cycle life of commercial lithium ion batteries during rapid charge–discharge cycling. *Journal of Power Sources*, 102(1-2):294–301, dec 2001.

[72] Jens Groot. *State-of-health estimation of li-ion batteries: Cycle life test methods.* PhD thesis, Chalmers University of Technology, 2014.

[73] Marc Doyle. Modeling of galvanostatic charge and discharge of the lithium/polymer/insertion cell. *Journal of The Electrochemical Society*, 140 (6):1526, 1993. doi: 10.1149/1.2221597.

[74] Dai Haifeng, Wei Xuezhe, and Sun Zechang. A new SOH prediction concept for the power lithium-ion battery used on HEVs. In *2009 IEEE Vehicle Power and Propulsion Conference*. Institute of Electrical and Electronics Engineers (IEEE), sep 2009. doi: 10.1109/vppc.2009.5289654.

[75] Madeleine Ecker, Jochen B. Gerschler, Jan Vogel, Stefan Käbitz, Friedrich Hust, Philipp Dechent, and Dirk Uwe Sauer. Development of a lifetime prediction model for lithium-ion batteries based on extended accelerated aging test data. *Journal of Power Sources*, 215:248–257, oct 2012. doi: 10.1016/j.jpowsour.2012.05.012.

[76] Chaochao Chen and Michael Pecht. Prognostics of lithium-ion batteries using model-based and data-driven methods. In *Proceedings of the IEEE 2012 Prognostics and System Health Management Conference (PHM-2012 Beijing).*

Institute of Electrical and Electronics Engineers (IEEE), may 2012. doi: 10.1109/phm.2012.6228850.

[77] J.D. Kozlowski. Electrochemical cell prognostics using online impedance measurements and model-based data fusion techniques. In *IEEE Aerospace Conference Proceedings (Cat. No.03TH8652)*. Institute of Electrical and Electronics Engineers (IEEE), 2003. doi: 10.1109/aero.2003.1234169.

[78] Githin K Prasad and Christopher D Rahn. Model based identification of aging parameters in lithium ion batteries. *Journal of power sources*, 232:79–85, 2013.

[79] Qingzhi Guo and Ralph E White. Cubic spline regression for the open-circuit potential curves of a lithium-ion battery. *Journal of The Electrochemical Society*, 152(2):A343–A350, 2005.

[80] Jennifer Pittman. Adaptive splines and genetic algorithms. *Journal of Computational and Graphical Statistics*, 11(3):615–638, 2002.

[81] Caihao Weng, Jing Sun, and Huei Peng. An open-circuit-voltage model of lithium-ion batteries for effective incremental capacity analysis. In *ASME 2013 Dynamic Systems and Control Conference*, pages V001T05A002–V001T05A002. American Society of Mechanical Engineers, 2013.

[82] Yiran Hu, S Yurkovich, Y Guezennec, and BJ Yurkovich. Electro-thermal battery model identification for automotive applications. *Journal of Power Sources*, 196(1):449–457, 2011.

[83] DE Neumann, S Lichte, and A Multi-Dimensional Battery Discharge Model. with thermal feedback applied to a lithium-ion battery pack. In *NDIA Ground*

Vehicle Systems Engineering and Technology Symposium-Modeling & Simulation, Testing and Validation (MSTV) Mini-Symposium, 2011.

[84] Antoni Szumanowski and Yuhua Chang. Battery management system based on battery nonlinear dynamics modeling. *IEEE transactions on vehicular technology*, 57(3):1425–1432, 2008.

[85] Wei Shyy, Young-Chang Cho, Wenbo Du, Amit Gupta, Chien-Chou Tseng, and Ann Marie Sastry. Surrogate-based modeling and dimension reduction techniques for multi-scale mechanics problems. *Acta Mechanica Sinica*, 27(6): 845–865, nov 2011. doi: 10.1007/s10409-011-0522-0.

[86] Y-B Yi and AM Sastry. Analytical approximation of the percolation threshold for overlapping ellipsoids of revolution. In *Proceedings of the Royal Society of London A: Mathematical, Physical and Engineering Sciences*, volume 460, pages 2353–2380. The Royal Society, 2004.

[87] Y.-B. Yi, C.-W. Wang, and A. M. Sastry. Two-dimensional vs. three-dimensional clustering and percolation in fields of overlapping ellipsoids. *Journal of The Electrochemical Society*, 151(8):A1292, 2004. doi: 10.1149/1.1769272.

[88] Matthieu Dubarry, Vojtech Svoboda, Ruey Hwu, and Bor Yann Liaw. Incremental capacity analysis and close-to-equilibrium ocv measurements to quantify capacity fade in commercial rechargeable lithium batteries. *Electrochemical and Solid-State Letters*, 9(10):A454, 2006. ISSN 10990062.

[89] Karthikeyan Kumaresan, Godfrey Sikha, and Ralph E. White. Thermal model for a li-ion cell. *Journal of The Electrochemical Society*, 155(2):A164, 2008.

[90] Karen E Thomas and John Newman. Heats of mixing and of entropy in porous insertion electrodes. *Journal of power sources*, 119:844–849, 2003.

[91] Zhe Li, Jianbo Zhang, Bin Wu, Jun Huang, Zhihua Nie, Ying Sun, Fuqiang An, and Ningning Wu. Examining temporal and spatial variations of internal temperature in large-format laminated battery with embedded thermocouples. *Journal of Power Sources*, 241:536–553, 2013.

[92] Kandler Smith and Chao-Yang Wang. Solid-state diffusion limitations on pulse operation of a lithium ion cell for hybrid electric vehicles. *Journal of Power Sources*, 161(1):628–639, 2006.

[93] Kong Soon Ng, Chin-Sien Moo, Yi-Ping Chen, and Yao-Ching Hsieh. Enhanced coulomb counting method for estimating state-of-charge and state-of-health of lithium-ion batteries. *Applied Energy*, 86(9):1506–1511, sep 2009. doi: 10.1016/j.apenergy.2008.11.021.

[94] Fangfang Yang, Yinjiao Xing, Dong Wang, and Kwok-Leung Tsui. A comparative study of three model-based algorithms for estimating state-of-charge of lithium-ion batteries under a new combined dynamic loading profile. *Applied Energy*, 164:387–399, feb 2016. doi: 10.1016/j.apenergy.2015.11.072.

[95] F. Huet. A review of impedance measurements for determination of the state-of-charge or state-of-health of secondary batteries. *Journal of Power Sources*, 70(1):59–69, jan 1998. doi: 10.1016/s0378-7753(97)02665-7.

[96] Fengchun Sun, Xiaosong Hu, Yuan Zou, and Siguang Li. Adaptive unscented

kalman filtering for state of charge estimation of a lithium-ion battery for electric vehicles. *Energy*, 36(5):3531–3540, may 2011. doi: 10.1016/j.energy.2011.03.059.

[97] Gregory L. Plett. Sigma-point kalman filtering for battery management systems of LiPB-based HEV battery packs. *Journal of Power Sources*, 161(2):1356–1368, oct 2006.

[98] Mingyu Gao, Yuanyuan Liu, and Zhiwei He. Battery state of charge online estimation based on particle filter. In *2011 4th International Congress on Image and Signal Processing*. Institute of Electrical and Electronics Engineers (IEEE), oct 2011. doi: 10.1109/cisp.2011.6100603.

[99] Mohinder S. Grewal and Angus P. Andrews. *Kalman Filtering: Theory and Practice with MATLAB*. JOHN WILEY & SONS INC, 2014. ISBN 1118851218. URL http://www.ebook.de/de/product/23151381/mohinder_s_grewal_angus_p_andrews_kalman_filtering_theory_and_practice_with_matlab.html.

[100] Greg Welch and Gary Bishop. *An introduction to the kalman filter. Department of Computer Science, University of North Carolina*. Chapel Hill, NC, unpublished manuscript, 2006.

[101] S. Julier, J. Uhlmann, and H. F. Durrant-Whyte. A new method for the non linear transformation of means and covariances in filters and estimations. *IEEE Transactions on automatic control*, 45(3):477–482, 2000.

[102] Simon J Julier and Jeffrey K Uhlmann. Unscented filtering and nonlinear estimation. *Proceedings of the IEEE*, 92(3):401–422, 2004.

[103] SR Habibi and R Burton. The variable structure filter. In *ASME 2002 International Mechanical Engineering Congress and Exposition*, pages 157–165. American Society of Mechanical Engineers, 2002.

[104] Saeid Habibi. The smooth variable structure filter. *Proceedings of the IEEE*, 95(5):1026–1059, may 2007.

[105] S. A. Gadsden and S. R. Habibi. A new robust filtering strategy for linear systems. *J. Dyn. Sys., Meas., Control*, 135(1):014503, oct 2012.

[106] B.S. Bhangu, P. Bentley, D.A. Stone, and C.M. Bingham. Nonlinear observers for predicting state-of-charge and state-of-health of lead-acid batteries for hybrid-electric vehicles. *IEEE Trans. Veh. Technol.*, 54(3):783–794, may 2005.

[107] A. Vasebi, S.M.T. Bathaee, and M. Partovibakhsh. Predicting state of charge of lead-acid batteries for hybrid electric vehicles by extended kalman filter. *Energy Conversion and Management*, 49(1):75–82, jan 2008.

[108] Tetsuro Okoshi, Keizo Yamada, Tokiyoshi Hirasawa, and Akihiko Emori. Battery condition monitoring (BCM) technologies about lead–acid batteries. *Journal of Power Sources*, 158(2):874–878, aug 2006.

[109] Xiaosong Hu, Shengbo Li, and Huei Peng. A comparative study of equivalent circuit models for li-ion batteries. *Journal of Power Sources*, 198:359–367, 2012.

[110] Jonghoon Kim, Seongjun Lee, and B. H. Cho. Complementary cooperation algorithm based on DEKF combined with pattern recognition for SOC/capacity

estimation and SOH prediction. *IEEE Transactions on Power Electronics*, 27 (1):436–451, jan 2012.

[111] Brian D. O. Anderson, John B. Moore, and Mansour Eslami. Optimal filtering. *IEEE Transactions on Systems, Man, and Cybernetics*, 12(2):235–236, 1982.

[112] William L. Brogan. Applied optimal estimation (arthur gels, ed.). *SIAM Rev.*, 19(1):172–175, jan 1977.

[113] Mohammad A. Al-Shabi, S. Andrew Gadsden, and Saeid R. Habibi. The toeplitz-observability smooth variable structure filter. In *2013 IEEE Jordan Conference on Applied Electrical Engineering and Computing Technologies (AEECT)*. Institute of Electrical & Electronics Engineers (IEEE), dec 2013.